



THE HONG KONG  
POLYTECHNIC UNIVERSITY

香港理工大學

Pao Yue-kong Library

包玉剛圖書館

---

## Copyright Undertaking

This thesis is protected by copyright, with all rights reserved.

**By reading and using the thesis, the reader understands and agrees to the following terms:**

1. The reader will abide by the rules and legal ordinances governing copyright regarding the use of the thesis.
2. The reader will use the thesis for the purpose of research or private study only and not for distribution or further reproduction or any other purpose.
3. The reader agrees to indemnify and hold the University harmless from and against any loss, damage, cost, liability or expenses arising from copyright infringement or unauthorized usage.

### IMPORTANT

If you have reasons to believe that any materials in this thesis are deemed not suitable to be distributed in this form, or a copyright owner having difficulty with the material being included in our database, please contact [lbsys@polyu.edu.hk](mailto:lbsys@polyu.edu.hk) providing details. The Library will look into your claim and consider taking remedial action upon receipt of the written requests.

**MINIATURE FIBER-TIP FABRY-PEROT  
INTERFEROMETRIC SENSORS FOR PRESSURE  
AND ACOUSTIC DETECTION**

MA JUN

Ph.D

The Hong Kong Polytechnic University

2014

The Hong Kong Polytechnic University

Department of Electrical Engineering

# **Miniature Fiber-tip Fabry-Perot Interferometric Sensors for Pressure and Acoustic Detection**

MA JUN

A thesis submitted in partial fulfillment of the requirements for the degree of Doctor  
of Philosophy

September 2013

## **CERTIFICATE OF ORIGINALITY**

I hereby declare that this thesis is my own work and that, to the best of my knowledge and belief, it reproduces no material previously published or written, nor material that has been accepted for the award of any other degree or diploma, except where due acknowledgement has been made in the text.

---

MA Jun

## **Abstract**

Pressure/acoustic detection has widespread applications in automobile, bio-medical, and oil/gas industries. Compared with their electro-mechanical counterparts, optical fiber pressure sensors (OFPSs) offer a number of advantages such as remote detection capability, light weight, electromagnetic immunity and corrosion resistance. Fabry-Perot interferometers (FPIs) with a deflectable diaphragm attached to a hollow-cavity at the end of a single mode fiber (SMF) represent an important class of OFPSs. These OFPSs are expected to have superior performance in terms of size and weight, detection sensitivity and bandwidth, and immunity to polarization fading. The objective of this dissertation is to improve the performance of the diaphragm-based OFPSs.

Various types of OFPSs are reviewed and the emphasis is placed on the diaphragm based FPI sensors. Basic theories of FPIs, as well as the mechanical response of the diaphragm subjected to static and dynamic pressures, are outlined. These theories form the foundation of the diaphragm-based FPIs for pressure measurement and provide the guideline for evaluating the sensor performance in terms of pressure sensitivity, frequency response, and noise equivalent pressure level.

A simple and low-cost technique for fabricating all-silica micro-cavities at the fiber end is developed. The technique involves splicing a hollow silica capillary to one end of a SMF and then melting the capillary to form a micro-cavity at the fiber end by using a fusion splicer. Experimental tests show that the micro-cavity has good mechanical strength and can sustain high temperature up to 1000 °C. With a pressure-assisted tapering process, the silica wall-thickness of the micro-cavity can be controlled and micro-cavities with the wall thickness from tens of

micrometers to 2.2  $\mu\text{m}$  have been practically made. The micro-cavity with the wall-thickness of 2.2  $\mu\text{m}$  demonstrates a pressure sensitivity of  $\sim 315$  pm/MPa, a low temperature sensitivity of 1.55 pm/ $^{\circ}\text{C}$ , and a maximum working pressure up to 40 MPa.

Ultra-sensitive fibre-optic FPI-based pressure/acoustic sensors with graphene diaphragms are developed. Graphene is the thinnest and strongest material known to us and it would represent the ultimate limit for two-dimensional diaphragm-based pressure sensors. A technique for transferring such thin graphene films is developed and used to build FPI sensors at the end of SMFs. With  $\sim 1$  nm-thick and  $\sim 25$   $\mu\text{m}$ -diameter graphene as the diaphragm, a sensor demonstrates a pressure sensitivity of  $\sim 40$  nm/kPa. This is a highly sensitive device considering the small size of the diaphragm, and the sensitivity is actually limited by the pre-stress in the diaphragm rather than the diaphragm thickness. With a larger ( $\sim 125$   $\mu\text{m}$  in diameter) multiple-layer graphene film ( $\sim 100$  nm in thickness), the sensor demonstrates a pressure (acoustic) sensitivity up to 1100 nm/kPa, and this, to my knowledge, is the highest value reported to date for the same type of sensors with similar diaphragm sizes. The sensor exhibits a flat frequency response from 0.2 to 22 kHz and a noise equivalent acoustic pressure level of  $\sim 60$   $\mu\text{Pa}/\text{Hz}^{1/2}$  at the frequency of 10 kHz.

A fiber-tip pressure sensor based on the mechanical resonance of the graphene diaphragm is demonstrated for the first time to my knowledge. A poly(methyl methacrylate)-assisted graphene transferring technique is developed and the technique might be also useful for building other graphene based optical fiber devices. The resonator is excited and interrogated optically by using an all-fiber system and this type of sensors would have potential applications in mass, pressure and force detection. For pressure detection, a miniature micro-resonator with a beam-shape diaphragm demonstrates a pressure sensitivity of over an order

of magnitude higher than that of a silicon cantilever. An additional advantage of the resonance detection scheme is that it needs no sealed cavity, making this type of pressure sensors inherently more immune to possible diaphragm fatigue.

## List of Publications

### *Journal papers*

1. **J. Ma**, J. Ju, L. Jin, W. Jin, and D. N. Wang, "Fiber-tip micro-cavity for temperature and transverse load sensing," *Optics Express*. **19** (13), 12418-12426, (2011).
2. **J. Ma**, J. Ju, L. Jin, and W. Jin, "A Compact Fiber-tip Micro-cavity Sensor for High Pressure Measurement," *IEEE Photon. Technol. Lett.* **23** (21), 1561-1563 (2011).
3. **J. Ma**, W. Jin, H. L. Ho, and J. Y. Dai, "High-sensitivity fiber-tip pressure sensor with graphene diaphragm," *Opt. Lett.* **37**, 2493-2495 (2012).
4. **J. Ma**, H. Xuan, H. L. Ho, W. Jin, Y. Yang, and S. Fan, "Fiber-Optic Fabry–Pérot Acoustic Sensor With Multilayer Graphene Diaphragm," *IEEE Photon. Technol. Lett.* **25** (10), 932-935 (2013).
5. Y. Cao, W. Jin, H. L. Ho, and **J. Ma**, "Miniature fiber-tip photoacoustic spectrometer for trace gas detection," *Opt. Lett.* **38**, 434-436 (2013).
6. C. Wang, W. Jin, **J. Ma**, Y. Wang, H. L. Ho, and X. Shi, "Suspended core photonic microcells for sensing and device applications," *Opt. Lett.* **38**, 1881-1883 (2013).

### *Conference papers*

1. **J. Ma**, W. Jin, and L. Jin, "A novel fiber-tip micro-cavity sensor for high temperature application," Proc. of 21st International Conference on Optical Fiber Sensors, Ottawa, 15-19 May 2011, Proc. of SPIE, paper No. 7753-385 (2011).
2. **J. Ma**, W. Jin, and L. Jin, "Temperature characteristics of microfiber long-period-gratings fabricated by a femtosecond infrared laser," Proc. of 21st International Conference on Optical Fiber Sensors, Ottawa, 15-19 May 2011,

- Proc. of SPIE, paper No. 7753-391 (2011).
3. **J. Ma** and W. Jin, “In-fiber microsphere air-cavity Fabry-Perot interferometer for strain/temperature measurement,” Proc. of the 22nd International Conference on Optical Fiber Sensors, Beijing, 15-19 October 2012, Proc. of the SPIE, paper No. 8421-321 (2012).
  4. **J. Ma**, W. Jin, and H. L. Ho, “A fiber-tip Fabry-Perot pressure sensor with graphene diaphragm,” Proc. of the 22nd International Conference on Optical Fiber Sensors, Beijing, 15-19 October 2012, Proc. of the SPIE, paper No. 8421-422 (2012). Best student paper award.

## **Acknowledgements**

I would like to express my deep gratitude to my supervisor, Prof. Wei Jin, for his invaluable encouragement, support and suggestion during the past four years. His conscientious research attitude and insightful view impress me and remain as precious asset to me. His patience and kindness to the student also set a good example for me. I am also very grateful to my co-supervisor, Dr. Jiyan Dai and Dr. Dongning Wang for their helpful discussions and advices.

Special thanks go to Dr. Jian Ju and Dr. Long Jin for their kind help and care especially when I just started my PhD study. It is my fortune to work with them and learn from them. I would also like to thank all my colleagues at Fiber Optics Lab for their help to my research.

Finally, I would give special gratitude to my beloved family, my parents, my sisters and my wife. Their continuous support and self-giving love keep encouraging me to move forward during my entire study period.

## Contents

<b>Abstract.....</b>	<b>I</b>
<b>List of Publications.....</b>	<b>IV</b>
<b>Acknowledgements.....</b>	<b>VI</b>
<b>Contents .....</b>	<b>VII</b>
<b>List of Figures.....</b>	<b>X</b>
<b>List of Tables.....</b>	<b>XIX</b>
<b>Chapter 1 Introduction.....</b>	<b>1</b>
1.1 Background review .....	1
1.1.1 Intensity modulation based FOPS.....	2
1.1.2 Spectrum modulation based FOPS .....	4
1.1.3 Polarization modulation based FOPS.....	6
1.1.4 Phase modulation based FOPS .....	7
1.2 Research motivation and significance .....	14
1.3 Thesis outline.....	16
<b>Chapter 2 Basic principle of FPIs.....</b>	<b>22</b>
2.1 Interference spectrum of FPIs.....	22
2.1.1 High-finesse and low-finesse Fabry-Perot cavities.....	22
2.1.2 Interference spectrum considering the diaphragm thickness .....	27
2.2 Signal demodulation for FPIs .....	30
2.2.1 Spectrum detection based demodulation.....	30
2.2.2 Linear demodulation .....	33
2.3 Noise analysis .....	37
2.3.1 Noise source.....	37
2.3.2 Noise equivalent pressure level.....	38

2.4	Summary.....	40
<b>Chapter 3</b>	<b>Silica and graphene diaphragms .....</b>	<b>42</b>
3.1	Diaphragm design.....	42
3.2	Mechanical properties of the silica diaphragm.....	45
3.2.1	Response to static pressure.....	45
3.2.2	Response to dynamic pressure .....	48
3.3	Mechanical and optical properties of the graphene diaphragm .....	51
3.3.1	Methods for the production of the graphene.....	51
3.3.2	Characterization of the graphene .....	54
3.3.3	Mechanical properties of the graphene diaphragm .....	56
3.3.4	Optical reflectivity of the graphene diaphragm .....	66
3.4	Summary.....	69
<b>Chapter 4</b>	<b>Miniature all-silica micro-cavity pressure sensors .....</b>	<b>72</b>
4.1	Introduction.....	72
4.2	Fabrication of the fiber-tip micro-cavities .....	73
4.3	Pressure sensitivity enhancement by the pressure-assisted tapering .....	77
4.3.1	Pressure-assisted tapering .....	77
4.3.2	Interrogation of the fiber-tip micro-cavity sensors .....	79
4.4	Pressure and temperature responses .....	81
4.5	Summary.....	87
<b>Chapter 5</b>	<b>Graphene diaphragm based FPI pressure and acoustic sensors..</b>	<b>89</b>
5.1	Introduction.....	89
5.2	Graphene diaphragm.....	90
5.2.1	Graphene preparation and transferring.....	90
5.2.2	Graphene characterization.....	91
5.3	Fiber-tip FPI with the few-layer graphene diaphragm.....	94
5.3.1	Fabrication and interrogation .....	95

5.3.2	Pressure response .....	100
5.3.3	Temperature response.....	106
5.4	Ferrule-top FPI with the multi-layer graphene diaphragm.....	107
5.4.1	Sensor fabrication and interrogation .....	108
5.4.2	Response to acoustic pressure.....	111
5.4.3	Noise analysis .....	117
5.5	Summary.....	119
<b>Chapter 6</b>	<b>Graphene diaphragm based micro-mechanical resonators .....</b>	<b>122</b>
6.1	Introduction.....	122
6.2	Theoretical basis for the graphene based micro-mechanical resonator .....	124
6.2.1	Damped oscillator with the harmonic excitation .....	124
6.2.2	Theoretical analysis of the damped resonant beam.....	127
6.3	Fabrication of the graphene diaphragm based micro-resonator.....	133
6.4	Optical excitation and interrogation of the micro-resonator.....	137
6.4.1	Optical excitation .....	137
6.4.2	Optical interrogation .....	138
6.4.3	Effects of air pressure.....	142
6.5	Post-processing of the graphene diaphragm by the femtosecond laser .....	144
6.6	Summary.....	148
<b>Chapter 7</b>	<b>Conclusion and future work .....</b>	<b>152</b>
7.1	Conclusion .....	152
7.2	Future work.....	154

## List of Figures

- Fig. 1.1 Schematic of (a) a I-FOPS based on pressure induced bending loss [7]; (b) an undisturbed optical fiber; (c) an optical fiber with micro-bending.  $\theta$  and  $\theta_c$  are the incident angle and the critical angle of light in the optical fiber, respectively.
- Fig. 1.2 Schematic of a FBG and its reflection spectrum (a) without and (b) with pressure;  $\lambda_0$ : the resonant wavelength,  $\Delta\lambda$ : the resonant wavelength change,  $n_{eff}$ : the effective refractive index,  $\Lambda$ : the grating period,  $\Delta\Lambda$ : change of the grating period,  $\Delta n_{eff}$ : change of the effective refractive index.
- Fig. 1.3 (a) Schematic of a Hi-Bi fiber based FOPS. Images of (b) a side-hole fiber [25]; (c) a polarization maintaining PCF [28]; (d) a Hi-Bi microstructure fiber [30].
- Fig. 1.4 Schematic of the configurations of (a) the Mach-Zehnder interferometer and (b) the Michelson interferometer; (c) the acoustically designed mandrel and coating for the pressure sensitivity enhancement [33].
- Fig. 1.5 (a) Schematic of a FPI with a section of capillary as the Fabry-Perot cavity; cross-section images of (b) a capillary; (c) a simplified HC-PBG; (d) a HC-PBG.
- Fig. 1.6 (a) a FPI pressure sensor with a polymer (SU-8) diaphragm; (b) a fiber-tip FPI pressure sensor with a silica diaphragm; (c) a FPI acoustic sensor with a silicon photonic crystal diaphragm; (d) a silver diaphragm; (e) a silver diaphragm; (f) a silicon photonic crystal diaphragm.
- Fig. 2.1 Schematic of (a) a Fabry-Perot cavity and (b) a typical reflection spectrum of the FPI.
- Fig. 2.2 Calculated reflection spectrums of the FPIs with different values of  $R_1$ ,  $R_2$ .

In the calculation, the cavity length  $L=200\ \mu\text{m}$ , the refractive index of the cavity  $n=1$ , and the transmission coefficient  $\eta=1$ .

- Fig. 2.3 Schematic of the FPI with the silica diaphragm.  $L$  is the air-cavity length of the FPI.
- Fig. 2.4 The transmission coefficient  $\eta$  as a function of the cavity length. The source coherence is not considered in the above calculation.
- Fig. 2.5 Schematic of the matrix method for calculating the transmission and reflection coefficients of a three-layer structure.
- Fig. 2.6 Relative intensity of the reflected light from the low-finesse FPI calculated by the  $2\times 2$  matrix method and the three-beam interference approximation described by Eq. (2.14), respectively. In the calculation, the cavity length  $L=20\ \mu\text{m}$ , the diaphragm thickness  $t=2\ \mu\text{m}$ , and the refractive index of the diaphragm and cavity are  $n_{diaphragm}=1.45$  and  $n_{cavity}=1$  (air), respectively.
- Fig. 2.7 Schematic of the spectrum detection based demodulation of the FPI.
- Fig. 2.8 Typical interference spectrum of the FPI.
- Fig. 2.9 Illustration of the linear demodulation at different operating wavelengths.
- Fig. 2.10 Interference spectrums of FPIs with different values of  $R_1$  and  $R_2$ . The circle symbols denote the Q points of the interference spectrum.
- Fig. 2.11 MDP as a function of the optical power incident on the detector  $I_{inc}$ .
- Fig. 3.1 Parameter space delineating regions of the plate behavior, linear membrane behavior, and nonlinear membrane behavior [1].
- Fig. 3.2 (a) Schematic of a diaphragm based FPI pressure sensor; (b) calculated deflection of a silica diaphragm with a radius of  $62.5\ \mu\text{m}$  and a thickness of  $2\ \mu\text{m}$  under a pressure of  $1\ \text{kPa}$ .
- Fig. 3.3 Pressure sensitivity as a function of the thickness for the silica diaphragm with different values of the radius.
- Fig. 3.4 Pressure sensitivity as a function of the thickness of the silica

semi-spherical shell with different values of the radius.

- Fig. 3.5 Frequency response of the diaphragm with the radius  $R= 62.5 \mu\text{m}$  and the thickness  $t= 2 \mu\text{m}$ .
- Fig. 3.6 Microscope image of the mechanical exfoliated graphene with different layers on the  $\text{SiO}_2/\text{Si}$  substrate [9].
- Fig. 3.7 Schematic diagram of a typical system for the graphene grown by the CVD method [11].
- Fig. 3.8 Schematic of (a) the membrane on a well and (b) the cross section of the membrane on the well under a pressure  $\Delta p$ .
- Fig. 3.9 Pressure induced deflections of the membranes with different values of radius. The thickness of the membrane in the calculation is 1 nm and the pre-stress is 1 GPa.
- Fig. 3.10 Pressure induced deflections of membranes with different values of thickness and pre-stress. The radius of the membrane in calculation is 10  $\mu\text{m}$ .
- Fig. 3.11 Sketch of the calculated vibration modes with different mode order  $(m, n)$  for a circular membrane.
- Fig. 3.12 Resonant frequency as functions of the pressure for membranes with different pre-stress  $\sigma_0$ .
- Fig. 3.13 Relative frequency shift as functions of the pressure for membranes with different values of thickness.
- Fig. 3.14 Reflectivity as functions of the graphene layer number for the graphene with refractive indices listed in Table 3.7.
- Fig. 3.15 Calculated transmission, reflection and absorption coefficient as functions of the layer number of the graphene film; inset: the reflectivity for the graphene film with the layer number from 1 to 15.
- Fig. 3.16 Calculated transmission, reflection and absorption coefficient as functions

of the thickness of the Au film. The refractive index of Au used is 0.55-11.5i [31].

- Fig. 4.1 Fabrication process for the fiber-tip micro-cavity. (a) Splicing the capillary with the SMF28; (b) melt the capillary at a distance of  $L$  from the spliced joint; (c) schematic image for the fiber-tip micro-cavity; Microscope images of (d) the cross-section of the capillary; (e) the micro-cavity.
- Fig. 4.2 Reflection spectrums of the micro-cavity FPI without (a) and with (b) the reduction of the light reflection from the surface 3 (as shown in Fig. 4.1(c)).
- Fig. 4.3 Dependence of the air cavity length  $d$  and the silica wall thickness  $t$  on the offset distance  $L$ .
- Fig. 4.4 Fiber-tip micro-cavities fabricated by the use of different offset distances  $L$ . (a) 300  $\mu\text{m}$ ; (b) 400  $\mu\text{m}$ ; (c) 700  $\mu\text{m}$ .
- Fig. 4.5 Relation between the wavelength spacing of the reflection spectrum and the cavity length of the micro-cavity.
- Fig. 4.6 Pressure-assisted fabrication process for the decrease of the wall thickness of the micro-cavity sensor: (a) tapering the capillary under the assistance of pressure; (b) melting the taper by applying an electric arc; (c) and (d) show the microscope images of the fabricated micro-cavities with the silica-wall thickness  $t$ , respectively  $\sim 6 \mu\text{m}$  and  $2.2 \mu\text{m}$ . Microscope image of the tapered capillary is shown in the inset in (b).
- Fig. 4.7 Measured reflection spectrums of the micro-cavity sensors with the air cavity length/silica wall thickness of (a) 134  $\mu\text{m}/6.2 \mu\text{m}$ ; (b) 120  $\mu\text{m}/2.2 \mu\text{m}$ , respectively.
- Fig. 4.8 Curve fitting of the measured spectrum as shown in Fig. 4.7(a).
- Fig. 4.9 Experimental setup for the pressure measurement.
- Fig. 4.10 (a) Pressure response of the micro-cavity sensor with  $t = 11.4 \mu\text{m}$  and  $d =$

123 $\mu\text{m}$ ; (b) wavelength shifts as functions of the applied pressure for three cavity sensors with different parameters. S1: ( $t = 4.3 \mu\text{m}$ ,  $d = 130 \mu\text{m}$ ), S2: ( $t = 5.5 \mu\text{m}$ ,  $d = 132 \mu\text{m}$ ), S3: ( $t = 11.4 \mu\text{m}$ ,  $d = 123 \mu\text{m}$ ).

Fig. 4.11 Pressure sensitivity of the micro-cavity sensor as a function of the silica wall thickness  $t$ . In the calculation, the value of  $d$ ,  $R$  and  $\lambda$  used are 130  $\mu\text{m}$ , 87  $\mu\text{m}$  and 1550 nm, respectively.

Fig. 4.12 (a) Deflection and (b) von Mises stress distribution in the micro-cavity under the pressure of 70 MPa.

Fig. 4.13 Temperature response of the micro-cavity sensor with  $t = 8\mu\text{m}$ .

Fig. 5.1 Schematic diaphragm of transferring the graphene from the CVD graphene samples to a  $\text{SiO}_2/\text{Si}$  substrate. (a) Graphene/metal foil on the  $\text{FeCl}_3$  solution; (b) graphene floated on the DI water; (c) scooping the graphene with a  $\text{SiO}_2/\text{Si}$  substrate; (d) graphene on the  $\text{SiO}_2/\text{Si}$  substrate.

Fig. 5.2 Microscope images of the SLG, FLG and MLG transferred onto the  $\text{SiO}_2/\text{Si}$  substrate.

Fig. 5.3 AFM images of (a) the single-layer, (b) the few-layer and (c) the multi-layer graphene transferred on the  $\text{SiO}_2/\text{Si}$  substrate.

Fig. 5.4 Raman spectrums of the single, few and multi-layer graphene.

Fig. 5.5 Schematic of (a) the graphene diaphragm based FPI pressure sensor; (b) an open air-cavity on the fiber end; (c) the cavity covered with the graphene diaphragm.

Fig. 5.6 Schematic of (a) a SMF spliced with a section of capillary and (b) the capillary cut by the cleaver at a distance of  $L$  from the splicing joint; (c) the microscope image of the process for cleaving the capillary.

Fig. 5.7 Microscope images of (a) the fiber/capillary tip; (b) the cross-section of the tip endface; inset: fiber-tip immersed in the oil with a refractive index of 1.4.

- Fig. 5.8 Fabrication process of the fiber-tip micro-cavity with a graphene diaphragm. (a) Etching off the Ni layer by immersing the sample to a  $\text{FeCl}_3$  solution; (b) transferring graphene film floating on the water surface to the surface of fiber-tip open-cavity; (c) schematic showing the graphene film covering a fiber-tip micro-cavity. Photographs of (d) a graphene/Ni/SiO<sub>2</sub>/Si sample floating on the  $\text{FeCl}_3$  solution; (e) graphene films floating on DI water; (d) the micro-cavity with the graphene covered.
- Fig. 5.9 (a) Measured and fitted reflection spectrums of the FPI; (b) calculated reflectivity as a function of the number of graphene layers at the wavelength of 1550 nm. The refractive index of the graphene used in the calculation is  $3.45 - 2.32i$  [15].
- Fig. 5.10 Reflectivities of the SMF endface with different tilted angles at the wavelength of 1550 nm.
- Fig. 5.11 Pressure response of the fiber-tip micro-cavity with the graphene film.
- Fig. 5.12 Cavity length change vs time for an initially applied pressure of  $\sim 13$  kPa.
- Fig. 5.13 Fitted pre-stress and thickness of the graphene film from the measured pressure response of several fiber-tip micro-cavity sensors.
- Fig. 5.14 The microscope images of the cross-section of the capillary before (a) and after (b) the smoothing treatment.
- Fig. 5.15 AFM images of the capillary end surface (a) before and (b) after smoothing treatment.  $R_a$  and  $R_q$  are the average roughness and the root mean square roughness, respectively.
- Fig. 5.16 (a) Reflection spectrums of the FPI at different pressures; (b) the cavity length change as a function of the applied pressure.
- Fig. 5.17 Cavity length change of the FPI during the pressure up and down cycle.
- Fig. 5.18 Temperature response of the FPI sensor. Green curve: the calculated cavity length change induced by the pressure change of the air in the cavity; blue

curve: the calculated cavity length change induced by the thermal expansion of the cavity; dots: the experimental results for the cavity length change in the temperature up and down cycle.

- Fig. 5.19 (a) Schematic of the FPI configuration: a 125  $\mu\text{m}$ -diameter zirconia ferrule with a SMF inserted into it and a graphene diaphragm covering its endface; (b) photograph of the fabricated FPI; microscope images of the ferrule endface (c) before and (d) after it is covered with the graphene diaphragm.
- Fig. 5.20 Interference spectrum of the multi-layer graphene diaphragm based FPI.
- Fig. 5.21 (a) Measured reflection spectrums of FPI with different cavity lengths; (b) calculated reflectivity of graphene diaphragm at 1550 nm as a function of its thickness. The complex refractive index of graphene is assumed to be  $3.45-2.32i$  [15].
- Fig. 5.22 (a) Schematic of the experimental setup for the acoustic pressure measurement; (b) photograph of the acoustic isolation box.
- Fig. 5.23 (a) Output voltage signal of the FPI for varying applied acoustic pressure levels at the frequency of 10 kHz; (b) frequency response of the FPI.
- Fig. 5.24 (a) Power spectrum of the FPI output under an acoustic pressure level of 400 mPa at 10 kHz; (b) output voltages of the FPI for acoustic pressures of 0 mPa, 2 mPa and 4 mPa at 10 kHz.
- Fig. 5.25 Normalized acoustic sensitivity of the FPI with different alignment angles at the acoustic frequency of 10 kHz. Inset: schematic showing the alignment angle between the sensor head and the speaker.
- Fig. 5.26 Noise spectrums of the FPI sensor when the laser is off, the laser power is -25 dBm and the laser power is -20 dBm.
- Fig. 5.27 Power spectrums of the FPI sensor in the Q-point demodulation system when the output power of the laser is -25 dBm, -10 dBm and 0 dBm.
- Fig. 6.1 Spring-mass-damper model for a forced resonator with viscous damping.

- Fig. 6.2 The amplitude and phase as functions of the frequency ratio ( $w/w_0$ ) for the harmonically excited oscillator with viscous damping.
- Fig. 6.3 Amplitude versus the frequency ratio for different values of  $\zeta$ .
- Fig. 6.4 Relative frequency changes for beam resonators with the thickness of 5, 10, 20 nm with/without considering the viscosity effect.
- Fig. 6.5 Schematic of the fabrication process for the MLG film.
- Fig. 6.6 Schematic of the process for transferring the MLG film to the ferrule top.
- Fig. 6.7 Microscope images of (a) the ferrule endface; (b) the ferrule endface with the PMMA/graphene film; (c) the ferrule endface with PMMA removed; (d) sample in (c) after being heated at 400 °C for 2 hours.
- Fig. 6.8 A typical reflection spectrum of the graphene diaphragm based resonator.
- Fig. 6.9 Schematic of an all-fiber system for measuring the resonant frequency of the graphene diaphragm based resonator.
- Fig. 6.10 Spectrums of the EDFA output with different injected currents.
- Fig. 6.11 Spectrums of the light intensity reflected by the graphene before and after the band-pass filter. The spectrums are offset vertically for the purpose of easy observation.
- Fig. 6.12 Amplitude versus frequency of the circular graphene diaphragm in the vacuum ( $2 \times 10^{-5}$  mBar); red dash line denotes the calculated frequencies of the high order resonant modes.
- Fig. 6.13 Q value of the fundamental mode as a function of the air pressure; Inset: the frequency responses of the resonator at the pressure of  $2 \times 10^{-5}$  and 100 mBar.
- Fig. 6.14 Resonant frequency of the fundamental resonant mode as a function of the air pressure.
- Fig. 6.15 Resonant frequencies of high-order resonant modes as functions of the air pressure.

- Fig. 6.16 Microscope images of (a) a circular graphene diaphragm with two scratch lines and (b) a beam-shape grapheme diaphragm manufactured by using the fs laser.
- Fig. 6.17 Amplitude versus frequency of the beam-shape graphene diaphragm in vacuum ( $1 \times 10^{-4}$  mBar). Inset: enlarged part of the frequency response near the frequency of 135 kHz.
- Fig. 6.18 Amplitude versus frequency of the beam-shape graphene diaphragm at the atmosphere (1000 mBar).
- Fig. 6.19 Resonant spectrums of the beam-shape graphene diaphragm at different air pressures. Inset: Q values of the fundamental resonant mode of the beam-shape graphene diaphragm as a function of the air pressure.
- Fig. 6.20 Resonant frequency of the fundamental resonant mode of the beam-shape graphene diaphragm as a function of the air pressure.

## List of Tables

- Table 1.1 Pressure sensitivities of FPIs with diaphragms of different materials and physical sizes.
- Table 2.1 Slopes of interference spectrums at the Q points for FPIs with different  $R_1$  and  $R_2$ .
- Table 3.1 Mechanical and thermal properties of silica (at 25 °C).
- Table 3.2 Values of  $\varphi_{mn}$ .
- Table 3.3 Values of the elastic modulus and the compliance modulus for graphite.
- Table 3.4 Mechanical and thermal properties of graphene.
- Table 3.5 Linear working ranges and pressure sensitivities of the graphene films with different values of the thickness and pre-stress.
- Table 3.6 Values of  $a_{mn}$  for the vibration modes.
- Table 3.7 Measured and calculated refractive indices for graphene and graphite.
- Table 4.1 Settings of the fusion current and duration for the tapering process.
- Table 5.1 List of the properties of the CVD graphene samples.
- Table 6.1 Coefficient  $\alpha$  for different values of  $W/d$ .
- Table 6.2 Physical parameters of the graphene beam and the nitrogen gas in the calculation.
- Table 6.3 Parameters for the fs fabrication.

# Chapter 1

## Introduction

### 1.1 Background review

Pressure monitoring has important applications in the areas of down-hole oil and gas exploration [1], automobile [2], and bio-medicine [3]. Pressure transducers usually detect pressure by two steps: firstly convert the pressure change into the elastic deformation of a flexible sensing element, and then convert the deformation into mechanical or electrical signals for easy readout or record. Conventional electrical pressure transducers include variable resistance transducers, capacitive transducers [4], piezoelectric and piezoresistive transducers [5].

Compared to their electrical counterparts, fiber optic pressure sensors (FOPSs) exhibit many advantages such as remote detection capability, high sensitivity, electromagnetic immunity, corrosion resistance and compact size [6]. These advantages make them especially competitive sensors in applications such as the automotive/aero engine monitoring, the oil extraction and undersea exploration, and the ultrasonic diagnosis and therapeutic treatment. Various types of FOPSs have been investigated for pressure (static and dynamic) detection. As light transmitted in the optical fiber can be modulated in aspects of intensity, wavelength, polarization and phase, FOPSs can be accordingly classified into four types: intensity modulation based FOPS, wavelength (spectrum) modulation based FOPS, polarization modulation based FOPS and phase modulation based FOPS.

### 1.1.1 Intensity modulation based FOPS

Intensity modulation based FOPSs (I-FOPSs) detect the pressure induced intensity change of light traveling in the fiber. One type of I-FOPSs is composed of a section of multi-mode fiber (MMF) which is embedded into two rigid mating plates, as shown in Fig. 1.1(a).

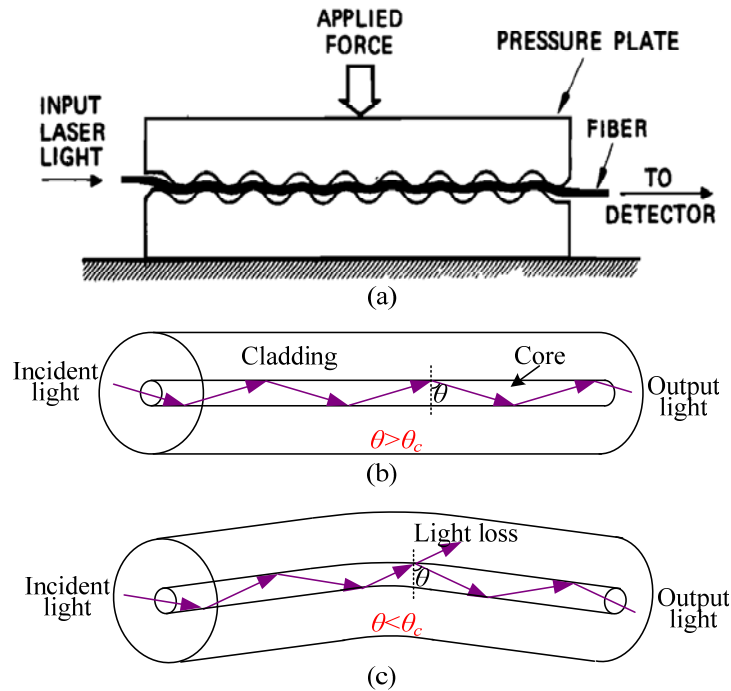


Fig. 1.1 Schematic of (a) a I-FOPS based on pressure induced bending loss [7]; (b) an undisturbed optical fiber; (c) an optical fiber with micro-bending.  $\theta$  and  $\theta_c$  are the incident angle and the critical angle of light in the optical fiber, respectively.

Fig. 1.1(b) plots an undisturbed optical fiber in which the light can transmit with negligible loss due to the total internal reflection. When the fiber is bended by the pressure applied on the upper plate, the induced micro-bending in the fiber couples the light from the core mode to the radiation modes. This mode-coupling corresponds to the case that the incident angle of the light  $\theta$  is larger than the critical angle of the fiber  $\theta_c$  if the light is regarded as light rays, as illustrated in Fig. 1.1(c). By detecting this coupling induced loss, a minimum detectable pressure level as small as 130  $\mu\text{Pa}$  has

been demonstrated by using a plate with size of 6 cm by 2.5 cm. The sensor has a simple configuration and is easy to demodulate, whereas it has a relatively large size [7].

It is known that acoustic pressure can periodically modulate the refractive index of medium (e.g. water). Consequently, the reflected light intensity from the fiber end surrounded by the medium would be also modulated according to the Fresnel formula. Based on this principle, a cleaved fiber end of a 100  $\mu\text{m}$ -diameter MMF has been reported to exhibit a pressure sensitivity of -302 dB (re 1V/ $\mu\text{Pa}$ ) [8]. Improvements of the pressure sensitivity and the frequency bandwidth of the sensor have been implemented by using a gold-coated fiber end [9] and a taper with a much decreased diameter [10], respectively. This type of sensors has a compact size, easy process of fabrication, and wide frequency bandwidth but relatively low pressure sensitivity.

Another type of I-FOPs makes use of a deflectable diaphragm placed close to the end of an optical fiber bundle. Light is delivered to the diaphragm by a transmitting fiber and the reflected light from the diaphragm is collected by the receiving fibers adjacent to the transmitting fiber in the fiber bundle. When there is pressure change, the diaphragm moves normally to the fiber end and modulates the light power level collected by the receiving fibers. A sensor with a 1.6 mm-diameter and 1.5  $\mu\text{m}$ -thick diaphragm demonstrates a minimum detectable pressure of 680  $\mu\text{Pa}/\text{Hz}^{1/2}$  over the frequency range from sub-hertz to 20 kHz [11]. This configuration shows a high pressure sensitivity which is determined by the amount of the pressure induced diaphragm deflection.

I-FOPs are simple in structure and easy to demodulate while they are sensitive to the variable loss in the whole interrogation system caused by, such as the splicing joint and connector, the micro-bending of the fiber, and the misalignment between the optical source and detector. Instability of the optical source also limits the long-term

stability of the sensor if no reference optical path is used.

## 1.1.2 Spectrum modulation based FOPS

Spectrum modulation based FOPSs (S-FOPSs) measure the pressure induced wavelength shift of light in the fiber. Typical examples of S-FOPSs are fiber gratings including the fiber Bragg grating (FBG) and the long period grating (LPG). The applied pressure changes the period of the grating and the refractive index of the fiber, both of which can induce the shift of the resonant wavelength of the grating [12].

### 1.1.2.1 Fiber Bragg gratings

The basic principle for the FBG based S-FOPS is schematically shown in Fig. 1.2. The reflection spectrum of the FBG exhibits a maximum intensity peak at the resonant wavelength  $\lambda_0$  which satisfies the resonant condition  $\lambda_0 = 2n_{eff}A$ , where  $n_{eff}$  is the effective refractive index of the fundamental mode of the optical fiber, and  $A$  is the period of the grating as shown in Fig. 1.2(a).

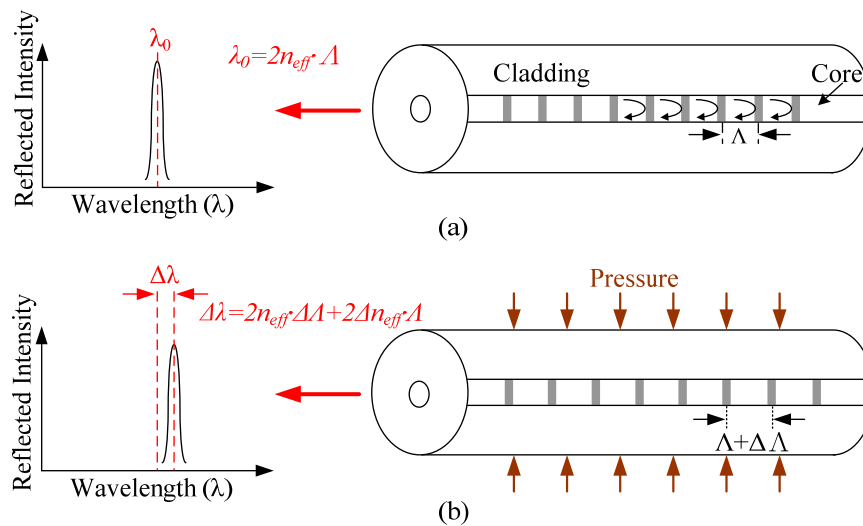


Fig. 1.2 Schematic of a FBG and its reflection spectrum (a) without and (b) with pressure;  $\lambda_0$ : the resonant wavelength,  $\Delta\lambda$ : the resonant wavelength change,  $n_{eff}$ : the effective refractive index,  $A$ : the grating period,  $\Delta A$ : change of the grating period,  $\Delta n_{eff}$ : change of the effective refractive index.

When the FBG experiences pressure, the effective refractive index  $n_{eff}$  and the grating period  $\Lambda$  will change due to the photoelastic effect and the pressure induced axial strain in the fiber, respectively. The relationship between the resonant wavelength change  $\Delta\lambda$  and the effective refractive index change  $\Delta n_{eff}$  and the grating period change  $\Delta\Lambda$  is given in Fig. 1.2(b). A FBG written holographically by UV light in a bare single mode fiber (SMF) has demonstrated a pressure sensitivity of  $3.1 \times 10^{-3}$  nm/Mpa [13]. The low pressure sensitivity could be improved by coating the fiber with elastomeric material or packaging the fiber with a sensitivity-enhanced structure [14-16]. For example, after being embedded into a silicon rubber, the FBG shows a significantly increased pressure sensitivity of 5.28 nm/Mpa, which is about three orders of magnitude higher than that of the FBG in a bare SMF. To alleviate the large temperature cross-sensitivity of the embedded FBG caused by the thermal expansion of the rubber or polymer, a partly embedded FBG which exhibits two separated resonant wavelengths was developed to simultaneously measure the pressure and temperature [17].

FBGs have also been written in microstructure fibers to increase the pressure sensitivity instead of using the bulky and complicated package [18, 19]. The FBG in the microstructure fiber with an air hole diameter of  $\sim 33.8 \mu\text{m}$  and a core diameter of  $\sim 8 \mu\text{m}$  has shown a higher pressure sensitivity of  $\sim 13$  pm/Mpa [18]. Simultaneous measurement of the pressure and temperature was realized by writing the FBG in a high-birefringence (Hi-Bi) microstructure fiber [19]. This FBG exhibits two polarization-dependent resonant peaks at different wavelengths in the reflection spectrum and the two resonant peaks show similar responses to temperature but different responses to pressure. In addition, a dual-polarization fiber grating laser has recently been developed to detect the pressure by measuring the beating frequency of the two polarization mode of the laser. The measurement is performed by using the well-developed demodulation technique for the radio frequency (RF) test, instead of

measuring the reflection spectrum by an optical spectrum analyzer (OSA) [20].

### **1.1.2.2 Long period gratings**

LPGs couple light from the core mode to the cladding mode at the resonant wavelength and are more sensitive to outside environment compared to FBGs [12]. A LPG fabricated into a SMF by using the electric arc discharge demonstrates a pressure sensitivity of 51 pm/Mpa, which is  $\sim 16$  times higher than that reported for the FBG without a sensitivity-enhanced package [21]. LPGs have also been fabricated in the polymer microstructure fiber and the silica photonic crystal fiber (PCF) [22, 23]. The LPG inscribed in the silica PCF exhibits a higher pressure sensitivity of 112 pm/Mpa and a substantially reduced temperature sensitivity of 0.35 pm/ $^{\circ}$ C (49.5 pm/ $^{\circ}$ C for the LPG in a SMF).

SFOPSSs based on fiber gratings possess advantages of the immunity to the variable loss of the optical power in the system and the capability for multiplexing (for FBGs). However, the gratings show inherently limited pressure sensitivities as well as large cross-sensitivities to other environment parameters such as the temperature and bending, which limit the scale of the S-FOPSSs employed for practical pressure measurements.

## **1.1.3 Polarization modulation based FOPS**

Polarization modulation based FOPSSs measure the pressure induced birefringence change of the fiber through the photoelastic effect. The fiber core experiences pressure induced anisotropic stress due to the asymmetric structure of the fiber. The anisotropic stress induces birefringence change of the fiber and the change can be measured by the polarimetric interference [24-27] with the configuration illustrated in Fig. 1.3(a).

A bow-tie HB 800 Hi-Bi fibers with a birefringence of  $0.37 \times 10^{-3}$  (Fig. 1.3(b)) has demonstrated a pressure sensitivity of 9.6 rad/(Mpa·m) and a maximum working

pressure of 200 MPa [25]. Recently developed fiber-drawing techniques provide the feasibility to design Hi-Bi microstructure fibers with optimized geometries to maximize the pressure sensitivity [27]. Based on these Hi-Bi microstructure fibers, a number of miniature pressure sensors have been developed [28-30]. For example, Fu et al. fabricated a Sagnac loop interferometer by coiling the polarization maintaining PCF (Fig. 1.3(c)) onto a 5 mm-diameter circle. The sensor has a compact structure and a high pressure sensitivity of 3.42 nm/Mpa [28]. Anuszkiewicz et al. reported a rocking filter written in the Hi-Bi PCF (Fig. 1.3(d)) and the sensor demonstrated a high pressure sensitivity of up to  $\sim 177$  nm/Mpa [30].

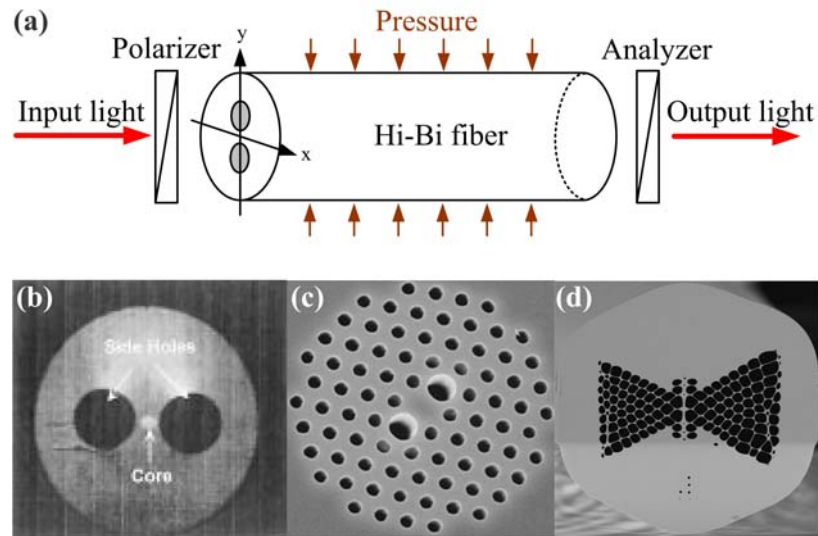


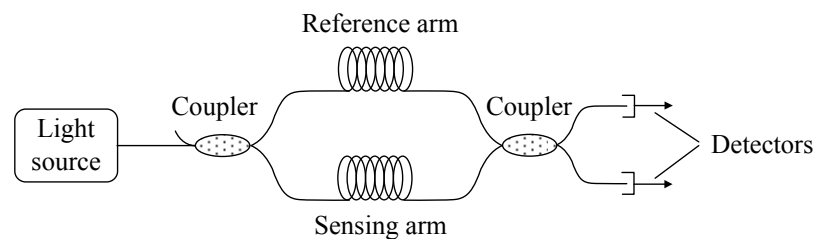
Fig. 1.3 (a) Schematic of a Hi-Bi fiber based FOPS. Images of (b) a side-hole fiber [25]; (c) a polarization maintaining PCF [28]; (d) a Hi-Bi microstructure fiber [30].

#### 1.1.4 Phase modulation based FOPS

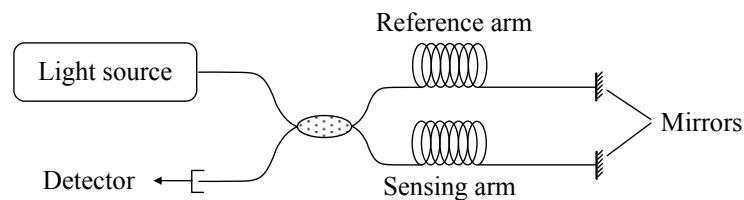
For FOPSs based on phase modulation (P-FOPSs), the pressure induces variations of the fiber length (i.e, the cavity length) and/or the refractive index of the fiber, both of which can change the phase of light in the fiber. The conventional configurations for P-FOPSs include Michelson, Mach-Zehnder, Sagnac loop and Fabry-Perot interferometers.

### 1.1.4.1 Michelson and Mach-Zehnder interferometers

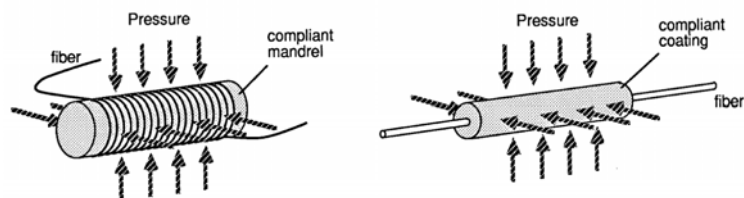
Mach-Zehnder interferometer (MZI) and Michelson interferometer (MI) are both comprised of two arms: the reference arm in which the light acts as a reference and the sensing arm in which the phase of light is modulated by the applied pressure, as shown in Fig. 1.4(a) and (b). For the MZI, one coupler is used to split the light from the optical source into two paths and the other coupler is used to combine the light from the two paths into the detector to form interference. For the MI, only one coupler is used, and the light is split into two paths after passing the coupler and then reflected back to the same paths by two reflective mirrors. The reflected lights from the two paths are then combined after passing through the same coupler again.



(a) Mach-Zehnder interferometer



(b) Michelson interferometer



(c) Acoustically designed mandrel and coating

Fig. 1.4 Schematic of the configurations of (a) the Mach-Zehnder interferometer and (b) the Michelson interferometer; (c) the acoustically designed mandrel and coating for the pressure sensitivity enhancement [33].

The pressure can be detected by measuring the phase difference between the reference arm and the sensing arm by different demodulation methods [31]. For a SMF based MZI, it shows a dynamic pressure (acoustic) sensitivity of  $2.5 \times 10^{-11} L/\lambda$  rad/Pa with  $L$  and  $\lambda$  denoting the fiber length and the light wavelength, respectively [32]. Improved sensitivities of the MZI have been achieved by either embedding the sensing arm into a sensitivity-enhanced composite/structure (Fig. 1.4(c)) or by applying the hollow-core photonic bandgap fiber (HC-PBF) as the sensing arm [33-34]. The HC-PBF is selected due to its lower effective Young's modulus and higher axial strain under pressure, compared to the conventional SMF. Recently, the sensitivity of the HC-PBF based MZI has been further increased by etching away the silica cladding outside the air hole array of the HC-PBF and subsequently coating the etched fiber with a layer of polymer [35].

The MI can be considered as the folded MZI with two reflective mirrors at the two arm ends. Compared to the MZI, the MI works in a reflective mode and its structure is more compact as just one coupler is required. The pressure sensitivity of the MI is twice larger than that of the MZI since the light travels forth and back in the sensing arm. On the other hand, the noise of the MI has increased due to the light reflections induced by the Rayleigh backscatter [36].

#### **1.1.4.2 Sagnac loop interferometers**

Sagnac loop interferometer has two light beams traveling within one close fiber loop in opposite directions. The two beams form phase difference since they reach the fiber part activated by the acoustic wave at different times. The Sagnac loop with a passive homodyne detection scheme has shown a noise-equivalent phase shift of  $2.5 \times 10^{-7}$  rad/Hz<sup>1/2</sup> [37]. This low phase noise benefits from the same optical fiber loop which the two light beams travel through.

### 1.1.4.3 Fabry-Perot Interferometers

The structure of Fabry-Perot interferometers (FPIs) is generally comprised of two reflective mirrors, which can be a fiber endface, a FBG, or an elastic diaphragm. The two reflected light beams interfere and generate periodic fringes in the interference spectrum due to their phase (the optical path) difference.

Fig. 1.5(a) shows a simple configuration of FPIs with the Fabry-Perot cavity formed by inserting a section of capillary (Fig. 1.5(b)) between two SMFs [38, 39]. The microstructure fiber, such as the simplified HC-PBF (Fig. 1.5(c)) and the HC-PBF (Fig. 1.5(d)) have also been used to replace the capillary for pressure sensing. A detailed investigation of the pressure response of those different types of fibers has been conducted in [40]. In addition to the fiber end/air interface, FBGs and metal films have been used as the reflective mirrors for the construction of high-finesse FPIs [41]. For the FPIs as mentioned, the deformation or elongation of the cavity, normally the optical fiber itself, determines the pressure sensitivity of the sensor.

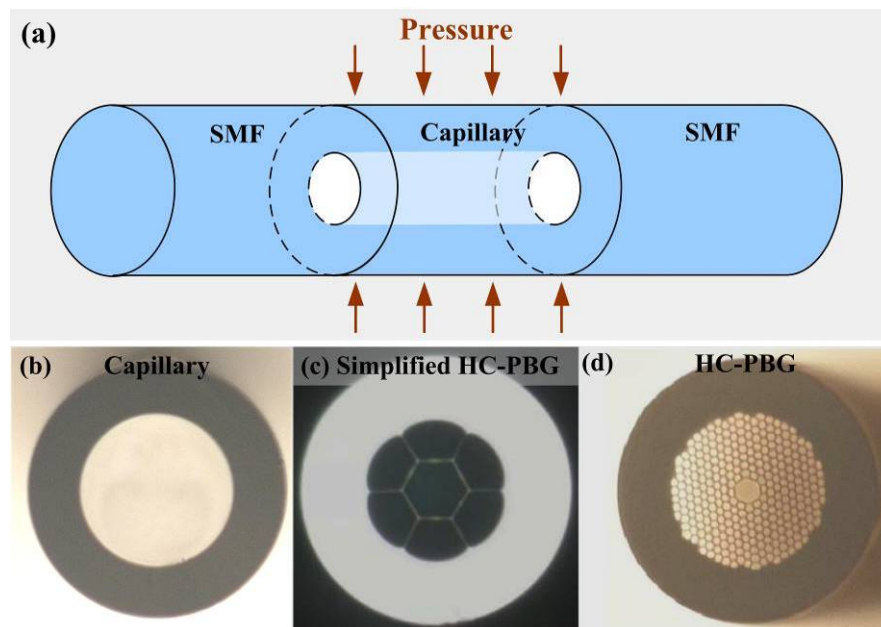


Fig. 1.5 (a) Schematic of a FPI with a section of capillary as the Fabry-Perot cavity; cross-section images of (b) a capillary; (c) a simplified HC-PBF; (d) a HC-PBF.

In addition to the pressure sensor using a section of fiber as the sensing element, the FPI with a movable diaphragm positioned at the end of the sensor head (the diaphragm based FPIs) represents an important class of FOPSs [42]. Applied static/acoustic pressure causes the deflection of the clamped diaphragm, which can be interrogated in a reflection mode with intensity or interferometric techniques [43].

According to the relation,  $\Delta L/\Delta P \sim a^4/t^3 E$ , the deflection of the diaphragm  $\Delta L$  to unit pressure  $\Delta P$  is proportional to the fourth power of the diameter  $a$ , and inversely proportional to the cube of the thickness  $t$  and the Young's modulus  $E$  of the diaphragm. If the pressure sensitivity of the diaphragm might be defined as the ratio of the diaphragm deflection to the pressure, increasing the size or decreasing the thickness of the diaphragm can significantly increase its pressure sensitivity [44]. Obviously, the latter method, i.e., decreasing the diaphragm thickness, is preferred for the sake of the compactness of the sensor. Significant progress has been made in developing fiber-tip pressure and acoustic sensors with a high sensitivity and a miniature size [45-49]. Fig. 1.6(a-c) show several diaphragm based FPIs with different diaphragms and structures.

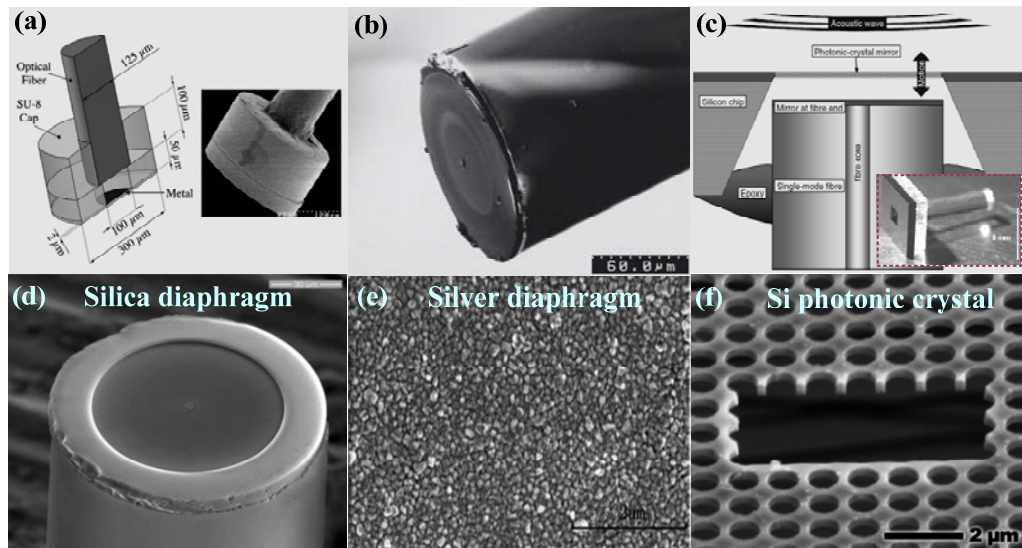


Fig. 1.6 (a) a FPI pressure sensor with a polymer (SU-8) diaphragm; (b) a fiber-tip FPI pressure sensor with a silica diaphragm; (c) a FPI acoustic sensor with a silicon photonic crystal diaphragm; (d) a silica diaphragm; (e) a silver diaphragm; (f) a silicon photonic crystal diaphragm.

Xu et al. [45] reported an all-silica fiber-tip FPI pressure sensor that uses a diaphragm with a thickness of a few microns and a diameter of 158  $\mu\text{m}$ , and the measured pressure sensitivity is 0.57 nm/kPa. Cibula et al. [48] developed a similar pressure sensor by using a silica diaphragm with a diameter of 90  $\mu\text{m}$  and a thickness down to 2  $\mu\text{m}$  or less. The thickness of the diaphragm is controlled by an online chemical etching technique. The pressure sensitivity achieved by the 2  $\mu\text{m}$  diameter diaphragm is 5.5 nm/kPa. Wang et al. [49] reported a pressure sensor with a higher pressure sensitivity of 11 nm/kPa; the sensor has an outer diameter of 125  $\mu\text{m}$  and uses a silica diaphragm with a thickness of 0.75  $\mu\text{m}$  and a diameter of 65  $\mu\text{m}$ .

In the above works, the silica (Fig. 1.6(d)) is selected as the diaphragm material due to the same thermal expansion coefficient as that of the optical fiber, which can reduce the thermal expansion stress in the sensor structure and thus improve the temperature stability and mechanical strength of the sensor.

In addition to silica, diaphragms made of other materials have also been used for sensitive pressure/acoustic sensors [50-56], such as the silver (see Fig. 1.6(e)) and the silicon photonic crystal (see Fig. 1.6(f)). Xu et al. transferred a 100 nm thick silver film onto a ferrule endface with an air cavity diameter of 125  $\mu\text{m}$  and the sensor shows a high pressure sensitivity of  $\sim 70.5$  nm/kPa [51]. Later, Guo et al. built a real fiber-tip pressure sensor on a fiber capillary with an outer diameter of 125  $\mu\text{m}$  and an inner hole diameter of 75  $\mu\text{m}$  with a similar silver film [52]. For acoustic detections, Gander et al. [54] described fiber-tip FPI sensors made of a copper diaphragm with a thickness of  $\sim 2$   $\mu\text{m}$  and a diameter of 50-100  $\mu\text{m}$ ; the sensors exhibits a minimum detectable pressure (MDP) of 900 mPa/Hz<sup>1/2</sup> at 8 kHz and a pressure sensitivity of 1.6 rad/bar at 1550 nm ( $\sim 2$  nm/kPa). Kilic et al. [56] demonstrated a fiber-tip acoustic FPI sensor formed by placing a silicon photonic-crystal slab (PCS) mirror in close proximity to the chromium/gold coated reflective tip of a SMF. The PCS acts as a thin diaphragm that deflects with the applied acoustic pressure wave. Both the coated fiber end and

the PCS diaphragm (mirror) have the reflectivity of  $\sim 75\%$ , forming a high-finesse FPI. The diaphragm is a  $150\ \mu\text{m} \times 150\ \mu\text{m}$  square-shape membrane with a thickness of  $\sim 450\ \text{nm}$ . The dynamic (acoustic) pressure test suggests a sensitivity of  $\sim 1000\ \text{nm/kPa}$  and a relatively uniform frequency response up to  $50\ \text{kHz}$ . Based on a similar structure, a miniature fiber hydrophone demonstrated a MDP of  $\sim 10\ \mu\text{Pa/Hz}^{1/2}$  at  $30\ \text{kHz}$  [57].

The ultra-high sensitivity of the acoustic sensor reported by Kilic et al. attributes to the large pressure sensitivity of the diaphragm as well as the high finesse of the Fabry-Perot cavity. Increasing of the finesse, i.e., the slope of the intensity/phase function (interference spectrum) of the FPI, is an alternative to improve the pressure sensitivity of the sensor and can be achieved by coating the reflective mirrors of the FP cavity with high-reflectivity films (e.g., gold).

Table 1.1 lists the pressure sensitivities of several FPIs with diaphragms of different materials and physical sizes (diameter and thickness).

Table 1.1 Pressure sensitivities of FPIs with diaphragms of different materials and physical sizes.

<b>Diaphragm material</b>	<b>Diameter (<math>\mu\text{m}</math>)</b>	<b>Thickness (<math>\mu\text{m}</math>)</b>	<b>Pressure sensitivity (nm/kPa)</b>	<b>Year</b>
Silica	158	5.5~6	0.57	2005 <sup>[45]</sup>
	90	2	5.5	2009 <sup>[48]</sup>
	65	0.75	11	2010 <sup>[49]</sup>
Silver	125	0.13	70.5	2012 <sup>[51]</sup>
	75	0.3	1.6	2012 <sup>[52]</sup>
Copper	50-100	2	2	2003 <sup>[54]</sup>
Silicon	150*	0.5	1000	2007 <sup>[56]</sup>

\*Note: the silicon diaphragm has a square shape with length and width of  $150 \times 150\ \mu\text{m}$ .

The pressure information carried by the diaphragm in the form of the deflection is demodulated and transformed into electrical signals for readout. A number of approaches have been developed for the interrogation of the FPI, such as the phase generated carrier homodyne [58],  $3 \times 3$  coupler, linear (or quadrature), and homodyne and heterodyne demodulation [59].

Two simple methods are widely used in the laboratory for testing the performance

of the fabricated pressure sensors. The first one which directly reads the pressure induced wavelength shift of the interference spectrum of the FPI, is usually adopted in the static pressure measurement. The second one, called the linear demodulation or quadrature (Q) demodulation, measures the linear intensity change of the reflected light from the FPI subjected to the dynamic (or acoustic) pressure. To achieve a maximum sensitivity and linear response, the central wavelength of the tunable laser should match with the Q point wavelength of the interference spectrum [46]. Possible schemes for dynamically tuning the central wavelength of the laser such as adjusting the DFB laser temperature or rotating a diffraction grating in combination of a feedback circuit have been proposed [60, 61]. Recently, a novel FPI with a microstructure fiber as the lead in/out fiber demonstrates the capability of tuning the Q point instead of the central wavelength of the laser. This is realized by controlling the gas pressure in the FP cavity which is connected to an air pressure controller by the hole of the microstructure fiber [62].

Compared to other types of FOPSs, the diaphragm-based FPIs exhibit advantages, such as high sensitivity and large bandwidth, immunity to polarization fading, and compact size of the sensor head. Through field tests for pressure/acoustic monitoring in engines and electrical power transformers [46, 54], the diaphragm-based FPIs have proven themselves promising for a variety of practical applications.

## **1.2 Research motivation and significance**

Although numerous techniques have been developed to fabricate diaphragm-based FPIs, these techniques suffer from several drawbacks: the fabrication processes are complicated and involve multiple steps such as cleaving, polishing, chemical etching and bonding; the FPIs are assembled by multi-parts with different structures and/or materials, which deteriorates their mechanical strength and thermal stability. To achieve a simpler and more cost-effective fabrication process for practical

applications, we have developed a simple and low-cost technique to fabricate compact fiber-tip micro-cavity FPIs. As the micro-cavity is directly melted into the fiber end, the micro-cavity based FPI has an all-silica structure and involves no assembly. The advantages such as the good mechanical strength and high temperature sustainability make these sensors promising for pressure measurements in harsh environments.

Considerable efforts have been made to fabricate miniature and high-sensitivity diaphragm-based FPIs with thin diaphragms. The thickness of the diaphragm, however, is limited to submicron scale by the fabrication technique and the mechanical strength of the material itself. We have for the first time explored the use of the graphene, the thinnest and strongest material, as the diaphragm to build fiber-tip FPIs for highly sensitive pressure measurements. A technique for transferring the graphene film has been developed. The graphene based FPI pressure sensor with a much smaller diaphragm demonstrates a pressure sensitivity at the same level with the highest reported value; the graphene based FPI acoustic sensor demonstrates a record-breaking acoustic pressure sensitivity compared to the FPIs with similar diaphragm sizes.

Suspended graphene sheets represent the thickness limit of the two-dimensional micro-mechanical resonators. The graphene with a low mass and large surface area is ideally suitable for ultra-sensitive mass and force detection. However, the graphene based resonators reported to date are mostly developed on the silicon substrate and have a bulky interrogation system. We have integrated the graphene with the optical fiber to construct a miniature micro-mechanical resonator. The resonator can be optically excited and interrogated by the use of an all-fiber system without the electrical actuation and bulky desktop system. The detection scheme requires no sealed cavity, which makes this resonator based pressure sensor inherently immune to the possible diaphragm fatigue. Compared to the silicon cantilever, the sensor shows a pressure sensitivity of  $\sim$  one order of magnitude higher. In addition to the pressure

detection, the micro-mechanical resonator is promising for ultra-low mass and force detection.

## 1.3 Thesis outline

The thesis is organized as follows:

**Chapter 2** introduces the basic principles of FPIs including the interference spectrum, fringe contrast and effect of the diaphragm thickness on the interference spectrum. The demodulation, noise source and noise equivalent pressure level of the FPI are also briefly discussed.

**Chapter 3** discusses the mechanical responses of silica and graphene diaphragms subjected to static and dynamic pressures. The general parameters for the evaluation of a diaphragm-based pressure sensor as well as the production and identification of the graphene diaphragm are introduced. Finally, the optical reflectivity of the graphene diaphragm is studied in detail.

**Chapter 4** presents a novel all-silica Fabry-Perot micro-cavity at the fiber tip for pressure measurements. The fabrication process of the micro-cavity and the pressure-assisted tapering process for the pressure sensitivity enhancement are described. Then the interference spectrum of the micro-cavity is studied by the use of a three-beam interference model. This is followed by the experimental and theoretical investigations of the pressure and temperature responses of the micro-cavity.

**Chapter 5** demonstrates the graphene diaphragm based pressure/acoustic sensors. After the illustration of the preparation, transferring, and characterization of the graphene films, two types of the pressure/acoustic sensors including a fiber-tip FPI with a few-layer graphene diaphragm and a ferrule-top FPI with a multilayer graphene diaphragm are presented. Their fabrication, interrogation, and test of the pressure and/or temperature response are studied in detail. Finally, a noise analysis of the ferrule-top FPI for the acoustic detection is given.

**Chapter 6** presents the graphene diaphragm based micro-mechanical resonators for pressure detection. After a brief review of the micro-mechanical resonators, a harmonically excited oscillator with damping is theoretically studied. This forms the basis for the following analysis of air damping effects on a thin beam resonator in terms of the resonant frequency and quality factor. The fabrication of the ferrule-top resonator with the graphene film as well as the optical excitation and interrogation of the resonator are also described. To improve the performance of the resonator with a circular graphene diaphragm for pressure measurements, a beam-shape graphene resonator is developed and the dependence of its quality factor and resonant frequency on air pressure is investigated.

**Chapter 7** gives the general conclusion and several suggestions for future work.

## References for Chapter 1

- [1] A. D. Kersey, "Optical fiber sensors for permanent downwell monitoring applications in the oil and gas industry," *IEICE Trans. Electron.* E83-C, 400-404 (2000).
- [2] W. J. Pulliam, P. M. Russler, and R. S. Fielder, "High-temperature high-bandwidth fiber optic MEMS pressure-sensor technology for turbine engine component testing," in *Proc. SPIE 4578, Fiber Optic Sensor Technology and Applications*, 229-238, Feb 2001.
- [3] O. Tohyama, M. Kohashi, M. Sugihara, and H. Itoh, "A fiber-optic pressure microsensor for biomedical applications," *Sensors Actuators A.* 66, 150-154 (1998).
- [4] D. Goustouridis, P. Normand, and D. Tsoukalas, "Ultraminiature silicon capacitive pressure-sensing elements obtained by silicon fusion bonding," *Sensors Actuators A.* 68, 269-274 (1998).
- [5] P. Melvas, E. Kalvesten, P. Enoksson, and G. Stemme, "A free-hanging strain-gauge for ultraminiaturized pressure sensors," *Sensors Actuators A.* 97-98, 75-82 (2002).
- [6] B. Lee, "Review of the present status of optical fiber sensors," *Opt. Fiber Technol.* 9, 57-79 (2003).
- [7] J. N. Fields, C. K. Asawa, O. G. Ramer, and M. K. Barnoski, "Fiber Optic Pressure Sensor," *J. Acoust. Soc. Am.* 67, 816-818 (1980).
- [8] J. E. Parsons, C. A. Cain, and J. B. Fowlkes, "Cost-effective assembly of a

- basic fiber-optic hydrophone for measurement of high-amplitude therapeutic ultrasound fields,” *J. Acoust. Soc. Am.* 119, 1432-1440 (2006).
- [9] R. G. Minasamudram, P. Arora, G. Gandhi, A. S. Daryoush, M. A. El-Sherif, and P. A. Lewin, “Thin film metal coated fiber optic hydrophone probe,” *Appl. Opt.* 48, G77-G82 (2009).
- [10] P. A. Lewin, C. Mu, S. Umchid, A. Daryoush, and M. El-Sherif, “Acousto-optic, point receiver hydrophone probe for operation up to 100 MHz,” *Ultrasonics* 43, 815-821 (2005).
- [11] J. A. Bucaro, N. Lagakos, B. H. Houston, J. Jarzynski, and M. Zalalutdinov, “Miniature, high performance, low-cost fiber optic microphone,” *J. Acoust. Soc. Am.* 118, 1406-1413 (2005).
- [12] T. Erdogan, “Fiber grating spectra,” *J. Lightwave Technol.* 15, 1277-1294 (1997).
- [13] M. Xu, L. Reekie, Y. Chow, and J. P. Dakin, “Optical in-fibre grating high pressure sensor,” *Electron. Lett.* 29, 398-399 (1993).
- [14] M. Xu, H. Geiger, and J. Dakin, “Fibre grating pressure sensor with enhanced sensitivity using a glass-bubble housing,” *Electron. Lett.* 32, 128-129 (1996).
- [15] Y. Zhang, D. J. Feng, Z. G. Liu, Z. Y. Guo, X. Y. Dong, K. S. Chiang, and B. C. Chu, “High-sensitivity pressure sensor using a shielded polymer-coated fiber Bragg grating,” *IEEE Photon. Technol. Lett.* 13, 618-619 (2001).
- [16] D. Hill and G. Cranch, “Gain in hydrostatic pressure sensitivity of coated fibre Bragg grating,” *Electron. Lett.* 35, 1268-1269 (1999).
- [17] Y. Q. Liu, Z. Y. Guo, Y. Zhang, K. S. Chiang, and X. Y. Dong, “Simultaneous pressure and temperature measurement with polymer-coated fibre Bragg grating,” *Electron. Lett.* 36, 564-566 (2000).
- [18] C. Wu, B. O. Guan, Z. Wang, and X. H. Feng, “Characterization of Pressure Response of Bragg Gratings in Grapefruit Microstructured Fibers,” *J. Lightwave Technol.* 28, 1392-1397 (2010).
- [19] E. Chmielewska, W. Urbańczyk, and W. J. Bock, “Measurement of pressure and temperature sensitivities of a Bragg grating imprinted in a highly birefringent side-hole fiber,” *Appl. Opt.* 42, 6284-6291 (2003).
- [20] B. O. Guan, Y. N. Tan, and H. Y. Tam, “Dual polarization fiber grating laser hydrophone,” *Optics Express* 17, 19544-19550 (2009).
- [21] W. J. Bock, J. Chen, P. Mikulic, and T. Eftimov, “A novel fiber-optic tapered long-period grating sensor for pressure monitoring,” *IEEE Trans. Instrum. Meas.* 56, 1176-1180 (2007).
- [22] G. Statkiewicz-Barabach, D. Kowal, M. K. Szczurowski, P. Mergo, and W. Urbanczyk, “Hydrostatic Pressure and Strain Sensitivity of Long Period Grating Fabricated in Polymer Microstructured Fiber,” *IEEE Photon. Technol. Lett.* 25, 496-499 (2013).
- [23] W. J. Bock, J. Chen, P. Mikulic, T. Eftimov, and M. Korwin-Pawlowski, “Pressure sensing using periodically tapered long-period gratings written in photonic crystal fibres,” *Meas. Sci. Technol.* 18, 3098-3102 (2007).
- [24] H. Xie, P. Dabkiewicz, R. Ulrich, and K. Okamoto, “Side-hole fiber for fiber-optic pressure sensing,” *Opt. Lett.* 11, 333-335 (1986).
- [25] W. J. Bock, “High-Pressure Polarimetric Sensor Using Birefringent Optical

- Fibers,” *IEEE Trans. Instrum. Meas.* 39, 233-237 (1990).
- [26] J. R. Clowes, S. Syngellakis, and M. N. Zervas, “Pressure sensitivity of side-hole optical fiber sensors,” *IEEE Photon. Technol. Lett.* 10, 857-859 (1998).
- [27] T. Martynkien, G. Statkiewicz-Barabach, J. Olszewski, J. Wojcik, P. Mergo, T. Geernaert, C. Sonnenfeld, A. Anuszkiewicz, M. K. Szczurowski, and K. Tarnowski, “Highly birefringent microstructured fibers with enhanced sensitivity to hydrostatic pressure,” *Optics Express* 18, 15113-15121 (2010).
- [28] H. Fu, H. Tam, L. Shao, X. Dong, P. Wai, C. Lu, and S. Khijwania, “Pressure sensor realized with polarization-maintaining photonic crystal fiber-based Sagnac interferometer,” *Appl. Opt.* 47, 2835-2839 (2008).
- [29] R. Kaul, “Pressure sensitivity of rocking filters fabricated in an elliptical-core optical fiber,” *Opt. Lett.* 20, 1000-1001 (1995).
- [30] A. Anuszkiewicz, G. Statkiewicz-Barabach, T. Borsukowski, J. Olszewski, T. Martynkien, W. Urbanczyk, P. Mergo, M. Makara, K. Poturaj, T. Geernaert, F. Berghmans, and H. Thienpont, “Sensing characteristics of the rocking filters in microstructured fibers optimized for hydrostatic pressure measurements,” *Optics Express* 20, 23320-23330 (2012).
- [31] C. K. Kirkendall and A. Dandridge, “Overview of high performance fibre-optic sensing,” *J. Phys. D: Appl. Phys.* 37, R197-R216 (2004).
- [32] G. B. Hocker, “Fiber-optic sensing of pressure and temperature,” *Appl. Opt.* 18, 1445-1448 (1979).
- [33] G. B. Hocker, “Fiber-optic acoustic sensors with increased sensitivity by use of composite structures,” *Opt. Lett.* 4, 320-321 (1979).
- [34] M. Pang and W. Jin, “Detection of acoustic pressure with hollow-core photonic bandgap fiber,” *Optics Express* 17, 11088-11097 (2009).
- [35] F. Yang, W. Jin, H. L. Ho, F. Wang, W. Liu, L. Ma, and Y. Hu, “Enhancement of acoustic sensitivity of hollow-core photonic bandgap fibers,” *Optics Express* 21, 15514-15521 (2013).
- [36] M. J. Marrone, A. D. Kersey, C. A. Villarruel, C. K. Kirkendall, and A. Dandridge, “Elimination of Coherent Rayleigh Backscatter Induced Noise in Fiber Michelson Interferometers,” *Electron. Lett.* 28, 1803-1804 (1992).
- [37] K. Kråkenes and K. Bløtekjaer, “Sagnac interferometer for underwater sound detection: noise properties,” *Opt. Lett.* 14, 1152-1154 (1989).
- [38] J. S. Sirkis, D. D. Brennan, M. A. Putman, T. A. Berkoff, A. D. Kersey, and E. J. Friebele, “In-Line Fiber Etalon for Strain-Measurement,” *Opt. Lett.* 18, 1973-1975 (1993).
- [39] D. Wang, S. Wang, and P. Jia, “In-line silica capillary tube all-silica fiber-optic Fabry–Perot interferometric sensor for detecting high intensity focused ultrasound fields,” *Opt. Lett.* 37, 2046-2048 (2012).
- [40] L. Jin, B.-O. Guan, and H. Wei, “Sensitivity Characteristics of Fabry-Perot Pressure Sensors Based on Hollow-Core Microstructured Fibers,” *J. Lightwave Technol.* 31, 2526-2532 (2013).
- [41] S. E. U. Lima, O. Frazao, R. G. Farias, F. M. Araujo, L. A. Ferreira, V. Miranda, and J. L. Santos, “Intrinsic and extrinsic fiber fabry perot sensors for acoustic detection in liquids,” *Microw. Opt. Technol. Lett.* 52, 1129-1134 (2010).

- [42] Q. Yu and X. Zhou, "Pressure sensor based on the fiber-optic extrinsic Fabry-Perot interferometer," *Photon. Sensors* 1, 72-83 (2011).
- [43] C. Zhou, S. V. Letcher, and A. Shukla, "Fiber-optic microphone based on a combination of Fabry-Perot interferometry and intensity modulation," *J. Acoust. Soc. Am.* 98, 1042-1046 (1995).
- [44] M. D. Giovanni, "Flat and Corrugated Diaphragm Design Handbook," Marcel Dekker (1982).
- [45] J. Xu, X. Wang, K. Cooper, and A. Wang, "Miniature all-silica fiber optic pressure and acoustic sensors," *Opt. Lett.* 30, 3269-3271 (2005).
- [46] B. Yu, D. W. Kim, J. Deng, H. Xiao, and A. Wang, "Fiber Fabry-Perot sensors for detection of partial discharges in power transformers," *Appl. Opt.* 42, 3241-3250 (2003).
- [47] Y. Zhu, K. Cooper, G. Pickrell, and A. Wang, "High-temperature fiber-tip pressure sensor," *J. Lightwave Technol.* 24, 861-869 (2006).
- [48] E. Cibula, S. Pevec, B. Lenardic, E. Pinet, and D. Donlagic, "Miniature all-glass robust pressure sensor," *Opt. Express* 17, 5098-5106 (2009).
- [49] W. Wang, N. Wu, Y. Tian, C. Niezrecki, and X. Wang, "Miniature all-silica optical fiber pressure sensor with an ultrathin uniform diaphragm," *Opt. Express* 18, 9006-9014 (2010).
- [50] E. Cibula and D. Donlagic, "Miniature fiber-optic pressure sensor with a polymer diaphragm," *Appl. Opt.* 44, 2736-2744 (2005).
- [51] F. Xu, D. Ren, X. Shi, C. Li, W. Lu, L. Lu, L. Lu, and B. Yu, "High-sensitivity Fabry-Perot interferometric pressure sensor based on a nanothick silver diaphragm," *Opt. Lett.* 37, 133-135 (2012).
- [52] F. Guo, T. Fink, M. Han, L. Koester, J. Turner, and J. Huang, "High-sensitivity, high-frequency extrinsic Fabry-Perot interferometric fiber-tip sensor based on a thin silver diaphragm," *Opt. Lett.* 37, 1505-1507 (2012).
- [53] L. Chen, C. Chan, W. Yuan, S. Goh, and J. Sun, "High performance chitosan diaphragm-based fiber-optic acoustic sensor," *Sensors Actuators A*. 163, 42-47 (2010).
- [54] W. N. M. Matthew J. Gander, James S. Barton, R. L. Reuben, Julian D. C. Jones, R. Stevens, Kam S. Chana, S. J. Anderson, and T. V. Jones, "Embedded micromachined fibre-optic Fabry-Perot pressure sensors in aerodynamics applications," *IEEE Sens. J.* 3, 102-107 (2003).
- [55] Q. Wang and Q. Yu, "Polymer diaphragm based sensitive fiber optic Fabry-Perot acoustic sensor," *Chin. Phys. Lett.* 8, 266-269 (2010).
- [56] O. Kilic, M. Digonnet, G. Kino, and O. Solgaard, "External fibre Fabry-Perot acoustic sensor based on a photonic-crystal mirror," *Meas. Sci. Technol.* 18, 3049 (2007).
- [57] O. Kilic, M. J. F. Digonnet, G. S. Kino, and O. Solgaard, "Miniature photonic-crystal hydrophone optimized for ocean acoustics," *J. Acoust. Soc. Am.* 129, 1837-1850 (2011).
- [58] A. Dandridge, A. B. Tveten, and T. G. Giallorenzi, "Homodyne Demodulation Scheme for Fiber Optic Sensors Using Phase Generated Carrier," *IEEE J. Quant. Electron.* 18, 1647-1653 (1982).
- [59] T. G. Giallorenzi, J. A. Bucaro, A. Dandridge Jr, G. Sigel, J. H. Cole, S. C.

- Rashleigh, and R. G. Priest, "Optical fiber sensor technology," *IEEE J. Quant. Electron.* 30, 472-511 (1982).
- [60] J. Chen, W. Li, H. Jiang, and Z. Li, "Stabilization of a fiber Fabry-Perot interferometric acoustic wave sensor," *Microw. Opt. Technol. Lett.* 54, 1668 (2012).
- [61] B. Yu and A. B. Wang, "Grating-assisted demodulation of interferometric optical sensors," *Appl. Opt.* 42, 6824-6829 (2003).
- [62] J. Tian, Q. Zhang, T. Fink, H. Li, W. Peng, and M. Han, "Tuning operating point of extrinsic Fabry-Perot interferometric fiber-optic sensors using microstructured fiber and gas pressure," *Opt. Lett.* 37, 4672-4674 (2012).

## Chapter 2

### Basic principle of FPIs

This chapter describes the basic principle of Fabry-Perot interferometers (FPIs). The interference spectrums of the FPIs with high and low finesse as well as the fringe visibility of the interference spectrum are discussed. Two basic signal demodulation schemes for the FPIs including the spectrum detection based demodulation and the linear demodulation are also introduced. In the last section, the noise source and the noise equivalent pressure level of the FPIs for dynamic pressure measurement are analyzed.

#### 2.1 Interference spectrum of FPIs

##### 2.1.1 High-finesse and low-finesse Fabry-Perot cavities

Fig. 2.1(a) shows the schematic of a Fabry-Perot cavity in which the incident light are reflected forth and back by two reflective mirrors. The multiple lights propagating in the cavity form interference and a typical reflection spectrum of the Fabry-Perot cavity is shown in Fig. 2.1(b). The intensity of the reflected light ( $I_R$ ) from the FPI can be described by [1],

$$I_R = I_0 \frac{R_1 + R_2\eta - 2\sqrt{R_1R_2\eta} \cdot \cos\left(\frac{4\pi nL}{\lambda} + \varphi_0\right)}{1 + R_1R_2\eta - 2\sqrt{R_1R_2\eta} \cdot \cos\left(\frac{4\pi nL}{\lambda} + \varphi_0\right)} \quad (2.1)$$

where,  $I_0$  is the intensity of the light launched into the Fabry-Perot cavity,  $R_1$ ,  $R_2$  are the reflectivities of the two mirrors,  $\eta$  is the transmission coefficient of the light traveling forth and back through the cavity,  $n$  is the refractive index of the cavity,  $L$  is

the cavity length,  $\lambda$  is the wavelength of the light, and  $\varphi_0$  is the constant phase shift.

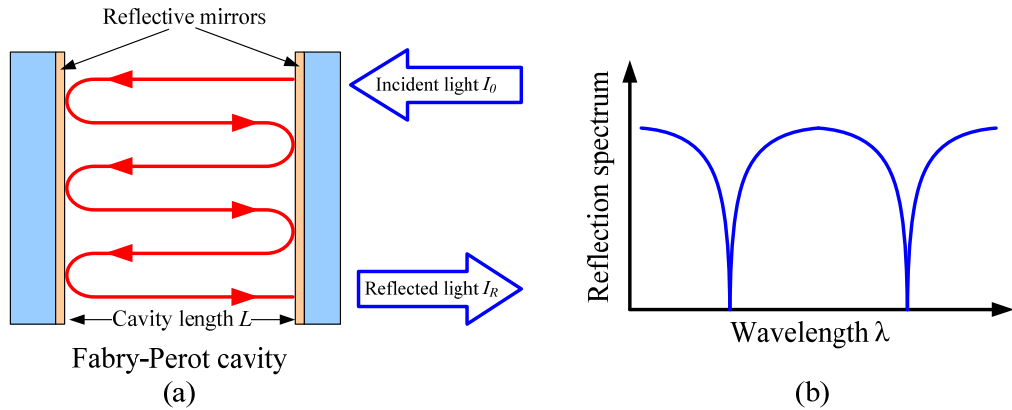


Fig. 2.1 Schematic of (a) a Fabry-Perot cavity and (b) a typical reflection spectrum of the FPI.

Without consideration of the transmission loss of the light in the cavity ( $\eta \approx 1$ ), the reflection spectrums of FPIs with different values of  $R_1$ ,  $R_2$  calculated from Eq. (2.1) are shown in Fig. 2.2.

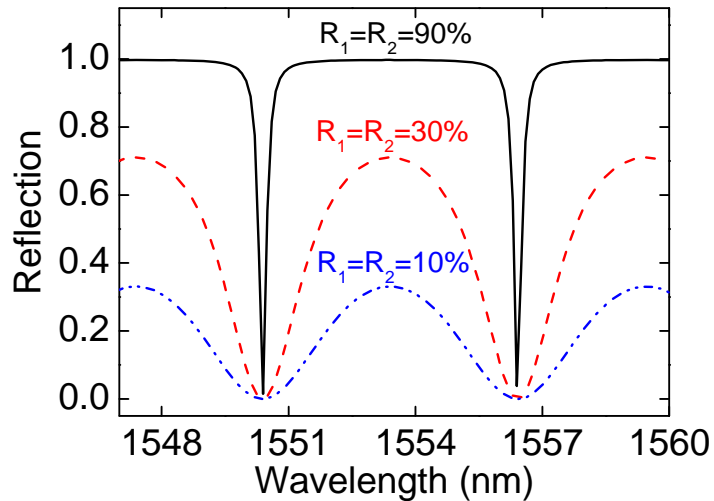


Fig. 2.2 Calculated reflection spectrums of the FPIs with different values of  $R_1$ ,  $R_2$ . In the calculation, the cavity length  $L=200 \mu\text{m}$ , the refractive index of the cavity  $n=1$ , and the transmission coefficient  $\eta=1$ .

The resolution of FPIs can be characterized by the finesse  $F$  defined as [2],

$$F = \pi(R_1 R_2)^{1/4} / (1 - \sqrt{R_1 R_2}) \quad (2.2)$$

For the FPIs with mirrors of equal reflectivities ( $R_1 = R_2 = R$ ), the expression can be simplified as,

$$F = \pi\sqrt{R}/(1 - R) \quad (2.3)$$

From Eq. (2.3), an increase of the reflectivity  $R$  leads to a larger finesse  $F$ , which corresponds to a steeper slope of the interference fringes in Fig. 2.2. For example, if the reflectivity  $R$  increases from 10% to 90%, the finesse  $F$  increases from 1.1 to 29.8.

For FPIs with low-reflectivity mirrors, high-order reflections of the light in the cavity are negligible, as shown in Fig. 2.3. The interference spectrum of the FPI can then be simply described by the two-wave interference approximation.

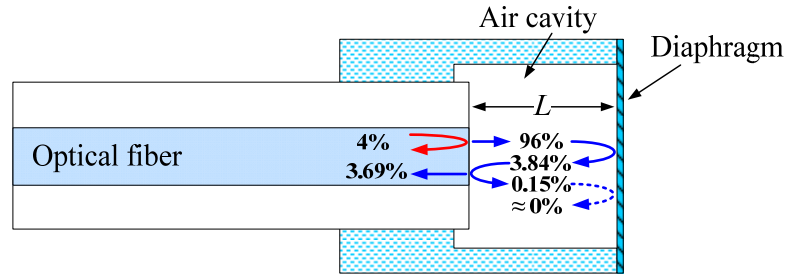


Fig. 2.3 Schematic of the FPI with the silica diaphragm.  $L$  is the air-cavity length of the FPI.

For  $R \ll 1$ , the two-wave interference approximation can be derived from the simplified Eq. (2.1) and can be expressed as,

$$\begin{aligned} I_R &\approx I_0 \left[ R_1 + R_2\eta - 2\sqrt{R_1R_2\eta} \cdot \cos\left(\frac{4\pi nL}{\lambda} + \varphi_0\right) \right] \\ &\propto I_0 \left[ 1 - \gamma \cos\left(\frac{4\pi nL}{\lambda} + \varphi_0\right) \right] \end{aligned} \quad (2.4)$$

The FPI exhibits a reflection spectrum approximating a sinusoidal curve and may be called a low-finesse FPI.  $\gamma$  is the fringe visibility of the interference and can be expressed as,

$$\gamma = \frac{2\alpha\sqrt{R_1R_2\eta}}{R_1 + R_2\eta} \quad (2.5)$$

which depends on the source coherence  $\alpha$ , the intensity ratio of the two reflected lights and the transmission coefficient  $\eta$ . These three factors are considered respectively as below,

**The source coherence:**

Considering a FPI illuminated by a low-coherence light emitting diode (LED) source, the source intensity can be described by the Gaussian function as [3],

$$I(\lambda) = \frac{I_0}{\sqrt{2\pi}\Delta\lambda} \exp\left[-(\lambda - \lambda_0)^2 / (2\Delta\lambda^2)\right] \quad (2.6)$$

where  $\lambda_0$  is the central wavelength,  $\Delta\lambda = \Delta\lambda_{FWHM}/(8\ln 2)^{1/2}$ ,  $\Delta\lambda_{FWHM}$  is the full width at half maximum of the intensity distribution, and  $I_0$  is the optical intensity at  $\lambda_0$ . The coherence of the source  $\alpha$  can then be given by,

$$\alpha = \exp(-2L/L_c) \quad (2.7)$$

$L_c$  is the coherence length of the source and can be estimated by,

$$L_c \propto \lambda_0^2 / \Delta\lambda \quad (2.8)$$

From Eq. (2.7), if the cavity length  $L$  is larger than the coherent length of the light source  $L_c$ , the fringe visibility decreases substantially.

**The intensity ratio of the reflected lights:**

The intensity ratio of the two reflected lights  $R_1/R_2$  is determined by the reflectivities of the two mirrors. For the diaphragm-based FPI as shown in Fig. 2.3, the reflectivity of the fiber end/cavity interface  $R_1$  and the reflectivity for the cavity/diaphragm interface  $R_2$  can be given by,

$$R_1 = \frac{(n_1 - n_2)^2}{(n_1 + n_2)^2}, R_2 = \frac{(n_2 - n_3)^2}{(n_2 + n_3)^2} \quad (2.9)$$

where,  $n_1$ ,  $n_2$  and  $n_3$  are the refractive index of the fiber, air cavity and diaphragm, respectively. For a silica/air interface, its reflectivity is calculated to be  $\sim 4\%$ .

**The transmission coefficient:**

Under the assumption that the lateral offset and the angular offset are negligible, the transmission coefficient  $\eta$  of the light traveling around the air cavity can be described

by [4],

$$\eta = \frac{4(4Z^2 + w_1^2 / w_2^2)}{(4Z^2 + (w_1^2 + w_2^2 / w_2^2))^2 + 4Z^2 \cdot (w_2^2 / w_1^2)} \quad (2.10)$$

$$Z = \frac{2L}{n_{air} k w_1 w_2} \quad (2.11)$$

where  $w_1$  and  $w_2$  are the field radius (or spot size) of the sending and receiving fibers, respectively. If the field in the step-index single mode fiber (SMF) is approximated by a Gaussian distribution, the spot size  $w$  of the fiber with the core radius of  $a$  can be determined from an analytic approximation given by,

$$\frac{w}{a} \approx 0.65 + \frac{1.619}{V^{3/2}} + \frac{2.879}{V^6} \quad (2.12)$$

where  $V = 2\pi a / \lambda \cdot \sqrt{n_{core}^2 - n_{clad}^2}$  is the normalized frequency of the fiber, and  $n_{core}$  and  $n_{clad}$  are the refractive indices of the fiber core and cladding, respectively. For  $1.2 < V < 2.4$ , the approximation of  $V$  has an accuracy within 1%. Since the incident and reflected lights transmitting in the same fiber for the FPI, we get  $w_1 = w_2$ . Then,  $\eta$  can be simplified as below,

$$\eta = \frac{1}{1 + (\lambda L / \pi n_2 w^2)^2} \quad (2.13)$$

where  $n_2 \approx 1$  is the refractive index of the air cavity. The relationship between the transmission coefficient and the cavity length is shown in Fig. 2.4. For the FPI with a cavity length of 52  $\mu\text{m}$ , the transmission coefficient decreases to 0.5, which corresponds a 3-dB loss for the light transmitting forth and back through the FP cavity once. In the calculation, the parameters used for the SMF are  $a=4.1 \mu\text{m}$ ,  $n_{core}=1.4492$  and  $n_{cladding}=1.444$ .

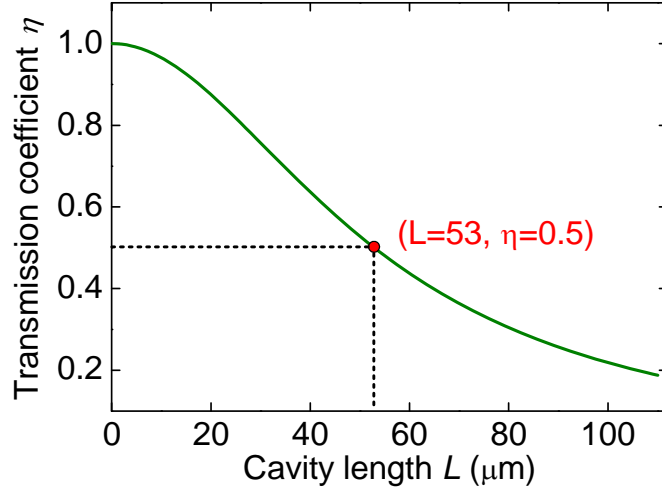


Fig. 2.4 The transmission coefficient  $\eta$  as a function of the cavity length. The source coherence is not considered in the above calculation.

To achieve a maximum fringe visibility  $\gamma$ , the reflectivities of the fiber end and the diaphragm need to satisfy the condition  $R_1 = \eta R_2$ . For FPIs with long cavity lengths, higher values of the reflectivity  $R_2$  are necessary to compensate the loss caused by the decreased transmission coefficient.

## 2.1.2 Interference spectrum considering the diaphragm thickness

In the two-beam interference approximation, the light reflected by the outer surface of the diaphragm is ignored. In the situation that the thickness of the diaphragm is not far smaller than the cavity length of the FPI, the effect of the reflected light from the outer surface of the diaphragm is inappropriate to be ignored and can be described by the three-beam interference approximation as [5],

$$\begin{aligned}
 I \propto |E|^2 &= \left| E_1 - E_2 \cdot \exp\left(j \frac{4\pi}{\lambda} n_{\text{cavity}} L\right) + E_3 \cdot \exp\left[j \frac{4\pi}{\lambda} (n_{\text{diaphragm}} t + n_{\text{cavity}} L)\right] \right|^2 \\
 &= E_1^2 + E_2^2 + E_3^2 - 2E_1 E_2 \cdot \cos\left(\frac{4\pi}{\lambda} n_{\text{cavity}} L\right) - 2E_2 E_3 \cdot \cos\left(\frac{4\pi}{\lambda} n_{\text{diaphragm}} t\right) \\
 &\quad + 2E_1 E_3 \cdot \cos\left[\frac{4\pi}{\lambda} (n_{\text{diaphragm}} t + n_{\text{cavity}} L)\right] \quad (2.14)
 \end{aligned}$$

where,  $E_1$ ,  $E_2$ , and  $E_3$  are respectively the electrical field amplitudes of the three reflected beams,  $L$  is the length of the air cavity,  $t$  is the thickness of the diaphragm,  $\lambda$  is light wavelength, and  $n_{cavity}$  and  $n_{diaphragm}$  are the refractive indices of the cavity and diaphragm, respectively. The negative sign before  $E_2$  is due to the  $\pi$ -phase shift of reflection from the low refractive index dielectric to the high refractive index dielectric at the air/diaphragm interface. The three-beam interference approximation is simple and self-evident to account for the effect of the light reflection from the outer surface of the diaphragm.

To testify the accuracy of this approximation, the more general and accurate  $2 \times 2$  matrix method is adopted to consider the multi-reflections of the lights between the cavity. As shown in Fig. 2.5, considering the lights on both sides of the dielectric as plane waves, the light transmission and reflection can be described by the transition matrix  $T$  and the propagation matrix  $P$ . The transition matrix  $T$  relates the transmitted waves  $A_i$  ( $A_0, A_1, \dots, A_n$ ) and reflected waves  $B_i$  ( $B_0, B_1, \dots, B_n$ ) on both sides of the dielectric interface and the propagation matrix  $P$  accounts for the transmission of the wave in the homogeneous medium.

Take the three-layer structure as shown in Fig. 2.5 for example, the column vector of the plane wave amplitudes ( $A_0, B_0$ ) in the first layer can be related to that ( $A_4, B_4$ ) of the last layer (light launched from left to right) by [1],

$$\begin{bmatrix} A_0 \\ B_0 \end{bmatrix} = T_{01} P_1 T_{12} P_2 T_{23} P_3 T_{34} \begin{bmatrix} A_4 \\ B_4 \end{bmatrix} = \begin{bmatrix} M_{11} & M_{12} \\ M_{21} & M_{22} \end{bmatrix} \begin{bmatrix} A_4 \\ B_4 \end{bmatrix} = M \begin{bmatrix} A_4 \\ B_4 \end{bmatrix} \quad (2.15)$$

$M$  is the  $2 \times 2$  matrix acquired by multiplying the transition and propagation matrix of the multi-layer structures layer by layer.

For a  $N$ -layer structure,

$$M = T_{01} P_1 T_{12} P_2 \dots P_N T_{N,N+1} \quad (2.16)$$

The transmission and reflection coefficients for the multi-layer structure can then be given by,

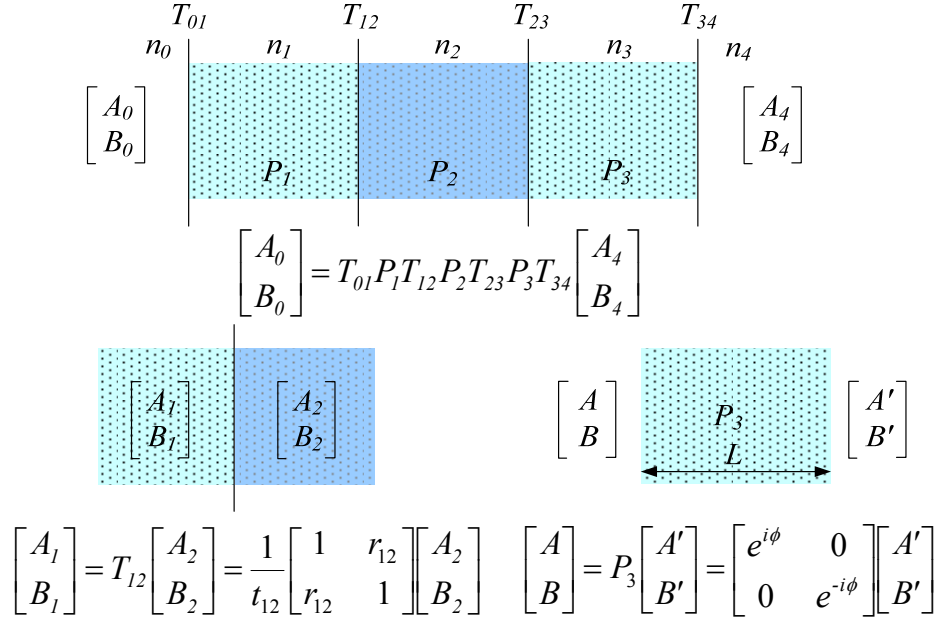


Fig. 2.5 Schematic of the matrix method for calculating the transmission and reflection coefficients of a three-layer structure.

$$t = \left( \frac{A_{N+1}}{A_0} \right)_{B_{N+1}=0} = \frac{1}{M_{11}} \quad (2.17)$$

$$r = \left( \frac{B_0}{A_0} \right)_{B_{N+1}=0} = \frac{M_{21}}{M_{11}} \quad (2.18)$$

$$R = |r|^2, T = tt' = \frac{n_{N+1}}{n_0} |t|^2 \quad (2.19)$$

Fig. 2.6 shows the reflection spectrum of the FPI with a cavity length of 20  $\mu\text{m}$  and a diaphragm thickness of 2  $\mu\text{m}$  calculated by using both the three-beam interference approximation and the  $2 \times 2$  matrix method. The good agreement between the results calculated by these two methods indicates that the three-beam interference approximation is accurate enough for the analysis of low-finesse FPIs. Therefore, the three-beam interference approximation will be adopted to analyze the FPI with a thick diaphragm due to its simplicity.

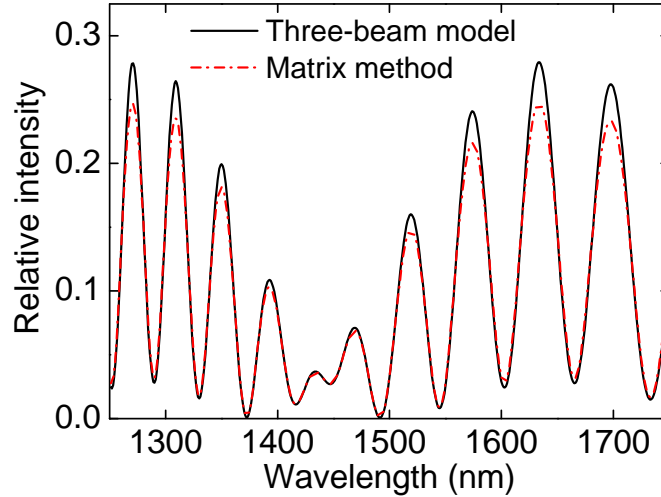


Fig. 2.6 Relative intensity of the reflected light from the low-finesse FPI calculated by the  $2 \times 2$  matrix method and the three-beam interference approximation described by Eq. (2.14), respectively. In the calculation, the cavity length  $L=20 \mu\text{m}$ , the diaphragm thickness  $t=2 \mu\text{m}$ , and the refractive index of the diaphragm and cavity are  $n_{\text{diaphragm}}=1.45$  and  $n_{\text{cavity}}=1$  (air), respectively.

## 2.2 Signal demodulation for FPIs

The spectrum detection based demodulation and the linear demodulation are two widely used methods to demodulate the FPIs. The first one is immune to the intensity variation and has a large measurement range while it has a slow response and is inappropriate for high-speed dynamic measurement (e.g., acoustic signal). In contrast, the second one has a dynamic response with a large bandwidth but a relatively small measurement range.

### 2.2.1 Spectrum detection based demodulation

The configuration for the spectrum detection based demodulation of the FPI is shown in Fig. 2.7. The light launched from a broadband source (BBS) or a tunable laser is delivered to the FPI head through an optical circulator. The reflected light from the FPI passes through the port 3 of the circulator and is detected by an optical spectrum

analyzer (OSA).

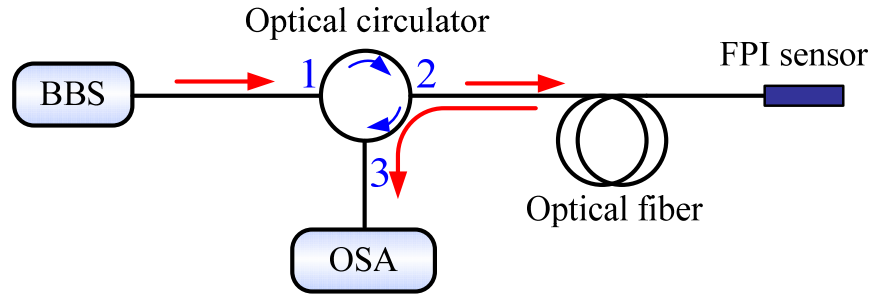


Fig. 2.7 Schematic of the spectrum detection based demodulation of the FPI.

The phase difference  $\Delta\varphi$  of the interference at the peak wavelength satisfies the condition,

$$\Delta\varphi = 4\pi nL / \lambda_m + \phi_0 = 2m\pi, \quad m = 1, 2, 3 \dots \quad (2.20)$$

where  $m$  is the interference order and  $\lambda_m$  is the peak wavelength. The cavity length change of the FPI can be calculated from the peak/valley wavelength change by the relationship,

$$\delta L / L \approx \delta\lambda_m / \lambda_m \quad (2.21)$$

where  $\delta L$  is the cavity length change and  $\delta\lambda_m$  is the shift of the peak wavelength as shown in Fig. 2.8.

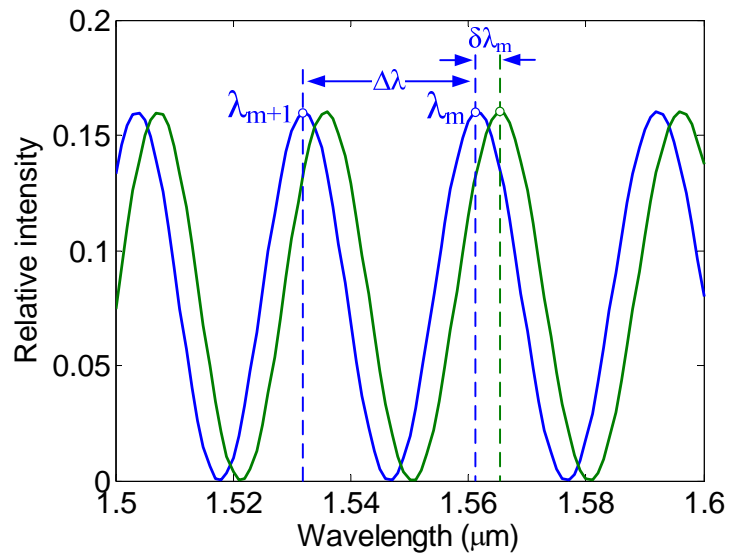


Fig. 2.8 Typical interference spectrum of the FPI.

Due to the sinusoidal nature of the interference signal, the adjacent peaks cannot be distinguished when the interference spectrum shifts over one period of the interference fringe. This ambiguity problem limits the measurement range of this single peak wavelength tracking method. The problem can be solved by direct demodulation of the cavity length change of the FPI. The peak wavelength of the interference spectrum (Fig. 2.8) satisfies the conditions as below,

$$\begin{aligned} 2nL &= m\lambda_m \\ 2nL &= (m+1)\lambda_{m+1} \end{aligned} \quad (2.22)$$

where  $\lambda_m$  and  $\lambda_{m+1}$  are the wavelengths of the adjacent peaks. The cavity length can be estimated by,

$$L = \frac{\lambda_m \cdot \lambda_{m+1}}{2n(\lambda_m - \lambda_{m+1})} \quad (2.23)$$

If the wavelength spacing between the adjacent peaks satisfy the condition,

$$\Delta\lambda = \lambda_m - \lambda_{m+1} \ll \lambda_m, \lambda_{m+1} \quad (2.24)$$

Eq. (2.23) becomes,

$$L \approx \frac{\lambda^2}{2n\Delta\lambda} \quad (2.25)$$

The absolute cavity length can be calculated by monitoring the change of  $\Delta\lambda$  without the information of the interference order  $m$ . The resolution by this multi-peak/valley tracking method is,

$$\frac{\delta L}{L} \approx \frac{\delta\lambda_m}{\Delta\lambda/2} \quad (2.26)$$

which is  $\Delta\lambda/(2\lambda_m)$  times larger than the single peak/valley tracking method. As a result, technique integrating these two methods has been proposed to increase both the dynamic range and the resolution of the FPI [6].

In addition to the above peak/valley tracking methods, curve fitting and Fourier transformation methods have been developed for the demodulation of the FPIs [7].

## 2.2.2 Linear demodulation

For the signal (e. g. acoustic wave) which dynamically modulates the cavity length of the FPI, the linear (or quadrature) demodulation method can be used to demodulate the signal with a high sensitivity and a wide frequency bandwidth [8].

The basic configuration for the quadrature demodulation is similar to that of the spectrum demodulation of the FPI as shown in Fig. 2.7, except that a tunable laser instead of the BBS is used as the optical source, and a photo-detector (PD) connected to an electrical spectrum analyzer (ESA) instead of the OSA is used as the detector. If the cavity length of the FPI is modulated by acoustic waves, the interference spectrum shifts, which changes of the light intensity reflected from the FPI. The light intensity change is then converted to electrical signals by the PD and analyzed by the ESA.

When the operating wavelength works at the quadrature point (Q-point) where the slope of the interference spectrum is maximum, the FPI exhibits a linear response and a maximum sensitivity, as shown in Fig. 2.9 (green line). If the operating wavelength drifts to the peak or dip of the interference spectrum, the sensitivity and the linearity of the FPI deteriorate significantly (blue and red lines). During the detecting process, the working wavelength of the input light should keep at the Q-point to maintain both the high sensitivity and linear response.

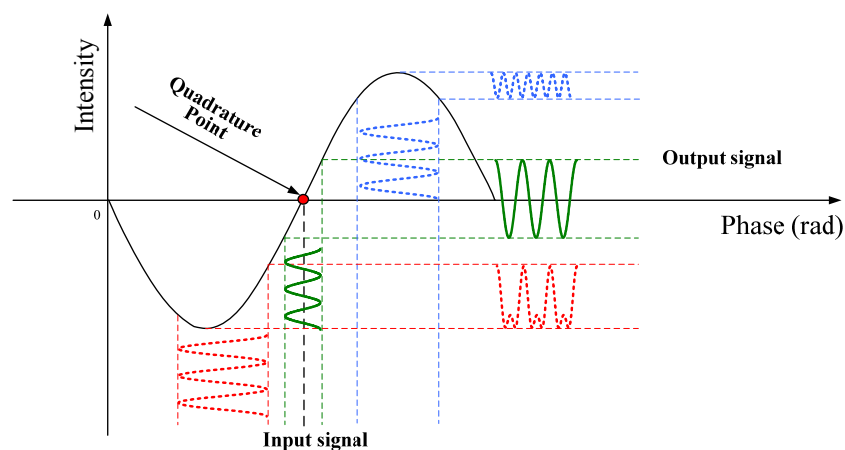


Fig. 2.9 Illustration of the linear demodulation at different operating wavelengths.

For the sake of simplicity, a low-finesse FPI is considered. The interference spectrum of the FPI under the acoustic pressure can be expressed as,

$$I = I_0 \left[ R_1 + R_2 - 2\sqrt{R_1 R_2} \cos(\varphi + \Delta\varphi) \right] \quad (2.27)$$

where  $I_0$  is the light intensity of the laser,  $R_1$  and  $R_2$  are the reflectivities of the two mirrors of the FPI,  $\Delta\varphi$  is the phase change induced by the acoustic wave and  $\varphi = 4\pi nL/\lambda + \varphi_0$  is the phase difference between the two reflected light beams of the FPI. After removing the DC term, the interference spectrum becomes

$$I = 2I_0 \sqrt{R_1 R_2} \cos(\varphi + \Delta\varphi) \quad (2.28)$$

For a sinusoidal acoustic signal with a frequency of  $w_a$ ,  $\Delta\varphi$  can be expressed as,

$$\Delta\varphi = \frac{4\pi n}{\lambda} \cdot x \cdot \sin(w_a t) \quad (2.29)$$

where  $x$  is the pressure induced cavity length change of the FPI.

At the Q point where  $\varphi = \pi/2$ , the output intensity becomes,

$$I = 2I_0 \sqrt{R_1 R_2} \sin\left(\frac{4\pi n}{\lambda} x \sin(w_a t)\right) \approx 2I_0 \sqrt{R_1 R_2} \frac{4\pi n}{\lambda} x \sin(w_a t) \quad (2.30)$$

for  $x \ll \lambda$ . The pressure sensitivity of the FPI  $S_{FP}$ , defined as the ratio of the light intensity change to the cavity length change/diaphragm deflection can be expressed as,

$$S_{FP} = 2I_0 \sqrt{R_1 R_2} \frac{4\pi n}{\lambda} \quad (2.31)$$

and the DC intensity of the reflected light at the Q point is,

$$I_Q = I_0 (R_1 + R_2) \quad (2.32)$$

The reflectivities of the two mirrors,  $R_1$  and  $R_2$ , can be derived from the measured maximum ( $I_{max}$ ) and minimum ( $I_{min}$ ) intensity by the relations as follows,

$$I_{max} = I_0 \left( \sqrt{R_1} + \sqrt{R_2} \right)^2 \quad (2.33)$$

$$I_{min} = I_0 \left( \sqrt{R_1} - \sqrt{R_2} \right)^2 \quad (2.34)$$

For the high-finesse FPI, according to Eq.(2.1), the pressure sensitivity  $S_{FP}$  can be

derived by,

$$S_{FP} = \frac{dI}{dL} = \frac{d \left( I_0 \frac{R_1 + R_2 \eta - 2\sqrt{R_1 R_2 \eta} \cdot \cos\left(\frac{4\pi n L}{\lambda} + \varphi_0\right)}{1 + R_1 R_2 \eta - 2\sqrt{R_1 R_2 \eta} \cdot \cos\left(\frac{4\pi n L}{\lambda} + \varphi_0\right)} \right)}{dL} \quad (2.35)$$

Under the assumption that  $R_1 = R_2 = R$  and  $\eta = 1$ ,  $S_{FP}$  is simplified to,

$$S_{FP} = \frac{4\pi n L}{\lambda} \cdot \frac{dI}{d\varphi} = \frac{4\pi n L}{\lambda} \cdot \frac{d \left( I_0 \frac{4R \sin^2(\varphi/2)}{(1-R)^2 + 4R \sin^2(\varphi/2)} \right)}{d\varphi} \quad (2.36)$$

When  $R \ll 1$ , the sensitivity  $S_{FP}$  at the  $Q$  point can be expressed as,

$$S_{FP} = \frac{4\pi n L}{\lambda} \cdot \frac{d(4I_0 R \sin^2(\varphi/2))}{d\varphi} = \frac{4\pi n L}{\lambda} \cdot 2I_0 R \sin(\varphi) = \frac{4\pi n L}{\lambda} \cdot 2I_0 R \quad (2.37)$$

which is in agreement with the result for the low-finesse FPI.

Fig. 2.10 shows the interference spectrums of the FPIs with different values of  $R_1$  and  $R_2$  with the  $Q$  points indicated by the circle symbols. It is found that the  $Q$  point shifts to the short wavelength with the increase of  $R_1$  and  $R_2$ .

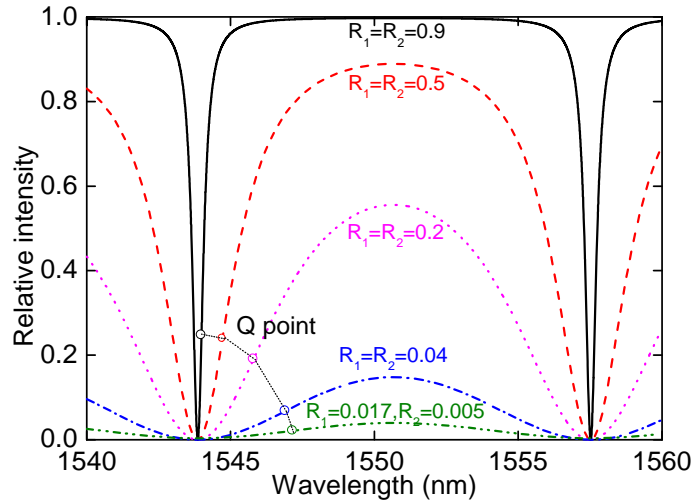


Fig. 2.10 Interference spectrums of FPIs with different values of  $R_1$  and  $R_2$ . The circle symbols denote the  $Q$  points of the interference spectrum.

Table 2.1 lists the slopes of the interference spectrums at the  $Q$  point of FPIs

with different values of  $R_1$  and  $R_2$ . The cavity length used for calculation is 88  $\mu\text{m}$ .

Table 2.1 Slopes of interference spectrums at the Q points for FPIs with different  $R_1$  and  $R_2$ .

$R_1$	$R_2$	Q point wavelength (nm)	$(dI/I_0)/d\lambda$ (/nm)	$(dI/I_0)/dL$ (/nm)
0.9	0.9	1544.0	2.9	50e-3
0.5	0.5	1544.7	0.42	7.3e-3
0.2	0.2	1545.8	0.15	2.6e-3
0.04	0.04	1546.9	0.034	0.61e-3
0.017	0.005	1547.2	0.0083	0.147e-3

Although the quadrature demodulation has a simple configuration and high sensitivity, it suffers from disadvantages such as the fringe direction ambiguity and the sensitivity reduction when the Q-point shifts to the peak/dip of the interference spectrum. In addition, its sensitivity is influenced by the fluctuations of the optical source power or the transmission loss of the light in the fiber. The latter problem has been improved by using a self-calibrated interferometric/intensity based configuration which splits the output of the sensor into two paths with different coherences. The high-coherence path is used for the demodulation of the signal and the low-coherence path is used for the reference to compensate the sensitivity fluctuation caused by the undesirable perturbations. To alleviate the variation of the Q-point, techniques such as dynamical tuning of the working wavelength of the DFB laser or rotating a diffraction grating with a feedback circuit have been developed [9]. However, it is not an easy job to exactly control the working wavelength at the Q-Point. In practice, the operating range of the cavity length change  $\Delta L$  around the Q point is defined as,

$$\Delta L \leq \frac{\lambda}{8} \quad (2.38)$$

in which the output from the sensor exhibits an acceptable sensitivity and linearity.

The change of light intensity from the FPI is usually converted into electrical signals by a PD and an amplifier for readout. For the PD with a responsibility of  $\mathfrak{R}$  and the amplifier with a gain of  $G$ , the output current  $i_{ac}$  of a low-finesse FPI for an laser source with the light intensity of  $I_0$  can be expressed as,

$$i_{ac} = \mathfrak{R} \cdot G \cdot I_0 \cdot S_{FP} \cdot \Delta L = \mathfrak{R} \cdot G \cdot I_0 \cdot 2\sqrt{R_1 R_2} \cdot \frac{4\pi n}{\lambda} \cdot S_d \cdot \Delta P \quad (2.39)$$

where  $S_{FP}$  is defined by Eq. (2.31),  $S_d = \Delta L / \Delta P$  is the pressure sensitivity of the diaphragm, and  $\Delta L$  is the diaphragm deflection induced by the dynamic pressure  $\Delta P$ .

As indicated by Eq. (2.39), the sensitivity of the FPI to the dynamic pressure ( $i_{ac}/\Delta P$ ) depends on not only the pressure sensitivity of the diaphragm  $S_d$  and the finesse of the FP cavity, but also the light source, the PD and the amplifier.

## 2.3 Noise analysis

### 2.3.1 Noise source

In optical interferometers, the noises involved include thermal noise, shot noise, excessive noise from optical source (frequency noise and intensity noise), and electrical noise.

The intrinsic thermal noise is caused by the thermal dynamic fluctuations in the fiber and transducer itself. The intrinsic thermal noise  $\sigma_{th}$  in a fiber with length of  $L$  (in meters) at a frequency of 1 kHz can be approximated as [10],

$$\sigma_{th} = (-147 + 10 \log(L)) \text{ dB re rad / Hz}^{1/2} \quad (2.40)$$

and the thermal noise rolls off at higher frequencies. For a sensor with a fiber length of 10 m, the thermal noise is  $\sim 0.14 \mu\text{rad/Hz}^{1/2}$ .

The shot noise current  $i_{shot}$  is related to the electrical current of the PD and can be given by,

$$i_{shot} = \sqrt{2 \cdot e \cdot (\mathfrak{R} I_{inc}) \cdot \Delta f} \quad (2.41)$$

where  $e$  is the electron charge,  $\mathfrak{R}$  is the responsibility of the PD,  $I_{inc}$  is the optical intensity incident on the PD and  $\Delta f$  is the bandwidth over which the noise is considered.

The frequency noise of the laser induces the phase noise which is proportional to

the optical path difference of the interferometers. The phase noise can be eliminated by matching the paths in the interferometers, even though the path matching is not practical for most applications. Here, the frequency noise is ignored for simplicity.

The intensity noise of the laser represented by the relative intensity noise (RIN), is strongly dependent on the technology of the laser manufacture. In the following noise analysis, a RIN of -150 dB is used for the illustrated purpose.

The electronic noise of the detector is typically in the  $\text{pA/Hz}^{1/2}$  range, which determines the minimum detectable current of the PD.

### 2.3.2 Noise equivalent pressure level

The minimum detectable phase (MDP) for the interferometer with the quadrature demodulation can be described by [10],

$$d\phi_{MDP} = \sqrt{\frac{i_{shot}^2 + i_{RIN}^2 + i_{elec}^2}{(\mathfrak{R}I_{inc})^2}} \quad (2.42)$$

where the shot noise current  $i_{shot}$  is given by Eq. (2.41),  $i_{RIN}$  is the RIN current,  $i_{elec}$  is the electrical noise current,  $\mathfrak{R}$  is the responsibility of the PD and  $I_{inc}$  is the optical power incident on the PD. Fig. 2.11 shows the calculated MDP as a function of  $I_{inc}$ .

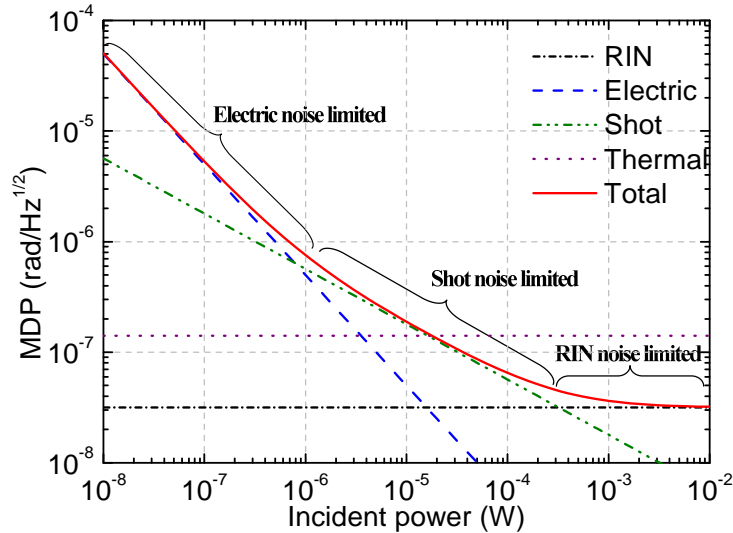


Fig. 2.11 MDP as a function of the optical power incident on the detector  $I_{inc}$ .

The electrical noise in the calculation is assumed to be  $0.5 \text{ pA/Hz}^{1/2}$  and the thermal noise in the plot accounts for the sensor working at 1 kHz with a fiber length of 10 m. For the incident power  $I_{inc}$  below  $1 \text{ }\mu\text{W}$ , the electric noise is the dominant noise. With the increase of the incident power, the electric noise is exceeded by the shot noise and the MDP of the sensor becomes to be limited by the shot noise. When the incident power increases up to  $0.3 \text{ mW}$ , the MDP falls into the RIN noise limited region, with a MDP as low as  $\sim 0.02 \text{ }\mu\text{rad/Hz}^{1/2}$ . However, this low MDP is impossible to achieve and is limited to  $\sim 0.2 \text{ }\mu\text{rad/Hz}^{1/2}$  by the thermal noise when the incident power is over  $20 \text{ }\mu\text{W}$ . As a result, before the MDP reduces to the value limited by the thermal noise, the increase of the incident power of the laser can achieve a smaller MDP, as shown in Fig. 2.11.

For the FPI with the  $Q$ -point demodulation, the shot noise  $i_{FPI\_shot}$  can be expressed as,

$$i_{FPI\_shot} = G \cdot (2 \cdot e \cdot i_Q \cdot \Delta f)^{1/2} \quad (2.43)$$

where  $e$  is the electronic charge,  $G$  is the gain of the amplifier,  $\Delta f$  is the noise-equivalent bandwidth of the receiver.  $i_Q$  is the average current from the PD and is given by,

$$i_Q = \mathfrak{R} \cdot (R_1 + R_2) \cdot I_0 \quad (2.44)$$

where  $\mathfrak{R}$  is the responsibility of the PD,  $R_1$  and  $R_2$  are the reflectivities of the two mirrors of the FPI, and  $I_0$  is the light intensity of the laser. Combined with Eq. (2.39), the noise equivalent pressure (NEP) level limited by the shot noise of the FPI pressure sensor can be derived as,

$$\Delta P_{NEP} = \left( \frac{\lambda}{4\pi n} \frac{1}{S_d} \right) \sqrt{\frac{R_1 + R_2}{2 \cdot R_1 \cdot R_2} \frac{e \cdot \Delta f}{I_0 \cdot \mathfrak{R}}} \quad (2.45)$$

From the above equation, the NEP level of the FPI pressure sensor depends on:

- 1) The reflectivity of the cavity mirrors ( $R_1$  and  $R_2$ ), the incident power of the laser  $I_0$  and the responsibility of the PD  $\mathfrak{R}$ .

2) The pressure sensitivity of the diaphragm  $S_d$  (the ratio of the diaphragm deflection to pressure).

## 2.4 Summary

This chapter has introduced the theoretical background of the FPIs with high-finesse and low-finesse. The fringe contrast of the low-finesse FPI is dependent on the source coherence, mirror reflectivity and cavity length. Effect of the diaphragm thickness on the interference spectrum has been analyzed by using the three-beam interference approximation and the  $2 \times 2$  matrix methods. Two simple demodulation schemes for the interrogation of FPIs are also introduced. Finally, the noise source as well as the NEP level of the diaphragm-based FPIs are discussed and the NEP depends on the pressure sensitivity of the diaphragm, which will be investigated in the next chapter.

## References for Chapter 2

- [1] P. Y. Amnon Yariv, "Photonics: Optical Electronics in Modern Communications," Oxford University Press, USA, 6 edition, Jan 26, 2006.
- [2] M. J. Lawrence, B. Willke, M. E. Husman, E. K. Gustafson, and R. L. Byer, "Dynamic response of a Fabry-Perot interferometer," J. Opt. Soc. Am. B. 16, 523-532 (1999).
- [3] J. Deng, "Development of novel optical fiber interferometric sensors with high sensitivity for acoustic emission detection," PhD Thesis, Virginia Polytechnic Institute and State University (2004).
- [4] D. Marcuse, "Loss analysis of single-mode fiber splices," Bell. Syst. Tech. J. 56, 703-718 (1977).
- [5] Y. Zhu, K. Cooper, G. Pickrell, and A. Wang, "High-temperature fiber-tip pressure sensor," J. Lightwave Technol. 24, 861-869 (2006).
- [6] B. Qi, G. Pickrell, J. Xu, P. Zhang, Y. Duan, W. Peng, Z. Huang, W. Huo, H. Xiao, and R. May, "Novel data processing techniques for dispersive white light interferometer," Opt. Eng. 42, 3165 (2003).
- [7] M. Han, "Theoretical and Experimental Study of Low-Finesse Extrinsic Fabry-Perot Interferometric Fiber Optic Sensors," PhD Thesis, Virginia

- Polytechnic Institute and State University (2006).
- [8] B. Yu, D. W. Kim, J. Deng, H. Xiao, and A. Wang, "Fiber Fabry-Perot sensors for detection of partial discharges in power transformers," *Appl. Opt.* 42, 3241-3250 (2003).
- [9] B. Yu and A. B. Wang, "Grating-assisted demodulation of interferometric optical sensors," *Appl. Opt.* 42, 6824-6829 (2003).
- [10] C. K. Kirkendall and A. Dandridge, "Overview of high performance fibre-optic sensing," *J. Phys. D: Appl. Phys.* 37, R197-R216 (2004).

## Chapter 3

### Silica and graphene diaphragms

This chapter discusses responses of silica and graphene diaphragms to static and dynamic pressures in terms of the pressure sensitivity and the resonant frequency. Linear plate theory and nonlinear membrane theory are used respectively to analyze the pressure responses of the silica and graphene diaphragms. This is followed by an investigation of the optical reflectivity of the graphene. Production and identification of the graphene are also briefly introduced.

#### 3.1 Diaphragm design

For diaphragm-based FPI pressure sensors, the diaphragm acts as the sensing element to pressure differences. The information of the pressure difference is recorded in the form of the mechanical deflection of the diaphragm. Before we discuss the mechanical properties of the diaphragm made of different materials, three major parameters are given to evaluate the performance of the diaphragm on pressure measurements.

**Linearity:** linearity can be defined as “the closeness to which a curve approximates a straight line”. Although a nonlinear relationship between the diaphragm deflection and the pressure might still provide accurate and serviceable measurements, a linear relationship is highly desirable for easy demodulation and data reduction;

**Sensitivity:** sensitivity can be defined as the ratio of the diaphragm deflection to the applied pressure. For a linear pressure-deflection relationship, the pressure

sensitivity of the diaphragm  $S_d$  can be expressed as,

$$S_d = y / P \quad (3.1)$$

For a nonlinear pressure-deflection relationship,

$$S_d = dy / dP \quad (3.2)$$

where  $y$  is the deflection,  $P$  is the applied pressure,  $dy$  and  $dP$  are respectively the differential forms of  $y$  and  $P$ ;

**Hysteresis:** hysteresis makes the ascending and descending curve of the pressure response of the diaphragm not superimposed. Hysteresis depends on the applied pressure on the diaphragm.

To characterize the mechanical response of the circular elastic diaphragm subjected to the pressure load, the behavior of the diaphragm, such as the plate behavior or the membrane behavior, needs to be identified for the selection of appropriate theory.

Generally, plate can sustain both tensile and bending stress and membrane can sustain only tensile stress. In the limit of very small thickness, the plate is tensile stress dominant and behaves like a membrane. Identification of the plate or membrane behavior for a circular diaphragm has been conducted in [1]. Fig. 3.1 shows the three regions which describe the plate behavior, the linear membrane behavior and the nonlinear membrane behavior, respectively. The partition of these regions depends on the load parameter  $\gamma$  and the pre-strain parameter  $\alpha$ , where  $P$  is the pressure,  $a$  is the radius,  $h$  is the thickness,  $\varepsilon_0$  is the prestrain,  $E$  is the Young's modulus and  $\nu$  is the poisson ratio. It need to be mentioned that a decrease of the pressure load and the pre-strain corresponds to an increase of  $\gamma$  and  $\alpha$  since the numerators of the expressions for  $\gamma$  and  $\alpha$  are much smaller than 1 as shown in Fig. 3.1.

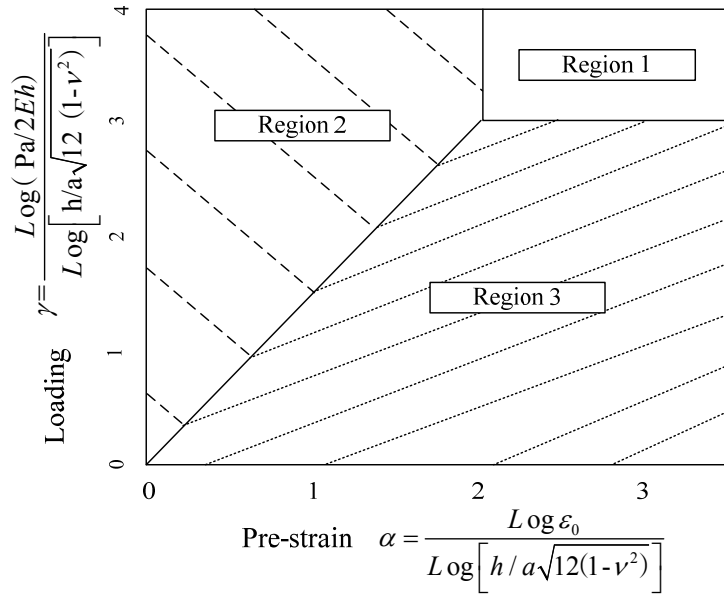


Fig. 3.1 Parameter space delineating regions of the plate behavior, linear membrane behavior, and nonlinear membrane behavior [1].

In the region 1, the pre-strain and load are small and the pressure response of the diaphragm can be described by the plate behavior. The deflection of the diaphragm  $y$  exhibits a linear relationship with the pressure  $P$  as  $y \sim P$ . In the region 2, the diaphragm experiences large pre-strain with the stretching dominant over the bending and its pressure response can be described by the linear membrane behavior. The diaphragm deflection  $y$  also shows a linear relationship with the pressure  $P$  as that in the region 1. In the region 3, in the range of  $\gamma < 3$  and  $\alpha > 2$ , the pre-strain is negligible and the stretching dominates over the bending. The diaphragm can be characterized by the nonlinear membrane behavior and its deflection  $y$  presents a relationship with the pressure  $P$  as  $y \sim P^{1/3}$ .

In the following section, the pressure responses of diaphragms made of silica and graphene are discussed, respectively. For the silica diaphragm with the thickness at the micrometer scale, its pressure response is analyzed by the linear plate theory; for the graphene diaphragm with the thickness at the nanometer scale, a nonlinear membrane theory is employed.

## 3.2 Mechanical properties of the silica diaphragm

Fused silica is a noncrystalline form of silica (the crystalline form is called quartz), and is produced without the addition of other ingredients like traditional glass to lower its melting temperature. The high purity makes the thermal and optical properties of the fused silica superior compared to other types of glass. The fused silica has the advantages such as high working temperature, low thermal expansion coefficient, high thermal shock resistance, good UV transparence and excellent resistance to corrosion.

The mechanical and thermal properties of the silica are listed in Table 3.1 [2].

Table 3.1 Mechanical and thermal properties of silica (at 25 °C).

<i>Property</i>	<i>Symbol</i>	<i>Value</i>	<i>unit</i>
<i>Young's modulus</i>	$E$	$7.3 \times 10^{10}$	$Pa$
<i>Poisson ratio</i>	$\nu$	$0.17$	-
<i>Density</i>	$\rho$	$2.2 \times 10^3$	$Kg/m^3$
<i>Maximum tensile stress</i>	$\sigma_m$	$\sim 1.5 \times 10^9$	$Pa$
<i>Thermal expansion coefficient</i>	$\alpha$	$\sim 5.5 \times 10^{-6}$	$(^\circ C)^{-1}$

### 3.2.1 Response to static pressure

As shown in Fig. 3.2(a), a thin edge-fixed circular plate deflects under the pressure difference between the two sides of the diaphragm. Under the assumption of small deflections (deflections less than 30% of the plate thickness), the out of plane deflection  $d$  of the plate at the radial distance  $r$  to the pressure  $P$  can be expressed as [3],

$$d = \frac{3(1-\nu^2)P}{16Et^3} (R^2 - r^2)^2 \quad (3.3)$$

where  $R$  is the radius

$t$  is the thickness

$\nu$  is the Poisson ratio

$E$  is the Young's modulus of the diaphragm

Since the fiber is aligned with the center of the diaphragm as show in Fig. 3.2(a),

the deflection of the diaphragm at  $r=0$  is of interest. By substituting  $r=0$  into Eq. (3.3), the deflection at the center of the diaphragm can be given by,

$$d_c = \frac{3(1-\nu^2)P}{16Et^3}R^4 \quad (3.4)$$

If we define the pressure sensitivity of the diaphragm  $S$  as the ratio of the diaphragm deflection to the applied pressure, the pressure sensitivity of the plate  $S$  can be expressed as,

$$S = \frac{d_c}{P} = \frac{3(1-\nu^2)}{16Et^3}R^4 \quad (3.5)$$

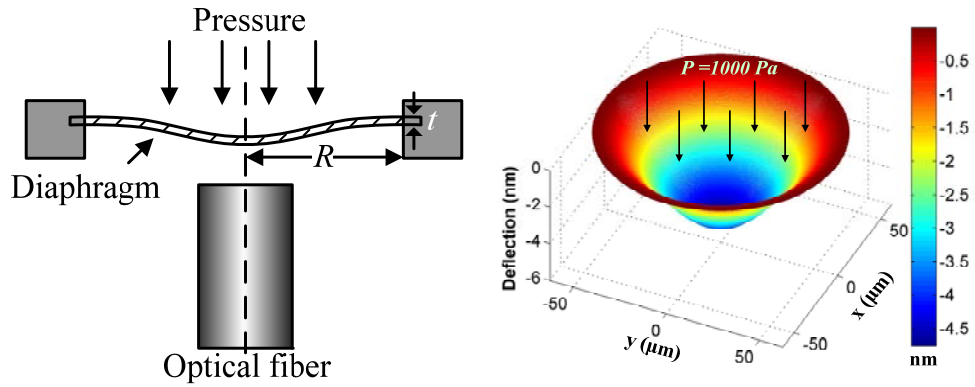


Fig. 3.2 (a) Schematic of a diaphragm based FPI pressure sensor; (b) calculated deflection of a silica diaphragm with a radius of  $62.5 \mu\text{m}$  and a thickness of  $2 \mu\text{m}$  under a pressure of 1 kPa.

Fig. 3.2(b) shows the calculated deflection of the silica diaphragm under a pressure of 1 kPa. The maximum deflection of the diaphragm occurs at the position of  $r=0$ . Based on Eq. (3.5), the pressure sensitivity  $S$  as a function of the radius  $R$  and thickness  $t$  of the plate is plotted in Fig. 3.3.

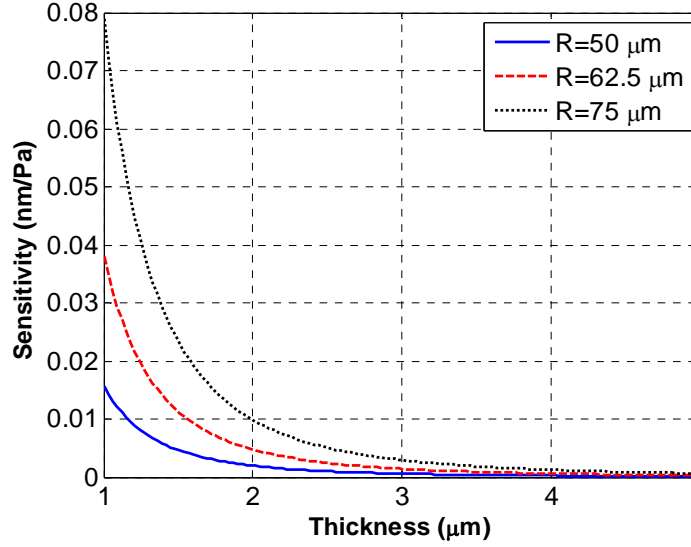


Fig. 3.3 Pressure sensitivity as a function of the thickness for the silica diaphragm with different values of the radius.

The maximum tolerable pressure for the diaphragm can be predicted from the stress in the deflected diaphragm, which can be described by,

$$\sigma_r = \pm \frac{3}{8} P \frac{R^2}{t^2} \left[ (3 + \nu) \frac{r^2}{R^2} - (1 + \nu) \right] \quad (3.6)$$

$$\sigma_t = \pm \frac{3}{8} P \frac{R^2}{t^2} \left[ (1 + 3\nu) \frac{r^2}{R^2} - (1 + \nu) \right] \quad (3.7)$$

where  $\sigma_r$  and  $\sigma_t$  are the radial and tangential stress at the distance of  $r$  from the center of the diaphragm, respectively. The maximum radial stress locates at the edge of the diaphragm and can be given by,

$$\sigma_r = \pm \frac{3}{4} P \frac{R^2}{t^2} \quad (3.8)$$

The maximum tangential stress locates at the center of the diaphragm and can be given by,

$$\sigma_t = \pm \frac{3}{8} (1 + \nu) P \frac{R^2}{t^2} \quad (3.9)$$

In addition to the flat plate, the deflection for a thin semi-spherical shell without

bending effects has been investigated. The deflection  $d$  of the shell center is related to the pressure change  $P$  by [4],

$$d = \frac{(1-\nu)R^2P}{2Et} \quad (3.10)$$

where  $R$  and  $t$  are the radius and the thickness of the spherical shell, respectively. Fig. 3.4 shows the pressure sensitivity  $S$  as functions of the shell thickness  $t$  with different values of the radius  $R$ .

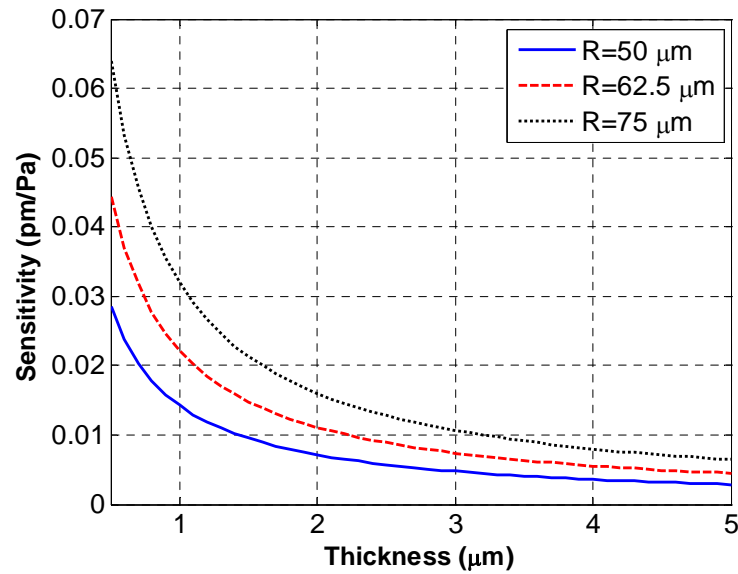


Fig. 3.4 Pressure sensitivity as a function of the thickness of the silica semi-spherical shell with different values of the radius.

Compared to the plate, the spherical shell shows considerably lower pressure sensitivity with the similar diameter and thickness. The dependence of the pressure sensitivity on the physical size for the spherical shell is significantly reduced, from  $R^4/t^3$  to  $R^2/t$ .

### 3.2.2 Response to dynamic pressure

For an edge fixed thin circular plate, the deflection at the center of the plate to the dynamic pressure with a frequency of  $f$  can be described by [5],

$$d(f) = d_c \cdot \sum_{m=0}^{\infty} \sum_{n=0}^{\infty} A_{mn} \cdot \beta_{mn}(f) = \frac{3(1-\nu^2)P}{16Et^3} R^4 \cdot \sum_{m=0}^{\infty} \sum_{n=0}^{\infty} A_{mn} \cdot \beta_{mn}(f) \quad (3.11)$$

where  $d_c$  is the deflection at the center of the plate under the static pressure, and  $(m, n)$  and  $A_{mn}$  are the mode order and the weight constant for each resonant mode, respectively.  $\beta_{mn}(f)$  is the enhancement coefficient for the resonant mode with the order of  $(m, n)$  and is expressed as,

$$\beta_{mn}(f) = \sum_{m=0}^{\infty} \sum_{n=0}^{\infty} \left[ \frac{w_{mn}^2}{\sqrt{(w_{mn}^2 - 4\pi^2 f^2)^2 + 16\pi^2 f^2 \xi^2}} \right] \quad (3.12)$$

where  $\xi = \kappa/2\rho t$  describes the damping effect of the surrounding material (e.g. air or liquid) to the diaphragm, and  $\kappa$  and  $\rho$  are the damping coefficient of the material and the density of the diaphragm, respectively.  $w_{mn}$  is the natural resonant frequency for the resonant mode  $(m, n)$  given by,

$$w_{mn} = \frac{\varphi_{mn}^2}{R^2} \sqrt{\frac{Et^2}{12\rho(1-\nu^2)}} \quad (3.13)$$

where  $\varphi_{mn}$  is the roots of the vibration equation for different mode orders ( $m=0,1,2,3, n=1,2,3$ ). The values of  $\varphi_{mn}$  are listed in Table 3.2.

 Table 3.2 Values of  $\varphi_{mn}$ .

$m \backslash n$	0	1	2	3
0	3.196	4.611	5.906	7.143
1	6.306	7.799	9.917	10.537
2	9.44	10.958	12.402	13.795
3	12.577	14.108	15.579	17.005

If the diaphragm is immersed into the liquid with a mass density of  $\rho'$ , the resonant frequency  $w_{mn}$  in Eq. (3.13) decreases to,

$$w'_{mn} = \frac{1}{\sqrt{1+\xi}} w_{mn} \quad (3.14)$$

$$\xi = 0.6689 \frac{\rho' R}{\rho t} \quad (3.15)$$

Fig. 3.5 shows the calculated frequency response of a silica diaphragm around its fundamental resonant frequency with  $\xi=0$ .

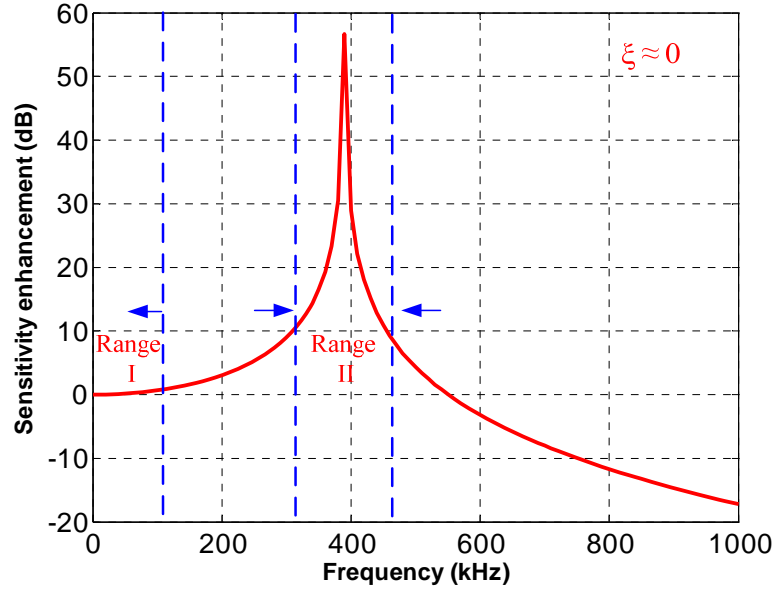


Fig. 3.5 Frequency response of the diaphragm with the radius  $R= 62.5 \mu\text{m}$  and the thickness  $t= 2 \mu\text{m}$ .

To response faithful to the acoustic signal, a flat frequency response is desired for the diaphragm based FPI pressure sensor. This means the fundamental resonant frequency of the diaphragm should be at least (3-5 times) larger than the maximum working frequency in measurements, as indicated by the range *I* in Fig. 3.5. Sensors work in this frequency range can be called the broadband sensors.

When the working frequency approximates the resonant frequency, the response of the diaphragm increases and reaches a maximum value at the resonant frequency (range *II*). The enhancement factor  $\beta_{00}$  of the diaphragm near its fundamental resonant frequency ( $w_{00}$ ) can be expressed as,

$$\beta_{00} \approx \frac{w_{00}^2}{4\pi f \xi} \quad (3.16)$$

Sensors work in the frequency range near the resonant frequency can be called the narrowband sensors. The high sensitivity of this type of sensors may be used for, e.g., photoacoustic gas detection.

## **3.3 Mechanical and optical properties of the graphene diaphragm**

Graphene is a single atomic layer of graphite with the carbon atoms arranged in a two-dimension honeycomb lattice. It is the thinnest and strongest material in the world to date with the single layer thickness of  $\sim 0.335$  nm. Although graphene is not discovered by a mechanical exfoliation method until 2004, it has already shown a cornucopia of new physics such as condensed-matter and low dimensional physics. Its superior features in terms of electron mobility, thermal conductivity and mechanical strength might be used for applications such as electronics and nanoelectromechanical system (NEMS) [6].

### **3.3.1 Methods for the production of the graphene**

Mechanical exfoliation, chemical vapor deposition (CVD) and epitaxial growth from silicon carbide (SiC) substrate are several of the most popular methods to produce the graphene.

#### **3.3.1.1 Mechanical exfoliation**

The graphene, which has a layered structure with strong bond in the layer plane and weak van der Waals interaction between layers, is firstly discovered by the mechanical cleavage of the highly oriented pyrolytic graphite [7]. Firstly, a scotch tape is folded and pulled apart to repeatedly peeling the graphite. Then the tape with a thin layer of graphite is pressed onto a silicon (Si) substrate with a 300 nm-thick oxidized silicon ( $\text{SiO}_2$ ) layer and is rubbed against the silicon substrate gently with a plastic tweezers for several minutes. With the assistance of an optical microscope, single or few layers graphene could be distinguished according to the interference color of the reflected

lights [8]. Fig. 3.6 shows the microscope images of the mechanical exfoliated graphene with different layer numbers [9].

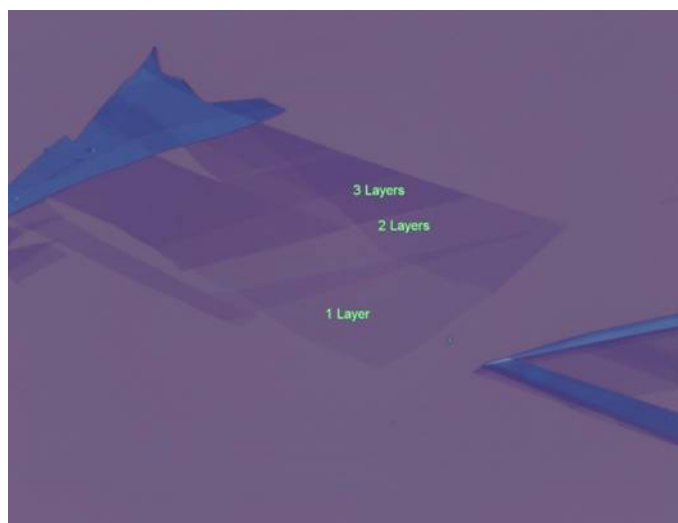


Fig. 3.6 Microscope image of the mechanical exfoliated graphene with different layers on the SiO<sub>2</sub>/Si substrate [9].

Mechanical exfoliation is widely used for the preparation for the pristine graphene film with the best quality compare to other production methods. However, the mechanical exfoliation method is time consuming and the size, thickness and location of the graphene sheets are uncontrollable in practice.

### 3.3.1.2 Chemical vapor deposition

CVD is a comparatively simple method to obtain high-quality single-layer or few-layer graphene film in large quantity. The basic principle of the CVD production of the graphene may be summarized as: the diffusion of the carbon into the metal substrate at the elevated temperature and subsequent precipitation of the carbon from the metal substrate by a cooling process [10]. Fig. 3.7 shows the schematic of the system for the graphene grown by the CVD method.

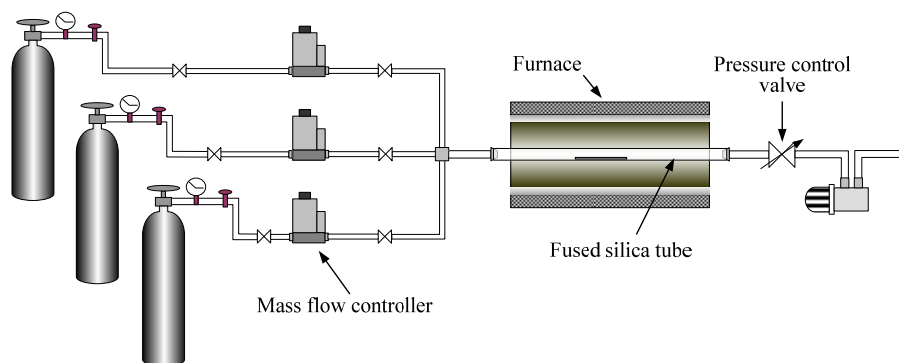


Fig. 3.7 Schematic diagram of a typical system for the graphene grown by the CVD method [11].

Firstly, a metal foil is inserted into a fused silica tube in a hot wall furnace. The tube is evacuated and filled with the hydrogen ( $H_2$ ) and then heated in the temperature of  $\sim 1000$  °C to remove the oxide on the surface of the metal (e.g., Cu). After that, the metal foil is exposed to the  $CH_4$  gas flow. At the temperature of  $\sim 1000$  °C, the carbon decomposed from the  $CH_4$  dissolves into the metal foil. When the tube is cooled down, the graphene dissolving into the metal foil segregates and rearranges into the graphene film due to the reduced dissolution of the carbon in the metal at a lower temperature. Different combinations of the parameters including the growth pressure, working temperature,  $H_2/CH_4$  flow ratio, growth time and cooling rate have been used for the graphene production. In the system, the gas flow is controlled by a mass flow controller with a gas deliver/removal system and the temperature is controlled through the hot wall furnace.

In addition to the CVD method, the epitaxial growth of the graphene on the SiC substrate is another promising technique for the mass production of the graphene. As the silicon has a higher sublimation rate compared to the carbon, when the SiC substrate is heated at temperatures in the range of 1200-1600 °C in vacuum, the remaining carbon rearranges and forms the graphene on the surface of the substrate [12]. The epitaxially grown graphene can be directly used for electronics-related applications, without the need of transferring the graphene from the metal substrate to dielectric substrate as that done for the CVD grown graphene.

### 3.3.2 Characterization of the graphene

Although the graphene is firstly discovered by the micromechanical cleavage of the graphite with an adhesive tape, the same method has been attempted by other groups before or later but only graphite flakes with the thickness of 20-100 layers were found. The problem is that it is impossible to locate the rare amount of the graphene hidden in a stack of thick graphite flakes left on the substrate. Even for the scanning probe microscope which can measure a film with an atomic thickness, the low throughput of the microscope makes it extremely difficult to search the several-micrometer-large graphene on the substrate with a centimeter-scale area. The critical factor for the discovery of the graphene is to observe and identify the graphene in an efficient way. By transferring the exfoliated graphene onto the oxidized silicon wafer with a specific SiO<sub>2</sub> thickness of ~300 nm, the graphene can be identified by its color contrast to the bare Si/SiO<sub>2</sub> substrate under an optical microscope. The observable color contrast results from that the graphene adds sufficient optical path difference to the two reflected beams, one from the Si/SiO<sub>2</sub> interface and the other from the SiO<sub>2</sub>/air interface [8]. The layer number of the graphene can be determined according to the different color contrasts observed by the microscope.

This method is efficient and ideally suitable for the graphene mechanical exfoliated onto the Si/SiO<sub>2</sub> substrate. Its disadvantage is that the color contrast between the graphene and the substrate varied from lab to lab due to the different light source, microscope, and thickness of the SiO<sub>2</sub> layer [13]. As a result, there is no uniform standard practical for identifying the layer number of the graphene. More definite measurement of the thickness of the graphene can be completed by using the atomic force microscope (AFM) or the transmission electronic microscope (TEM).

The AFM is widely used to directly measure the thickness of the graphene, and the measurement range can vary from single up to hundreds of atomic layers.

However, the slow speed of the scanning process makes it very time-consuming for the mass graphene identification. Furthermore, the interaction force between the AFM tip and the test sample causes an offset of  $\sim 0.5$  nm which induces uncertainty of the exact graphene thickness or layer number [14]. TEM can accurately determine the layer number of the graphene by firstly transferring the graphene film onto a lacey grid coated with carbon and then directly counting the layer number from the cross-section of the graphene edges which has folded back [15]. However, this method induces damage to the graphene sample during the test.

Compared to the AFM or TEM, the Raman spectroscopy is an unambiguous and nondestructive method to identify the layer number as well as the quality of graphene. In the Raman spectrum, the *D* band at  $\sim 1350$   $\text{cm}^{-1}$  provides information of defects in the graphene. Larger intensity of *D* band indicates more defects or worse quality of the graphene. The *G* band at  $\sim 1580$   $\text{cm}^{-1}$  originates from the in-plane vibration of  $\text{sp}^2$  carbon atoms and the intensity of the *G* band can be used to determine the layer number of the graphene [14]. The *G'* (or *2D*) band at  $\sim 2700$   $\text{cm}^{-1}$  originates from the two-photon double resonance Raman process and the profile and position of the *G'* band can be analyzed for identifying the layer number of graphene from single layer up to five layers [16]. For the layer number more than 5, the graphene exhibits a similar *G'* band with that of the bulk graphite, which causes the ambiguity for the identification of the layer number. The ratio of *G* and *G'* peak intensity has also been used for the identification of the layer number [15].

The contrast spectroscopy is another fast, non-destructive and easy method to identify the layer number of the graphene up to 10 layers [17]. The contrast spectrum is obtained by comparing the two reflection spectrums from the substrate covered and uncovered by the graphene film. Both of the spectrums are measured under the illumination of a white light source. The layer number of the graphene film can be determined by comparing the measured contrast value from the contrast spectrum to

the standard contrast values.

### 3.3.3 Mechanical properties of the graphene diaphragm

Since the graphene is a single layer of graphite, it is necessary to review the related study on the mechanical properties of graphite, which has been studied in detail very early in 1981 [18]. The stress and strain of the graphite with a hexagonal lattice can be described by the following matrix, with  $x$  and  $y$  standing for the direction of the lattice in-plane.

$$\begin{bmatrix} \varepsilon_x \\ \varepsilon_y \\ \varepsilon_z \\ \varepsilon_{xz} \\ \varepsilon_{yz} \\ \varepsilon_{xy} \end{bmatrix} = S \begin{bmatrix} \sigma_x \\ \sigma_y \\ \sigma_z \\ \sigma_{xz} \\ \sigma_{yz} \\ \sigma_{xy} \end{bmatrix}, \quad S = \begin{bmatrix} S_{11} & S_{12} & S_{13} & 0 & 0 & 0 \\ S_{21} & S_{22} & S_{23} & 0 & 0 & 0 \\ S_{31} & S_{32} & S_{33} & 0 & 0 & 0 \\ 0 & 0 & 0 & S_{44} & 0 & 0 \\ 0 & 0 & 0 & 0 & S_{55} & 0 \\ 0 & 0 & 0 & 0 & 0 & S_{66} \end{bmatrix} \quad (3.17)$$

Where,  $\varepsilon$  is the strain,  $\sigma$  is the stress,  $S$  is the compliance and  $S_{11}=S_{22}$ ,  $S_{12}=S_{21}$ ,  $S_{13}=S_{31}=S_{23}=S_{32}$ ,  $S_{44}=S_{55}$ , and  $S_{66}=(S_{11}-S_{12})/2$ .

By inverse the matrix, there is,

$$\begin{bmatrix} \sigma_x \\ \sigma_y \\ \sigma_z \\ \sigma_{xz} \\ \sigma_{yz} \\ \sigma_{xy} \end{bmatrix} = C \begin{bmatrix} \varepsilon_x \\ \varepsilon_y \\ \varepsilon_z \\ \varepsilon_{xz} \\ \varepsilon_{yz} \\ \varepsilon_{xy} \end{bmatrix}, \quad C = \begin{bmatrix} C_{11} & C_{12} & C_{13} & 0 & 0 & 0 \\ C_{21} & C_{22} & C_{23} & 0 & 0 & 0 \\ C_{31} & C_{32} & C_{33} & 0 & 0 & 0 \\ 0 & 0 & 0 & C_{44} & 0 & 0 \\ 0 & 0 & 0 & 0 & C_{55} & 0 \\ 0 & 0 & 0 & 0 & 0 & C_{66} \end{bmatrix} \quad (3.18)$$

and,

$$S = C^{-1} \quad (3.19)$$

where  $C$  is the elastic modulus, and  $C_{11}=C_{22}$ ,  $C_{12}=C_{21}$ ,  $C_{13}=C_{31}=C_{23}=C_{32}$ ,  $C_{44}=C_{55}$ , and  $C_{66}=(C_{11}-C_{12})/2$ .

Different techniques have been employed to experimentally measure the

compliance  $S$  or the elastic modulus  $C$ . Ultrasonic testing provides the  $C$  and the flexural vibration and static stress-strain test gives  $S$ . Hence, it is necessary to know the relation between the  $S$  and  $C$ . By calculating the inverse matrix of the  $S$ , equations relate the  $C$  and  $S$  can be derived as follows,

$$C_{11} = \frac{S_{11}S_{33} - S_{13}^2}{(S_{11} - S_{12})(S_{11}S_{33} - 2S_{13}^2 + S_{12}S_{33})} \quad (3.20)$$

$$C_{12} = -\frac{S_{12}S_{33} - S_{13}^2}{(S_{11} - S_{12})(S_{11}S_{33} - 2S_{13}^2 + S_{12}S_{33})} \quad (3.21)$$

$$C_{13} = -\frac{S_{13}}{S_{11}S_{33} - 2S_{13}^2 + S_{12}S_{33}} \quad (3.22)$$

$$C_{33} = \frac{S_{11} + S_{12}}{S_{11}S_{33} - 2S_{13}^2 + S_{12}S_{33}} \quad (3.23)$$

$$C_{44} = C_{55} = \frac{1}{S_{44}} \quad (3.24)$$

$$C_{66} = \frac{C_{11} - C_{12}}{2} = \frac{1}{2(S_{11} - S_{12})} \quad (3.25)$$

According to the study of the group at Union Carbide [19], the elastic constants of the graphite were determined by the static test, ultrasonic pulses and sonic resonance methods.

Table 3.3 Values of the elastic modulus and the compliance modulus for graphite.

Elastic modulus $C$ (GPa)		Compliance modulus $S$ (TPa <sup>-1</sup> )	
$C_{11}$	1060 ± 20	$S_{11}$	0.98 ± 0.03
$C_{12}$	180 ± 10	$S_{12}$	-0.16 ± 0.06
$C_{13}$	15 ± 5	$S_{13}$	-0.33 ± 0.08
$C_{33}$	36.5	$S_{33}$	2.3 ± 0.2
$C_{44}$	0.18 – 0.35	$S_{44}$	2860 - 5560

The Young's modulus of the graphite  $E = 1/S_{11} = 1.02 \pm 0.03$  TPa and the Poisson ration along the basal plane of the graphite  $\nu = -S_{12}/S_{11} = 0.16 \pm 0.06$ .

Recently, the mechanical properties of the graphene are investigated by a

nanoindentation and a pressurized blister test of the free-standing graphene membrane [20, 21]. Table 3.4 lists the basic mechanical properties of the graphene.

Table 3.4 Mechanical and thermal properties of graphene.

Property	Symbol	Value	unit
Young's modulus	$E$	$1.0 \times 10^{12}$	Pa
Poisson ratio	$\nu$	0.165	-
Density	$\rho$	$2.2 \times 10^3$	Kg/m <sup>3</sup>
Maximum tensile stress	$\sigma_m$	$\sim 130 \pm 10 \times 10^9$	Pa
Thermal expansion coefficient	$\alpha$	$\sim -8.0 \pm 0.7 \times 10^{-6}$	(°C) <sup>-1</sup>

Compare Table 3.3 with Table 3.4, the elastic constants  $E$  and  $\nu$  remain the same for the graphite with thickness from the bulk to the atomic scale.

### 3.3.3.1 Response to static pressure

The deflection of the graphene under the static pressure can be described in the same way as that in the bulge test conducted in [21, 22]. Considering a thin clamped circular membrane with the radius of  $a$  and the thickness of  $t$  on a well, as shown in Fig. 3.8, the pressure difference  $\Delta p$  applied on the membrane is balanced by the induced biaxial radial stress  $\sigma$  through the equation,

$$\Delta p \cdot \pi R^2 = \sigma \cdot 2\pi R t \quad (3.26)$$

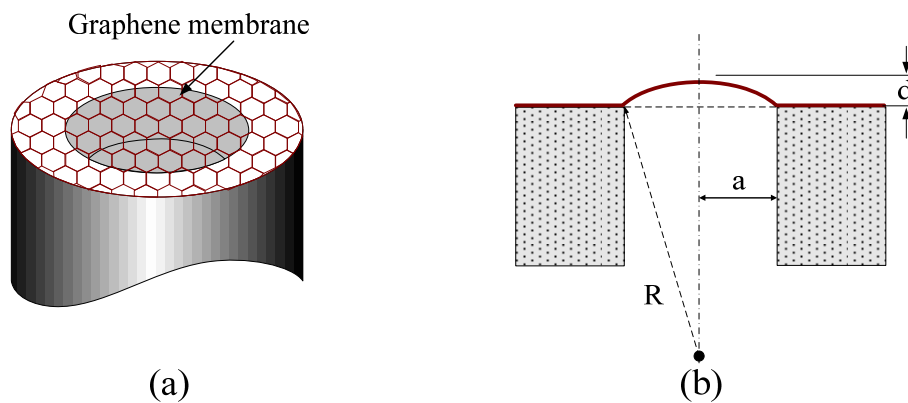


Fig. 3.8 Schematic of (a) the membrane on a well and (b) the cross section of the membrane on the well under a pressure  $\Delta p$ .

The induced biaxial radial stress  $\sigma$  can then be written as,

$$\sigma = \Delta p \cdot R / 2t \quad (3.27)$$

Under the assumption of a small deflection  $d$  ( $d \ll a$ ), the curvature radius of the deflected membrane  $R$  can be expressed as,

$$R \approx a^2 / 2d \quad (3.28)$$

Then the biaxial stress  $\sigma$  can be given by,

$$\sigma = \Delta p \cdot a^2 / 4td \quad (3.29)$$

The corresponding strain  $\varepsilon$  can be calculated from the geometrical deformation of the membrane as,

$$\varepsilon \approx \frac{a^2}{6R^2} \approx \frac{2d^2}{3a^2} \quad (3.30)$$

If the initial stress  $\sigma_0$  (or pre-stress) in the membrane before the pressurization is considered, the total stress  $\sigma$  becomes,

$$\sigma = \frac{E}{(1-\nu)} \varepsilon + \sigma_0 \quad (3.31)$$

By substituting Eq. (3.29) and (3.30) into Eq. (3.31), the deflection of the membrane  $d$  can be expressed as,

$$\Delta p = \frac{E}{(1-\nu)} \frac{8td^3}{3a^4} + \sigma_0 \frac{4td}{a^2} \quad (3.32)$$

In the above derivation, an equal biaxial stress in the membrane is assumed, which requires that the edge of the membrane is tangentially stretched as if there is no constrain on the boundary. This appropriation leads to overestimate of the stress distribution in the membrane induced by the pressure [23]. The discrepancy can be eliminated by introducing the mean strain  $\varepsilon_e$  [22],

$$\varepsilon_e = \frac{3}{4} \varepsilon \quad (3.33)$$

By plugging it into the Eq. (3.31) to replace the biaxial strain  $\varepsilon$ , Eq. (3.32) becomes,

$$\Delta p = \frac{E}{(1-\nu)} \frac{2td^3}{a^4} + \sigma_0 \frac{4td}{a^2} \quad (3.34)$$

The right hand of Eq. (3.34) comprises of a cubic term and a linear term of the deflection, which indicates that the membrane may have a nonlinear response to the pressure. If  $\Delta p$  is large, the first term of Eq. (3.34) dominates, which describes the nonlinear pressure response of the membrane under the large deformation. If  $\Delta p$  is small enough, the second term dominates, which describes the linear pressure response of the stress-dominated membrane. Fig. 3.9 shows the calculated pressure response of membranes with different values of radius. The values for the parameters  $E$  and  $\nu$  used in the calculation are listed in Table 3.4. The membrane with a larger diameter exhibits a higher pressure sensitivity but a smaller linearity range.

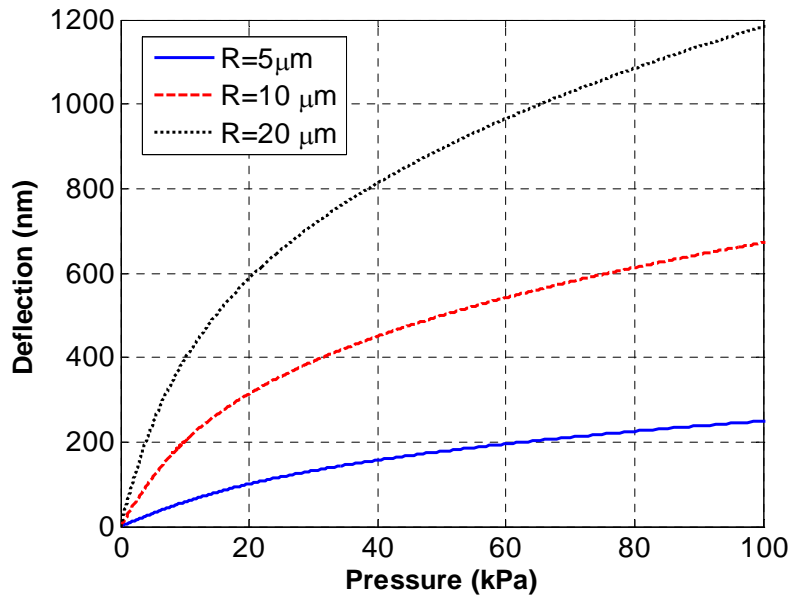


Fig. 3.9 Pressure induced deflections of the membranes with different values of radius. The thickness of the membrane in the calculation is 1 nm and the pre-stress is 1 GPa.

The dependence of the linear working range on the thickness  $t$  and pre-stress  $\sigma_0$  of the membrane is investigated and the pressure responses of membranes with different values of  $t$  and  $\sigma_0$  are calculated and plotted in Fig. 3.10.

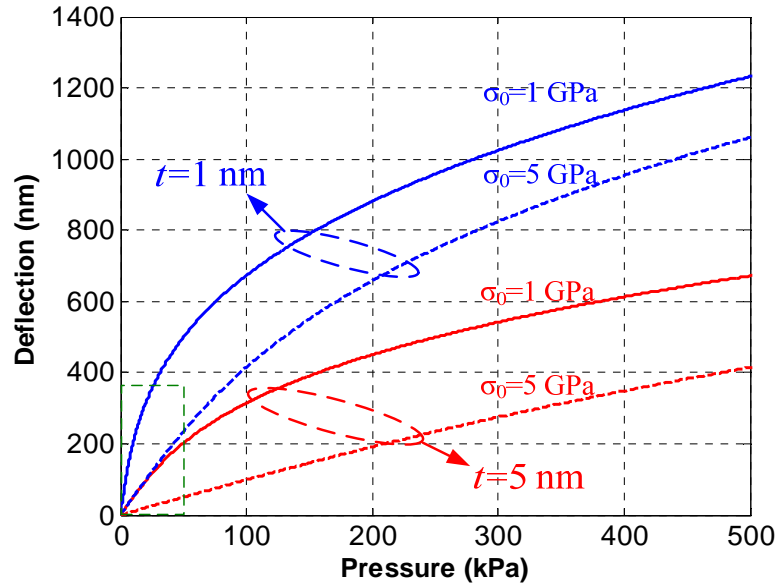


Fig. 3.10 Pressure induced deflections of membranes with different values of thickness and pre-stress. The radius of the membrane in calculation is  $10 \mu\text{m}$ .

The four curves in the area denoted by the dash green line are linearly fitted. The values for the adjusted R-square and slope are listed in Table 3.5.

Table 3.5 Linear working ranges and pressure sensitivities of the graphene films with different values of the thickness and pre-stress.

<i>Thickness (nm)</i>	<i>Pre-stress (GPa)</i>	<i>Adj. R-Square (0-50kPa)</i>	<i>Linear working range for pressure (kPa)</i>	<i>Pressure sensitivity (nm/kPa)</i>
1	1	0.9400	5.2	23.190
5	1	0.9938	25.8	4.638
1	5	0.9994	58	4.634
5	5	1	290	0.927

The linear working range corresponds to an Adj. R-Square value of 0.999. As shown in Table 3.5, when the pre-stress  $\sigma_0$  of the membrane ( $\sigma_0=1\text{GPa}$ ,  $t=1 \text{ nm}$ ) increases for 5 times from 1 GPa and 5 GPa, the linear working range increases by  $\sim 11$  times with the sensitivity decreased by  $\sim 5$  times. Comparatively, when the thickness  $t$  of the membrane increases for 5 times from 1 nm to 5 nm, the linear working range increases by  $\sim 5$  times with the sensitivity also decreased by  $\sim 5$  times.

It can be seen that increasing the pre-stress is a more effective way to enlarge the linear working range with less sacrifice of the pressure sensitivity. In addition, a compromise between the large linear working range and the high pressure sensitivity is necessary to be considered for the design of the pressure sensors with ultra-thin membranes.

### 3.3.3.2 Response to dynamic pressure

Under the assumption that the membrane is a perfectly flexible thin lamina with an uniform thickness and is stretched by a tension large enough to neglect the fluctuation induced by the small deflection during the vibration, the resonant frequency  $f_{mn}$  for a circular membrane with a radius of  $a$  and a thickness of  $t$  can be expressed as [5],

$$f_{mn} = \frac{\alpha_{mn}}{2\pi a} \sqrt{\frac{S}{\rho t}} \quad (3.35)$$

where  $\alpha_{mn}$  is a constant,  $\rho$  is the mass density and  $S$  is the uniform tension per unit length of the boundary.

The resonant frequency for a rectangular membrane with the length  $a$ , width  $b$  and thickness  $t$  is given by,

$$f_{mn} = \frac{1}{2} \sqrt{\frac{S}{\rho t} \left( \frac{m^2}{a^2} + \frac{n^2}{b^2} \right)} \quad (3.36)$$

Fig. 3.11 shows the calculated vibration modes with different mode order  $(m, n)$  for a circular membrane.

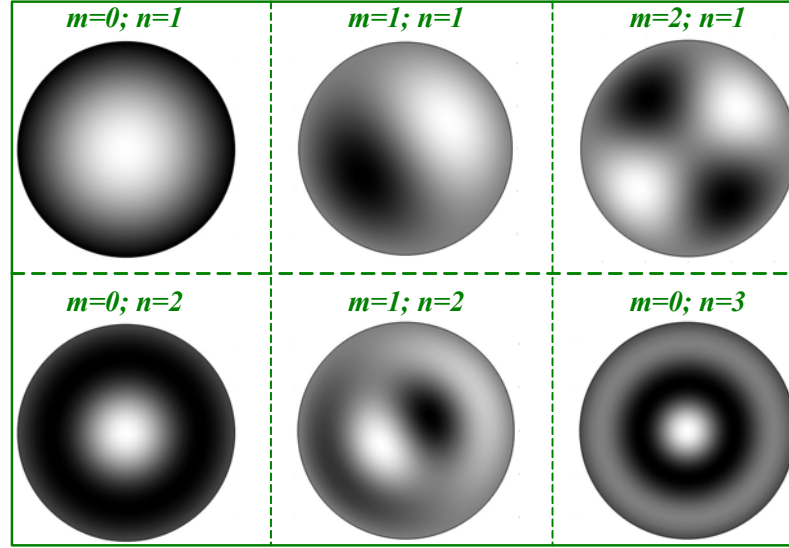


Fig. 3.11 Sketch of the calculated vibration modes with different mode order ( $m, n$ ) for a circular membrane.

The values of the constant  $\alpha_{mn}$  for the vibration modes with different order ( $m, n$ ) of a circular membrane are listed in Table 3.6. The subscript  $m$  and  $n$  denote the number of the nodal diameter and nodal circle, respectively.

Table 3.6 Values of  $\alpha_{mn}$  for the vibration modes.

$m \backslash n$	1	2	3	4	5	6
0	2.404	5.520	8.654	11.792	14.931	18.071
1	3.832	7.016	10.173	13.323	16.470	19.616
2	5.135	8.417	11.620	14.796	17.960	21.117
3	6.379	9.760	13.017	16.224	19.410	22.583
4	7.586	11.064	14.373	17.616	20.827	24.018

If the tension  $S$  is replaced by the stress  $\sigma$  with  $S=\sigma t$ , the resonant frequency  $f_{mn}$  can be expressed as,

$$f_{mn} = \frac{\alpha_{mn}}{2\pi a} \sqrt{\frac{S}{\rho t}} = \frac{\alpha_{mn}}{2\pi a} \sqrt{\frac{\sigma}{\rho}} \quad (3.37)$$

By substituting Eq. (3.29) and Eq.(3.34) into above equation and neglecting the pre-stress, the third power of the frequency  $f^3$  changes linearly with the pressure  $\Delta p$  as,

$$f_{mn}^3 \approx \left( \frac{\alpha_{mn}}{2\pi a} \right)^3 \sqrt{\frac{2Ea^2}{64(1-\nu)t^2\rho^3}} \Delta p \quad (3.38)$$

Fig. 3.12 shows the calculated resonant frequency for the fundamental vibration mode ( $m=0, n=1$ ) of the membrane under different pressures. In the calculation, Eq. (3.37) is used to consider the pre-stress  $\sigma_0$ .

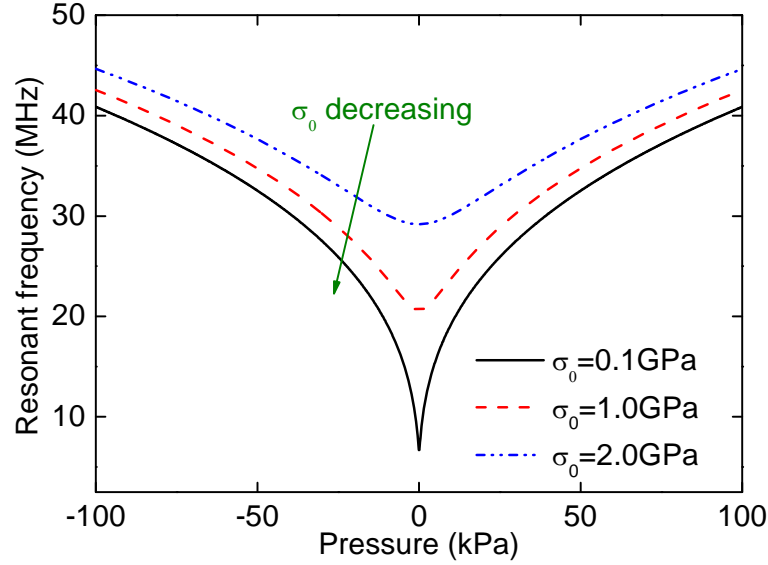


Fig. 3.12 Resonant frequency as functions of the pressure for membranes with different pre-stress  $\sigma_0$ .

### 3.3.3.3 Air effects on the resonant frequency

In the previous section, the membrane is assumed to vibrate freely without being affected by the air. This assumption is valid only if the membrane is placed into a vacuum environment or the radius to thickness ratio of the membrane is relatively small according to Eq. (3.15). When a thin circular membrane vibrates in fluids (the air in our case), the fluid moves in phase with the vibrating membrane and its inertia behaves as an added virtual mass to the membrane. This added virtual mass effect (or acoustic radiation effect) on the resonant frequency of the membrane should be considered and might be described in a similar way to that for the plate as [24],

$$f = \frac{1}{\sqrt{1+\xi}} f_0 \quad (3.39)$$

$$\xi = \frac{\rho_f}{\rho} \cdot \frac{a}{t} \cdot \Gamma \quad (3.40)$$

with,  $f_0$ : the initial resonant frequency of the membrane

$f$ : the resonant frequency considering the added virtual mass effect

$\xi$ : the added virtual mass incremental (AVMI) factor

$\rho_f$ : the mass density of the fluid

$\rho$ : the mass density of the membrane

$a$ : the radius of the membrane

$t$ : the thickness of the membrane

$\Gamma$ : the non-dimensional AVMI factor

The non-dimensional AVMI factor  $\Gamma$  for an edge clamped circular membrane is 0.7463 for the fundamental vibration mode ( $m=0, n=1$ ) [24].

The resonant frequency of the membrane can be thus related to the air pressure by replacing the fluid density  $\rho_f$  with the air density  $\rho_a$  by [25],

$$\rho_a = 1.18 \times 10^{-5} P / P_0 \text{ (kg / m}^3\text{)} \quad (3.41)$$

where  $P$  is the pressure of the air and  $P_0$  is the reference pressure equal to 1 Pa. The relative resonant frequency shift as functions of the pressure for membranes with different thickness is plotted in Fig. 3.13. With the decrease of the membrane thickness, the acoustic radiation exerts more significant effects on the resonant frequency of the membrane.

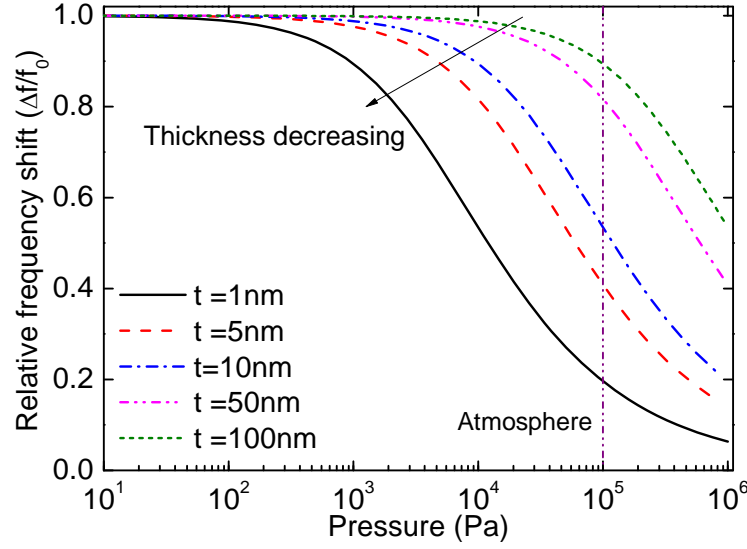


Fig. 3.13 Relative frequency shift as functions of the pressure for membranes with different values of thickness.

In the above analysis, the viscous damping effect of air on the resonant frequency has not been considered. For a fluid with a small viscosity ( $\leq 5$  cP), the viscous damping exhibits negligible effects on the resonant frequency of the membrane and might be ignored [26, 27].

### 3.3.4 Optical reflectivity of the graphene diaphragm

For the graphene diaphragm with the thickness at the nanometer scale, its reflectivity shows strong dependence on its thickness (or the layer number). For the light normally incident onto the graphene film, the reflection coefficient and transmission coefficient can be given by [28],

$$r_{02} = r_{01} + \frac{t_{01}t_{10}r_{12}e^{-2i\phi}}{1 - r_{10}r_{12}e^{-2i\phi}} \quad (3.42)$$

$$t_{02} = \frac{t_{01}t_{12}e^{-i\phi}}{1 - r_{10}r_{12}e^{-2i\phi}} \quad (3.43)$$

where  $\phi = 2\pi n_g d / \lambda$ ,  $r_{ab} = (n_a - n_b) / (n_a + n_b)$ ,  $t_{ab} = 2n_a / (n_a + n_b)$  ( $a, b=0, 1, 2$ , stand for the air, graphene and air), and  $n_g$  is the refractive index of the graphene. The

intensity reflectivity coefficient  $R$  and transmission coefficient  $T$  can then be calculated by,

$$R = |r_{02}|^2 \quad T = \frac{n_2}{n_0} |t_{02}|^2 \quad (3.44)$$

For the lossless material,  $R+T=I$  is satisfied. For the graphene, the absorption indicated by the complex refractive index of the graphene can be calculated by the energy conservation:  $A=I-R-T$ ;

Before the calculation of the reflectivity, it is needed to know the refractive index of the graphene. Table 3.7 lists the refractive indices of the graphene obtained theoretically and experimentally by different research groups [28]. However, the results vary from each other and only cover the visible wavelength range (~550 nm).

Table 3.7 Measured and calculated refractive indices for graphene and graphite.

<b>Material</b>	<b>Method</b>	<b>Refractive index</b>
<i>Graphite</i>	<i>Optical reflection</i>	$2.675 - 1.35i$
<i>Graphite</i>	<i>Ellipsometry</i>	$2.52 - 1.94i$
<i>Graphene</i>	<i>Reflection contrast</i>	$2.0 - 1.1i$
<i>Graphene</i>	<i>Reflectance and transmittance</i>	$3.0 - 1.0i$
<i>Graphene</i>	<i>Theory, universal conductance</i>	$1.88 - 1.59i$
<i>Graphene Theory</i>	<i>fit from 10 layers</i>	$2.62 - 0.89i$
	<i>fit from 35 layers</i>	$2.92 - 0.77i$

Fig. 3.14 plots the reflectivity of the graphene with different refractive indices as a function of the layer number at the wavelength of 550 nm. Although the calculated curves are different from each other, they show similar trends and can provide a sketch of the reflectivity range for the graphene film with different layer numbers. As this thesis focuses on the CVD grown graphene with the working wavelength near 1550 nm, in the following calculation, the refractive index value  $n_g=3.45-2.32i$  is used for the CVD grown graphene [29]. The refractive index of the graphene film at the wavelength of 550 nm ( $n_g=2.68-1.36i$ ) reported by the same author is near to the mean value of all the refractive indices in Fig. 3.14, which might prove the validity

of using  $n_g=3.45-2.32i$  at 1550 nm for the following calculation.

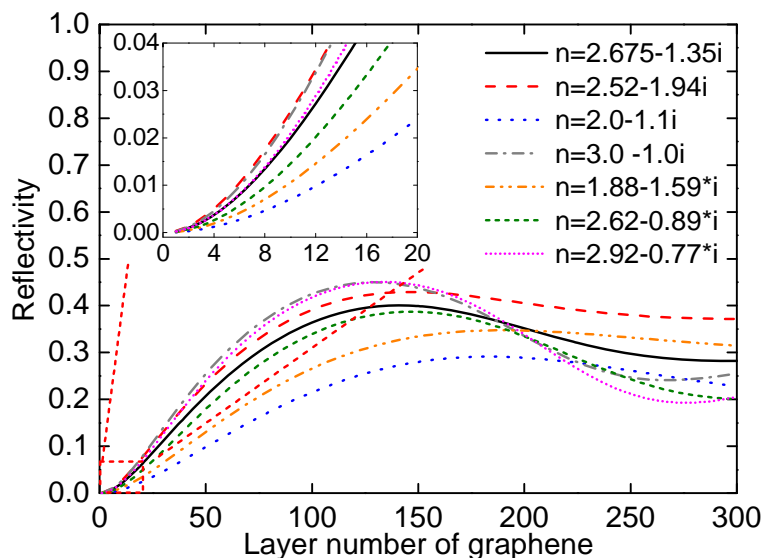


Fig. 3.14 Reflectivity as functions of the graphene layer number for the graphene with refractive indices listed in Table 3.7.

The reflectivity, transmission and absorption coefficient of the graphene film as functions of the layer number at 1550 nm are calculated and plotted in Fig. 3.15. The reflectivity for the graphene film with a few layers is less than  $\sim 0.5\%$ , which is much lower than that ( $\sim 3.5\%$ ) of the well cleaved fiber end.

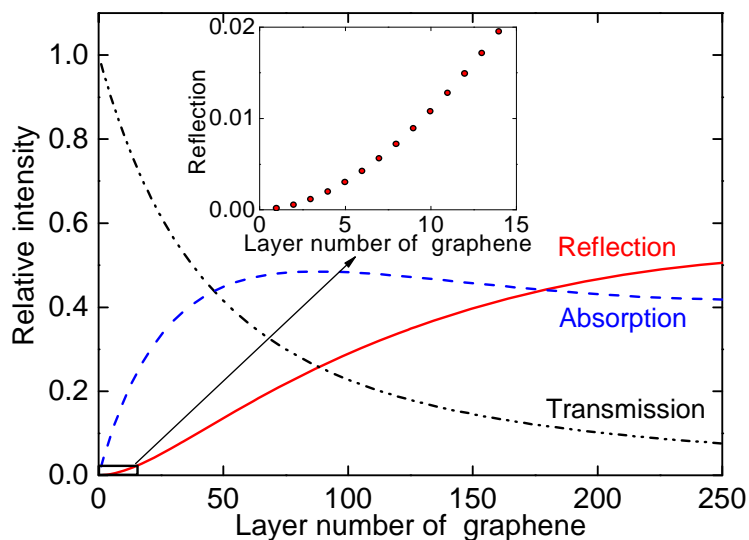


Fig. 3.15 Calculated transmission, reflection and absorption coefficient as functions of the layer number of the graphene film; inset: the reflectivity for the graphene film with the layer number from 1 to 15.

To improve the fringe contrast of the graphene film based FPI, metal coating is one possible method. The reflectivity of the single layer graphene after being coated with the gold (Au) film is plotted in Fig. 3.16. For the Au film with the thickness of  $\sim 2$  nm, the reflectivity can be increased to  $\sim 6\%$ . However, possibilities such as the poor adhesion between the metal film and the graphene or the stress induced in the graphene during the deposition of the metal film might significantly influence the mechanical performance of the nanometer-scale graphene film [30].

Another alternative is to decrease the reflectivity of the fiber end by cleaving the fiber with a specific tilted angle. This method will be described in the fabrication process of the few-layer graphene based fiber-tip FPI in Chapter 5.

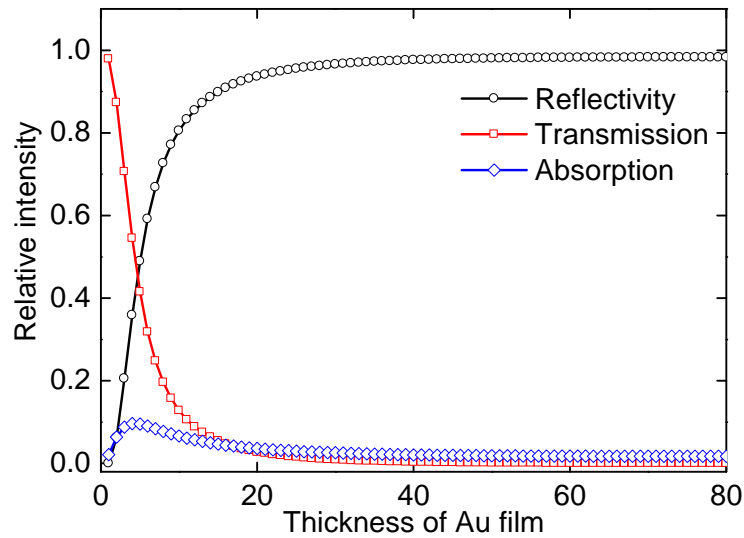


Fig. 3.16 Calculated transmission, reflection and absorption coefficient as functions of the thickness of the Au film. The refractive index of Au used is  $0.55-11.5i$  [31].

### 3.4 Summary

In this chapter, the responses of the silica and graphene diaphragms subjected to the static and dynamic pressures are analyzed. The pressure sensitivity and resonant frequency are primarily determined by the diameter and the thickness of the diaphragm. For the ultra-thin graphene diaphragm, its pressure sensitivity and

resonant frequency are also dependent on the pre-stress. In the last part, the optical reflectivity of the graphene is calculated by treating the graphene as a thin film with stacked layers. The calculated reflectivity for the graphene with the layer number less than 10 is lower than 1% and shows a rapid increase with the layer number.

## References for Chapter 3

- [1] U. Komaragiri, M. R. Begley, and J. G. Simmonds, "The mechanical response of freestanding circular elastic films under point and pressure loads," *Trans. ASME, J. Appl. Mech.* 72, 203-212 (2005).
- [2] J. Xu, "High temperature high bandwidth fiber optic pressure sensors," PhD Thesis, Virginia Polytechnic Institute and State University (2005).
- [3] A. C. Ugural, *Stresses in Beams, Plates, and Shells*, Third Edition, Computational Mechanics and Applied Analysis, CRC Press, Jul, (2011).
- [4] Y. W. C. Roark. R. J., "Formulas for Stress and Strain," New York: McGrawHill. (1989).
- [5] J. W. Weaver, S. P. Timoshenko, and D. H. Young, *Vibration Problems in Engineering*, 5th Edition, Wolfenden Press, Mar, (2007).
- [6] A. K. Geim and K. S. Novoselov, "The rise of graphene," *Nat. Mater.* 6, 183-191 (2007).
- [7] K. S. Novoselov, A. K. Geim, S. V. Morozov, D. Jiang, Y. Zhang, S. V. Dubonos, I. V. Grigorieva, and A. A. Firsov, "Electric field effect in atomically thin carbon films," *Science* 306, 666 (2004).
- [8] K. S. Novoselov, D. Jiang, F. Schedin, T. J. Booth, V. V. Khotkevich, S. V. Morozov, and A. K. Geim, "Two-dimensional atomic crystals," *Proc. Natl Acad. Sci. USA.* 102, 10451-10453 (2005).
- [9] "Carbon flatland, Summer Science Exhibition 2011," The Royal Society. Website: <http://royalsociety.org/summer-science/2011/carbon-flatland>, July.
- [10] C. Mattevi, H. Kim, and M. Chhowalla, "A review of chemical vapour deposition of graphene on copper," *M. J. Mater. Chem.* 21, 3324-3334 (2011).
- [11] C. Miao, C. Zheng, O. Liang and Y.-H. Xie, *Physics and Applications of Graphene-Experiments: Chapter 3 Chemical Vapor Deposition of Graphene*, (2011).
- [12] S. Shivaraman, R. A. Barton, X. Yu, J. Alden, L. Herman, M. Chandrashekar, J. Park, P. L. McEuen, J. M. Parpia, and H. G. Craighead, and M. G. Spencer, "Free-standing epitaxial graphene," *Nano Lett.* 9, 3100-3105 (2009).
- [13] P. Blake, E. W. Hill, A. H. Castro Neto, K. S. Novoselov, D. Jiang, R. Yang, T. J. Booth, and A. K. Geim, "Making graphene visible," *Appl. Phys. Lett.* 91, 063124 (2007).
- [14] Z. Ni, Y. Wang, T. Yu, and Z. Shen, "Raman Spectroscopy and Imaging of

- Graphene,” *Nano Res.* 1, 273-291 (2008).
- [15] A. Reina, X. Jia, J. Ho, D. Nezich, H. Son, V. Bulovic, M. S. Dresselhaus, and J. Kong, “Large area, few-layer graphene films on arbitrary substrates by chemical vapor deposition,” *Nano Lett.* 9, 30-35 (2009).
- [16] A. C. Ferrari, J. C. Meyer, V. Scardaci, C. Casiraghi, M. Lazzeri, F. Mauri, S. Piscanec, D. Jiang, K. S. Novoselov, S. Roth, and A. K. Geim, “Raman spectrum of graphene and graphene layers,” *Phys. Rev. Lett.* 97, 187401 (2006).
- [17] Z. H. Ni, H. M. Wang, J. Kasim, H. M. Fan, T. Yu, Y. H. Wu, Y. P. Feng, and Z. X. Shen, “Graphene thickness determination using reflection and contrast spectroscopy,” *Nano Lett.* 7, 2758-2763 (2007).
- [18] B. T. Kelly, “Physics of Graphite,” Applied Science Publishers, 1981.
- [19] O. L. Blakslee, D. G. Proctor, E. J. Selden, G. B. Spence, and T. Weng, “Elastic Constants of Compression-Annealed Pyrolytic Graphite,” *J. Appl. Phys.* 41, 8 (1970).
- [20] C. Lee, X. Wei, J. W. Kysar, and J. Hone, “Measurement of the elastic properties and intrinsic strength of monolayer graphene,” *Science* 321, 385-388 (2008).
- [21] J. S. Bunch, Mechanical and electrical properties of graphene sheets, PhD Thesis, Cornell University, 2008.
- [22] D. Xu and K. M. Liechti, “Bulge Testing Transparent Thin Films with Moiré Deflectometry,” *Exp. Mech.* 50, 217-225 (2010).
- [23] K.-T. Wan and Y.-W. Mai, “Fracture-Mechanics of a New Blister Test with Stable Crack-Growth,” *Acta Metall. Mater.* 43, 4109-4115 (1995).
- [24] M. K. Kwak, “Vibration of Circular Membranes in Contact with Water,” *J. Acoust. Soc. Am.* 178, 688-690 (1994).
- [25] A. Prak, F. R. Blom, M. Elwenspoek, and T. S. J. Lammerink, “Q-Factor and Frequency-Shift of Resonating Silicon Diaphragms in Air,” *Sensors Actuators A.* 25-27, 691-698 (1991).
- [26] S. Inaba and K. Hane, “Resonance frequency shifts of a photothermal vibration in vacuum,” *J. Vac. Sci. Technol. A.* 9, 2138-2139 (1991).
- [27] K. Hane, T. Iwatuki, S. Inaba, and S. Okuma, “Frequency shift on a micromachined resonator excited photothermally in vacuum,” *Rev. Sci. Instrum.* 63, 3781-3782 (1992).
- [28] H. S. Skulason, P. E. Gaskell, and T. Szkopek, “Optical reflection and transmission properties of exfoliated graphite from a graphene monolayer to several hundred graphene layers,” *Nanotechnology* 21, 295709 (2010).
- [29] F. J. Nelson, V. K. Kamineni, T. Zhang, E. S. Comfort, J. U. Lee, and A. C. Diebold, “Optical properties of large-area polycrystalline chemical vapor deposited graphene by spectroscopic ellipsometry,” *Appl. Phys. Lett.* 97, 253110 (2010).
- [30] X. Sun, R. Hong, H. Hou, Z. Fan, and J. Shao, “Optical properties and structures of silver thin films deposited by magnetron sputtering with different thicknesses,” *Chin. Phys. Lett.* 4, 366-369 (2006).
- [31] E. D. Palik, “Handbook of Optical Constants of Solids,” Academic, New York, (1985).

## Chapter 4

# Miniature all-silica micro-cavity pressure sensors

### 4.1 Introduction

FPIs with all-silica diaphragms have been widely investigated for pressure measurements, and they have shown advantages such as high sensitivity, compact size, and capacity to work in high temperature. A number of techniques including the CO<sub>2</sub> laser bonding [1], the electrical arc fusion splicing [2], and the epoxy bonding [3] have been developed to fabricate the FPIs. However, the majority of these techniques require careful cleaving, polishing or hazardous chemical etching which increase the complexity of the fabrication process especially for the miniature fiber tip. Moreover, the FPI fabricated by these methods are the assembly of elements with different structures, which may undermine the mechanical strength and temperature stability of the sensor.

In this chapter, we develop a novel fiber-tip micro-cavity pressure sensor fabricated by simply using a fusion splicer. The micro-cavity has an all-silica structure and the whole fabrication process does not need careful cleaving and chemical etching. As the micro-cavity is directly melted into the fiber end, the pressure sensor based on this micro-cavity shows high mechanical strength and excellent high-temperature sustainability and may be used for pressure measurements in harsh environments.

## 4.2 Fabrication of the fiber-tip micro-cavities

The micro-cavity is fabricated at the tip of a single mode fiber (SMF) by two steps as shown in Fig. 4.1.

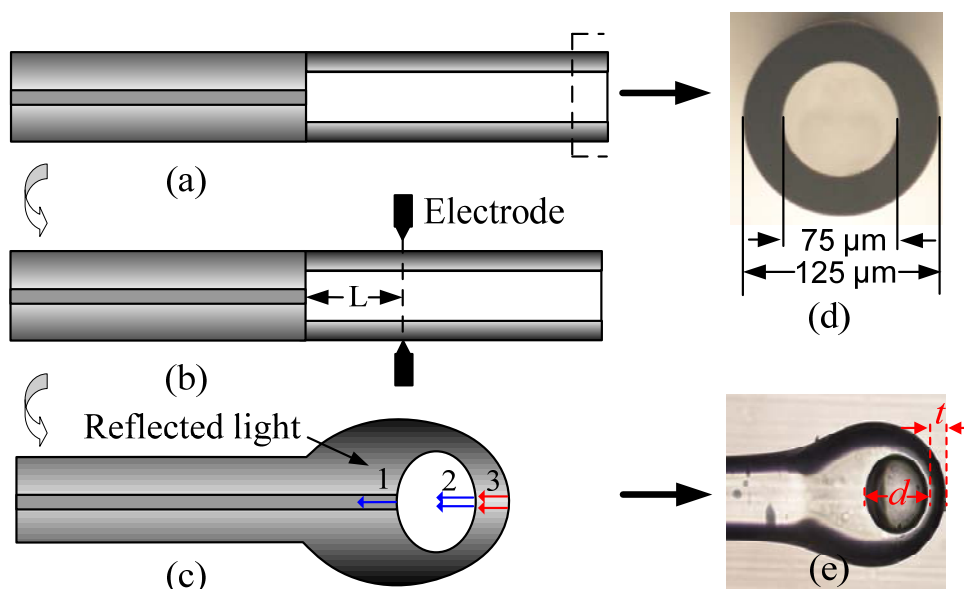


Fig. 4.1 Fabrication process for the fiber-tip micro-cavity. (a) Splicing the capillary with the SMF28; (b) melt the capillary at a distance of  $L$  from the spliced joint; (c) schematic image for the fiber-tip micro-cavity; Microscope images of (d) the cross-section of the capillary; (e) the micro-cavity.

**Step1:** a conventional SMF (SMF28, Corning) is spliced with a section of capillary (Polymicro, the cross-section shown in Fig. 4.1(d)) with the outer and inner diameter of  $126\ \mu\text{m}$  and  $75\ \mu\text{m}$  by using the Ericsson FSU-975 fusion splicer as shown in Fig. 4.1(a). The fusion time and fusion current of the splicer are set to  $0.3\ \text{s}$  and  $12\ \text{mA}$ , respectively.

**Step2:** the spliced joint is moved horizontally with a translation stage so that the position of the splicer electrodes offsets the splice joint by a distance of  $L$ . An arc discharge is then applied to the capillary (Fig. 4.1(b)) with the fusion time and current increased to  $1\ \text{s}$  and  $20\ \text{mA}$ . During the arc discharge, the capillary is melted and separated into two parts. For the part connected to the SMF, the air in the capillary is

trapped during the melting process and a micro-cavity with a sphere-like shape is firmly attached to the fiber end, as shown in Fig. 4.1(c). The sphere-like shape of the micro-cavity might rise from the isotropic air pressure in the micro-cavity during the melting process.

The reflection spectrum of the FPI is measured by using a broadband source (BBS) which is comprised of five light emitting diodes (LEDs) with the working wavelength from 1200 to 1700 nm. The reflected light from a circulator is detected by an optical spectrum analyzer (OSA) with a resolution of 0.01 nm.

Fig. 4.2(a) shows the measured reflection spectrum of the micro-cavity. The interference pattern is induced by the three-wave interference from three surfaces: (1) the fiber end surface, (2) the inner surface and (3) the outer surface of the micro-cavity silica wall, as indicated in Fig. 4.1(c). To simplify the demodulation of the reflection spectrum, two-wave interference (waves reflected from surface 1 and 2) is desirable and this can be easily implemented by roughing or blackening the surface 3 of the micro-cavity. Fig. 4.2(b) shows the reflection spectrum of the micro-cavity after blackening the surface 3 with a matt black aerosol paint and a two-wave interference pattern with the fringe visibility up to 10 dB is observed.

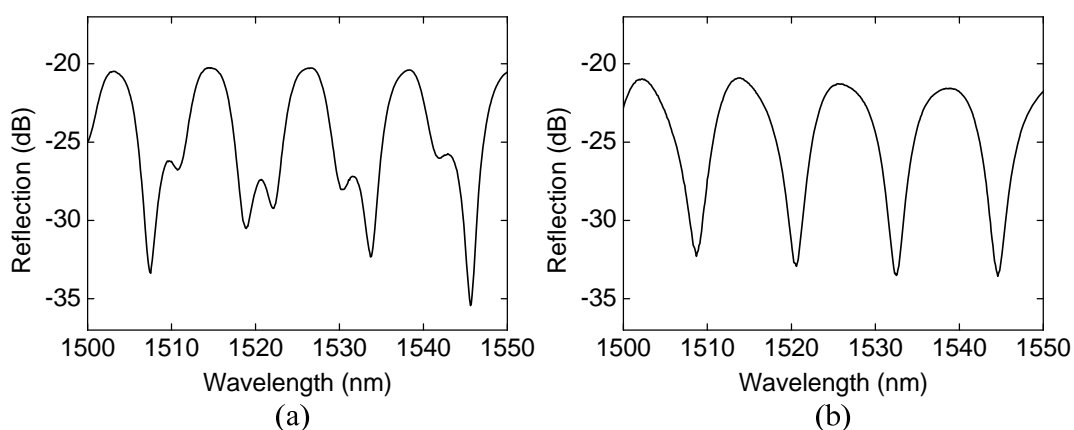


Fig. 4.2 Reflection spectrums of the micro-cavity FPI without (a) and with (b) the reduction of the light reflection from the surface 3 (as shown in Fig. 4.1(c)).

Fig. 4.3 presents the dependence of the cavity length  $d$  (i.e. the length of the air

cavity between the surface 1 and 2) and the thickness of the silica wall  $t$  on the offset distance  $L$ . The cavity length  $d$  and the silica wall thickness  $t$  (Fig. 4.1(e)) both increase with the offset distance  $L$ . Images of fiber-tip micro-cavities with different values of  $d$  and  $t$  are shown in Fig. 4.4.

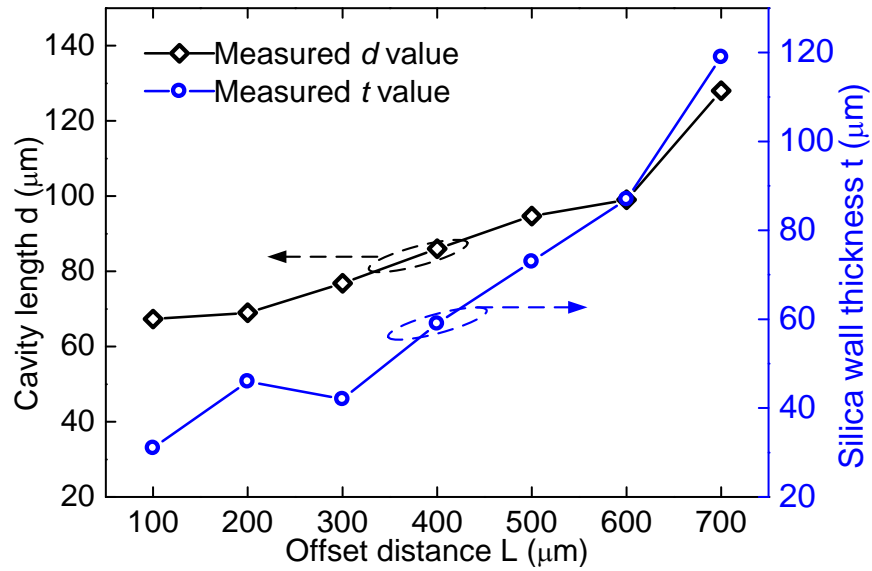


Fig. 4.3 Dependence of the air cavity length  $d$  and the silica wall thickness  $t$  on the offset distance  $L$ .

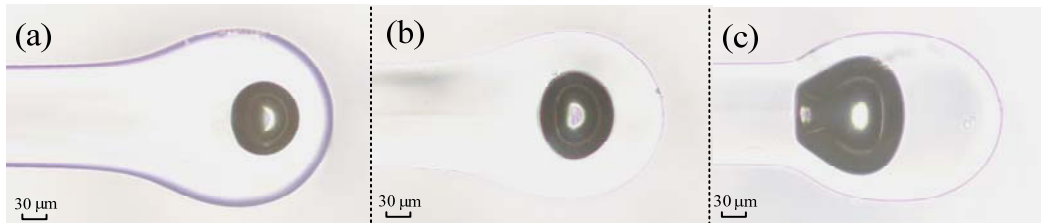


Fig. 4.4 Fiber-tip micro-cavities fabricated by the use of different offset distances  $L$ . (a) 300  $\mu\text{m}$ ; (b) 400  $\mu\text{m}$ ; (c) 700  $\mu\text{m}$ .

The wavelength spacing  $\Delta\lambda$  is related to the cavity length by,

$$\Delta\lambda = \frac{\lambda^2}{2nd} \quad (4.1)$$

where  $\lambda$  is the wavelength of light,  $n$  is the refractive index of the micro-cavity ( $n \approx 1$ ) and  $d$  is the cavity length. Fig. 4.5 shows the wavelength spacing of the reflection spectrums of the micro-cavities with different cavity lengths at the wavelength

around 1520 nm. The measured values agree well with the calculated curve and the slight difference might result from the inaccuracy of the air cavity length measured by the microscope due to the refraction of the light from the spherical air cavity as well as the selection of the focal plane.

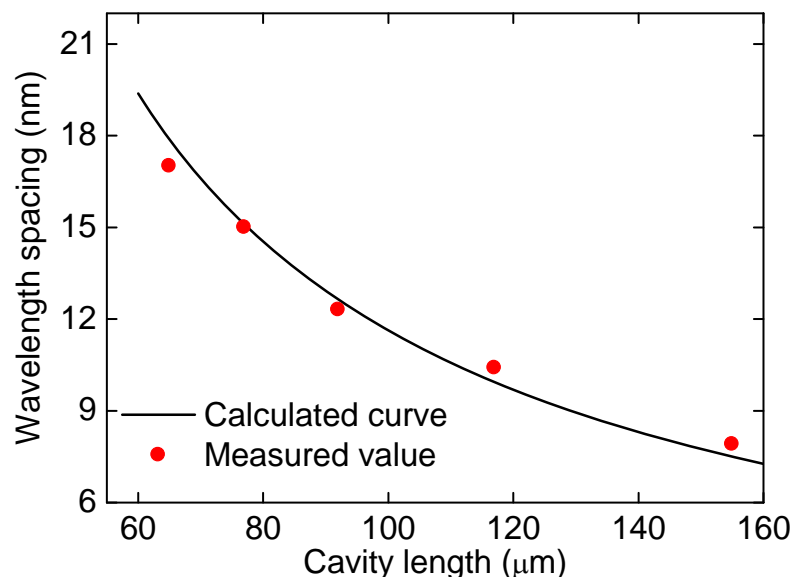


Fig. 4.5 Relation between the wavelength spacing of the reflection spectrum and the cavity length of the micro-cavity.

The experimental results show that the above fiber-tip micro-cavities have demonstrated good mechanical strength without being broken under a transverse load of 5 N and high temperature sustainability up to 1000 °C. Consequently, the micro-cavity may be used as a high temperature sensor or a transverse load sensor [4]. However, to behave as a pressure sensor, the micro-cavity exhibits a limited pressure sensitivity which is inversely dependent on the thickness of the silica wall. The silica walls of the micro-cavities are typically thicker than 20  $\mu\text{m}$  as shown in Fig. 4.3 and 4.4. In order to improve the pressure sensitivity of the micro-cavity, a pressure-assisted tapering of the capillary is introduced to reduce the silica-wall thickness of the micro-cavity.

## 4.3 Pressure sensitivity enhancement by the pressure-assisted tapering

### 4.3.1 Pressure-assisted tapering

Compared to the fabrication process described previously in Fig. 4.1, the capillary after being offset from the splicing joint by a distance of  $L$  ( $\sim 50 \mu\text{m}$ ) is tapered by the fusion splicer instead of being directly melted by a large arc discharge, as illustrated in Fig. 4.6(a).

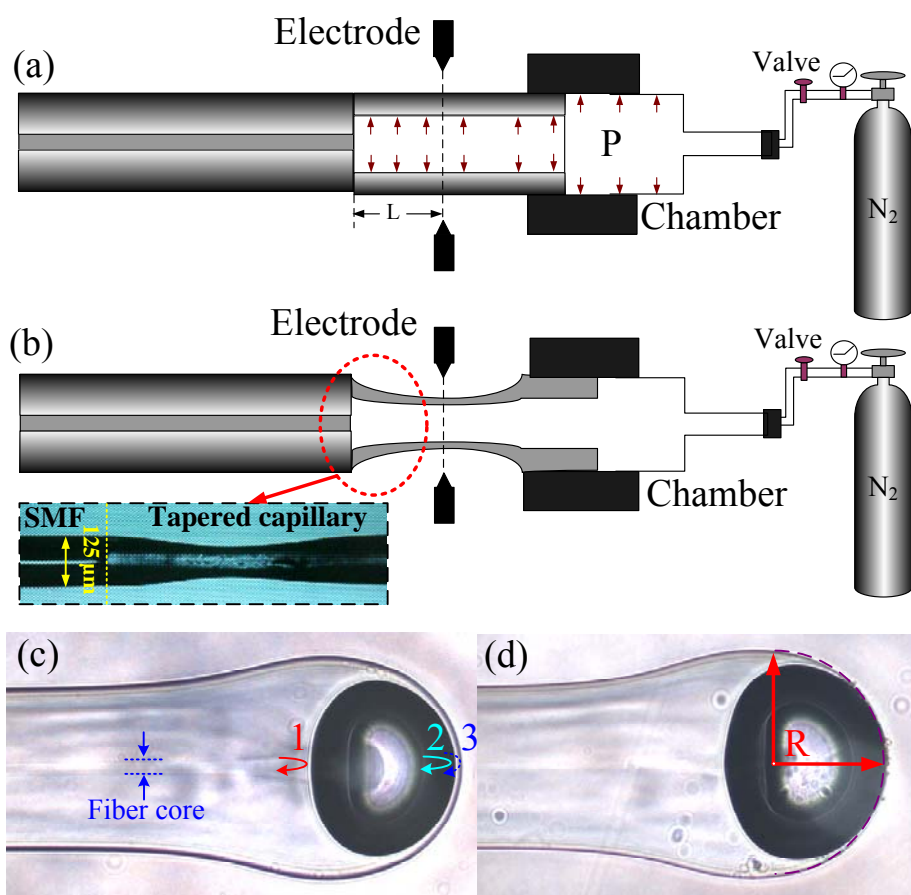


Fig. 4.6 Pressure-assisted fabrication process for the decrease of the wall thickness of the micro-cavity sensor: (a) tapering the capillary under the assistance of pressure; (b) melting the taper by applying an electric arc; (c) and (d) show the microscope images of the fabricated micro-cavities with the silica-wall thickness  $t$ , respectively  $\sim 6 \mu\text{m}$  and  $2.2 \mu\text{m}$ . Microscope image of the tapered capillary is shown in the inset in (b).

The tapering process is completed by an automatic three-step procedure of the fusion splicer, with proper settings of the fusion current and duration as listed in Table 4.1. The whole process takes less than 1 minute. To avoid the possible collapse of the capillary during the tapering, the other end of the capillary is pressurized by a nitrogen gas chamber with the gas pressure of  $\sim 3$  Bar, as shown in Fig. 4.6(a). The wall thickness of the internally pressurized capillary can be tapered down to a few micrometers and the diameter of the capillary after the tapering is estimated to be  $78 \mu\text{m}$  under a microscope (the inset of Fig. 4.6(b)).

Table 4.1 Settings of the fusion current and duration for the tapering process.

<i>Step number</i>	<i>Fusion current (s)</i>	<i>fusion duration (s)</i>
1	8.5	5
2	7.5	8
3	6.5	4

The gas inside the capillary is then released to recover the pressure in the capillary to the atmosphere. After the pressure is stable, a strong electric arc discharge with the fusion current of 20 mA is applied to the tapered capillary waist, which automatically separates the capillary and forms an internal spherical micro-cavity at the fiber end as shown in Fig. 4.6(c) or (d).

The cavity length  $d$  and the silica wall thickness  $t$  of the micro-cavities in Fig. 4.6(c) and Fig. 4.6(d) are estimated from the microscope images to be  $107 \mu\text{m}$  and  $6 \mu\text{m}$ , and  $120 \mu\text{m}$  and  $2.2 \mu\text{m}$ , respectively. The thinnest silica wall we obtained during the experiment is  $\sim 2.2 \mu\text{m}$ . For micro-cavities with the silica-wall thickness at the micrometer scale, slight variation of arc discharge could melt the silica wall and thus collapse the air cavity. Further reduction of the silica-wall thickness might be achieved by the use of a more stable electrical arc discharge.

Compared to the micro-cavity fabricated by just a large electric arc as illustrated in Fig. 4.1, the pressure-assisted tapering process used here significantly reduce the silica-wall thickness of the micro-cavity. In addition, the whole fabrication process is

still simple since the tapering process can be automatically finished by the splicer.

### 4.3.2 Interrogation of the fiber-tip micro-cavity sensors

Fig. 4.7 shows the measured reflection spectrums of two micro-cavity sensors with different values of the air-cavity length and the silica-wall thickness. The variation of the fringe visibility results from the effect of the three-wave interference. Due to the low reflectivity of the silica/air interface (typically lower than 3.5%), higher-order reflections from the surfaces of the micro-cavity can be ignored [5].

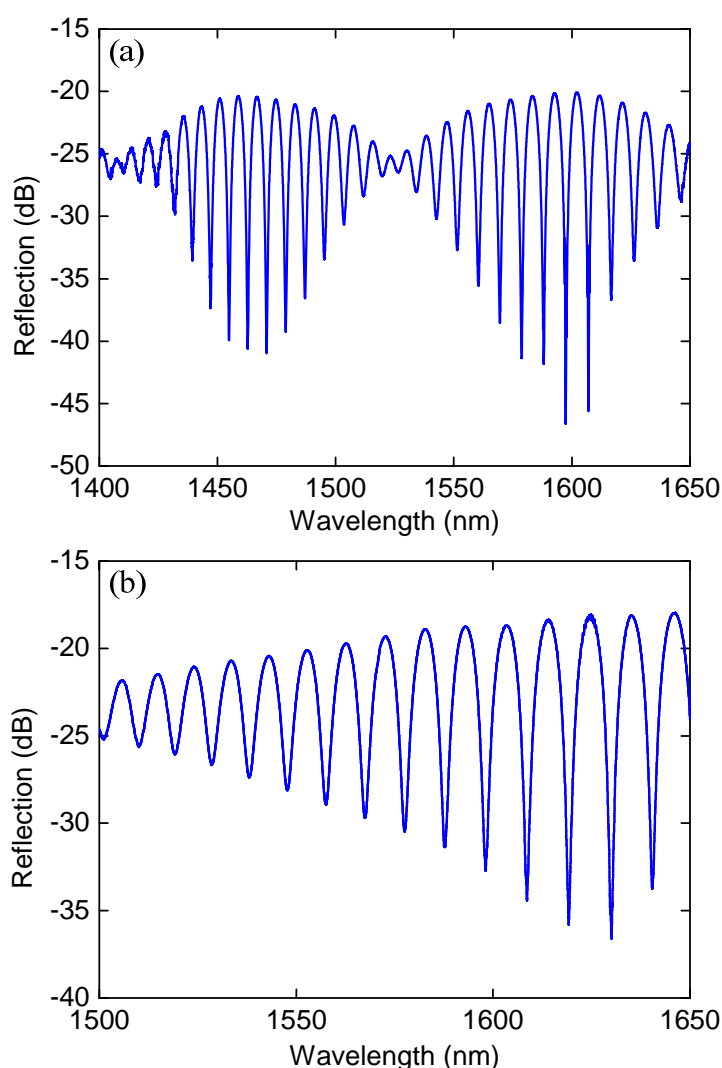


Fig. 4.7 Measured reflection spectrums of the micro-cavity sensors with the air cavity length/silica wall thickness of (a) 134  $\mu\text{m}$ /6.2  $\mu\text{m}$ ; (b) 120  $\mu\text{m}$ /2.2  $\mu\text{m}$ , respectively.

The length of the air cavity  $L$  and the thickness of the silica wall  $t$  can be estimated from the wavelength spacing of the interference fringes and that of the large envelope of the interference fringes, respectively. The values for  $L$  and  $t$  are calculated to be  $134\ \mu\text{m}$  and  $6.2\ \mu\text{m}$  for the sample in Fig. 4.7(a), and  $120\ \mu\text{m}$  and  $2.2\ \mu\text{m}$  for the sample in Fig. 4.7(b).

If the three reflective surfaces of the micro-cavity (the SMF fiber end, inner and outer side surface of the silica wall) are regarded as plane mirrors with equivalent reflectivities of  $R_1$ ,  $R_2$  and  $R_3$ , the cavity length  $L$  and the thickness  $t$  can also be acquired by curve fitting the measured interference spectrum through the three-beam interference approximation discussed in Chapter 2, as shown in Fig. 4.8. Here, the effect of the spherical shape of the silica wall on the reflection spectrum is ignored by approximating the silica wall as a plane. The extra phase shift caused by the spherical shape can be analyzed by treating the light waves with the Gaussian beam model [6].

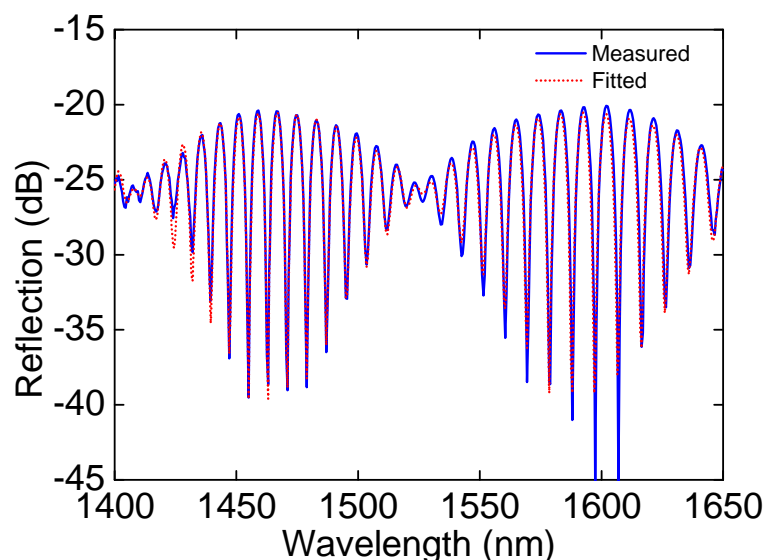


Fig. 4.8 Curve fitting of the measured spectrum as shown in Fig. 4.7(a).

The cavity length and the thickness of the micro-cavity are fitted to be  $130\ \mu\text{m}$  and  $6.3\ \mu\text{m}$ , respectively, which are similar to the values calculated directly from the wavelength spacing of the interference spectrum. Theoretically, the curve fitting

method can accurately demodulate the cavity length change of the micro-cavity for pressure measurements while the fitting process is time-consuming. Due to the small silica wall of the micro-cavity, the light reflected from its outer surface just modulates the fringe envelope of the interference spectrum slightly over one period of the interference fringes [7]. Therefore, directly detecting the peak/dip wavelength shift of the interference spectrum is used to demodulate the pressure-induced deformation of the thin silica wall.

#### 4.4 Pressure and temperature responses

The pressure response of the micro-cavity sensor is measured as shown in Fig. 4.9. The sensor head was inserted into an oil-filled chamber which was connected with a pressure controller and a calibrated pressure meter. The magnitude of the pressure in the chamber was monitored by the pressure meter and was increased from 0 to 40 Mpa with a step of 5 Mpa by the controller.

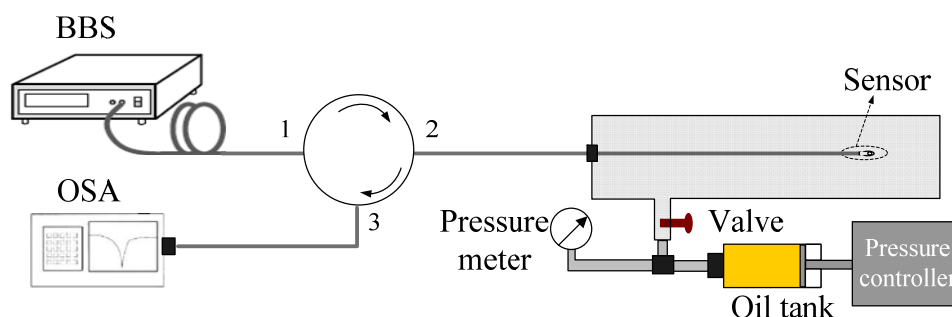


Fig. 4.9 Experimental setup for the pressure measurement.

Fig. 4.10(a) shows the pressure response of the micro-cavity with the cavity length  $d$  and silica wall thickness  $t$  of 123  $\mu\text{m}$  and 11.4  $\mu\text{m}$ , respectively. With the increase of the applied pressure, the peak/dip wavelength of the interference fringe of the micro-cavity shifts toward short wavelength. The three-wave modulation is alleviated in the spectrum due to the reduction of the light reflected by the outer surface of the silica wall when the micro-cavity is immersed into the oil. Fig. 4.10(b)

shows the shifts of the dip wavelengths of the interference spectrums for three samples with different cavity parameters. Around the wavelength of  $\sim 1550$  nm, the sensors show linear responses to the pressure with the values of adjusted R-Square larger than 0.99995. The slope of the curve, i.e., the pressure sensitivity, increases with the reduction of the wall thickness  $t$ .

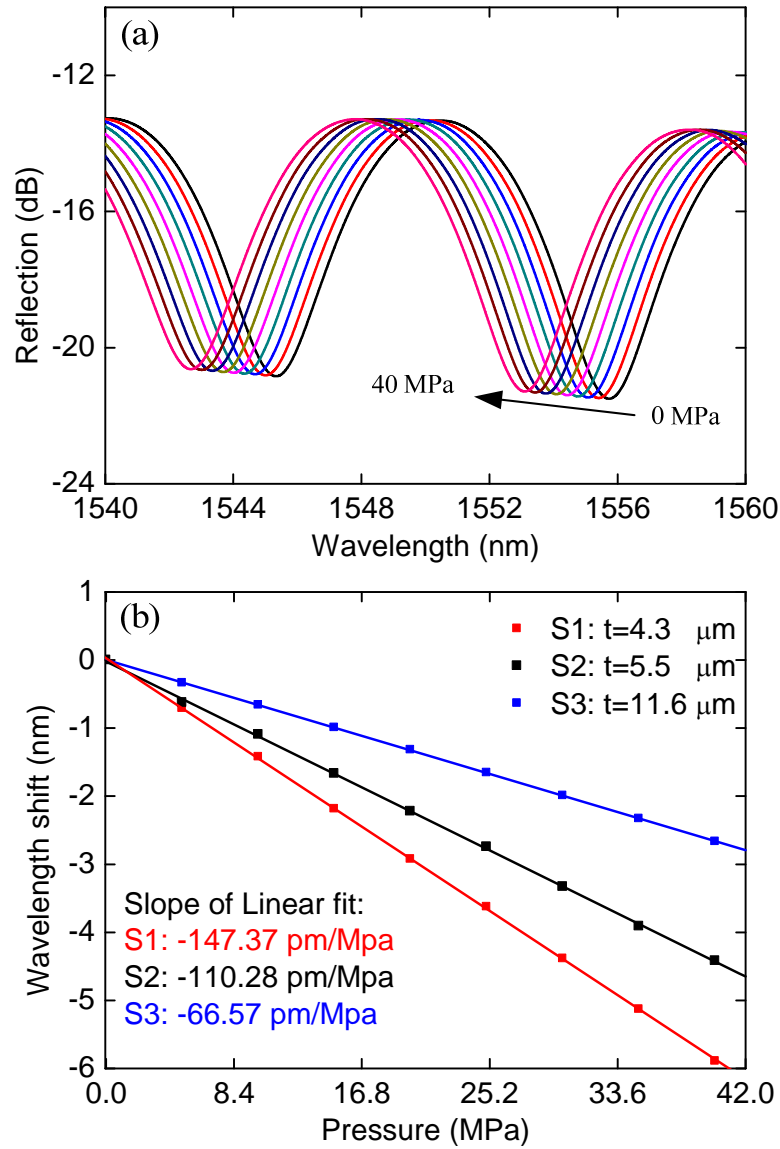


Fig. 4.10 (a) Pressure response of the micro-cavity sensor with  $t=11.4 \mu\text{m}$  and  $d=123 \mu\text{m}$ ; (b) wavelength shifts as functions of the applied pressure for three cavity sensors with different parameters. S1: ( $t=4.3 \mu\text{m}$ ,  $d=130 \mu\text{m}$ ), S2: ( $t=5.5 \mu\text{m}$ ,  $d=132 \mu\text{m}$ ), S3: ( $t=11.4 \mu\text{m}$ ,  $d=123 \mu\text{m}$ ).

The wavelength shift  $\Delta\lambda$  of the interference spectrum due to the change of the cavity length  $\Delta d$  can be described by  $\Delta\lambda = \lambda \cdot \Delta d / d$ . If the micro-cavity is considered approximately equivalent to a thin silica semi-spherical shell attached to the end of a SMF, the cavity length change  $\Delta d$  due to the pressure change  $\Delta p$  can be expressed as [3],

$$\Delta d = \frac{(1-\nu)R^2\Delta p}{2Et} \quad (4.2)$$

where  $\nu$  is the Poisson's ratio,  $E$  is the Young's modulus of silica and  $R$  is the radius of the spherical shell (as shown in Fig. 4.6(d)). For fused silica,  $E = 73$  GPa,  $\nu = 0.17$ .

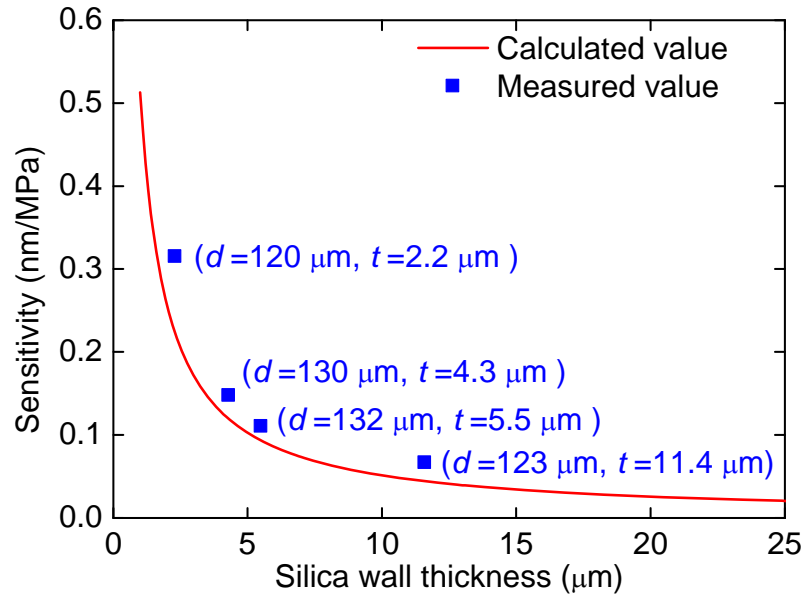


Fig. 4.11 Pressure sensitivity of the micro-cavity sensor as a function of the silica wall thickness  $t$ . In the calculation, the value of  $d$ ,  $R$  and  $\lambda$  used are 130  $\mu\text{m}$ , 87  $\mu\text{m}$  and 1550 nm, respectively.

Fig. 4.11 shows the theoretical and experimental results for the pressure sensitivities of micro-cavities with different values of  $t$  and the calculated values are in agreement with the experimental results. The slight difference between the calculated values and experimental data might arise from the spherical shell approximation of the micro-cavity. When the silica wall thickness  $t$  is less than 2  $\mu\text{m}$ , the pressure sensitivity increases significantly for the micro-cavity with a thinner

silica wall. In our experiments, the thinnest  $t$  we have achieved is  $2.2\ \mu\text{m}$  and the corresponding micro-cavity exhibits a pressure sensitivity of  $\sim 315\ \text{pm/MPa}$ .

As mentioned previously, the further reduction of the wall thickness is limited by the stability of the arc discharge and the accuracy of controlling the fusion current and time in our present experimental setup. Wet etching may be an alternative for further reduction of  $t$  [7], while this might not be needed for large pressure measurements.

The maximal pressure applied in our experiment is  $40\ \text{Mpa}$ , which is limited by the pressure chamber used. To investigate the maximum working pressure of the sensor, the pressure response of micro-cavity is studied by the use of the solid mechanics module (2D axisymmetric) of the finite element modeling software Comsol Multiphysics.

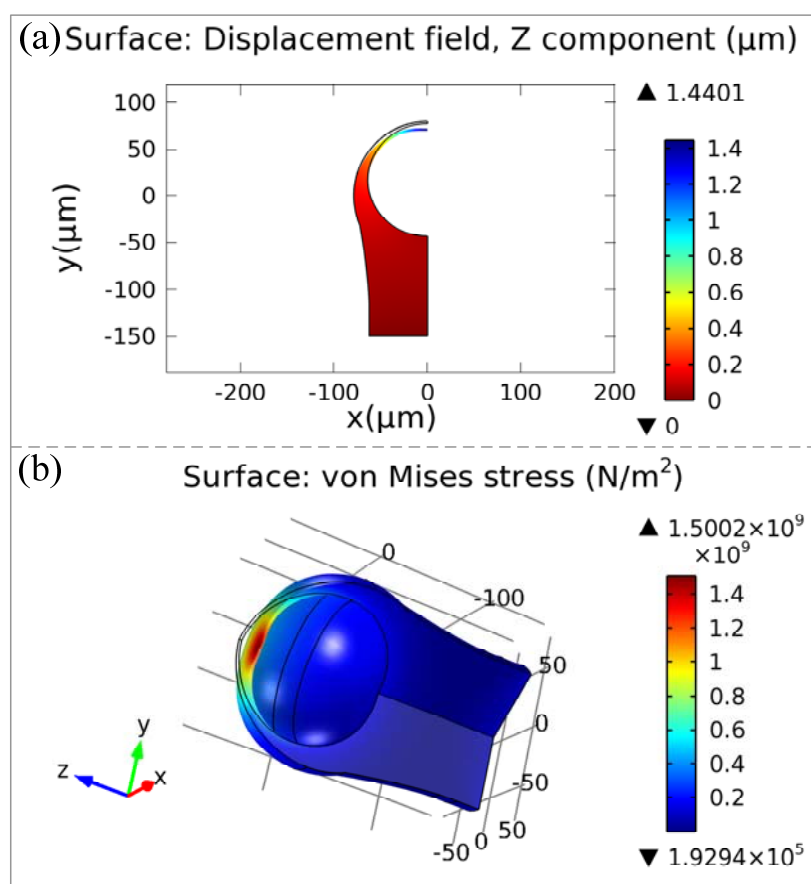


Fig. 4.12 (a) Deflection and (b) von Mises stress distribution in the micro-cavity under the pressure of 70 MPa.

The maximum deflection of the micro-cavity ( $t=2.2\ \mu\text{m}$ ,  $L=120\ \mu\text{m}$ ) under a pressure of 70 MPa is  $\sim 1.44\ \mu\text{m}$ , as shown in Fig. 4.12(a), which corresponds to an average pressure sensitivity (change of cavity length to pressure) of 20.6 nm/MPa. For the wavelength of 1550 nm, the pressure sensitivity (wavelength shift to pressure) is 0.27 nm/MPa. This value is similar to the measured value (see Fig. 4.11) of  $\sim 0.335$  nm/MPa, which corresponds to a silica wall thickness of  $1.7\ \mu\text{m}$  in the simulation.

From Fig. 4.12(b), the maximum von Mises stress locates at the head center where the cavity wall is thinnest. If the maximum strength for the fused silica is taken as 1.5 GPa as listed in Table 3.1, the maximum working pressure of the micro-cavity is  $\sim 70$  MPa. In the simulation, the micro-cavity with a larger wall thickness exhibits an increased maximum working pressure but at the same time a decreased pressure sensitivity.

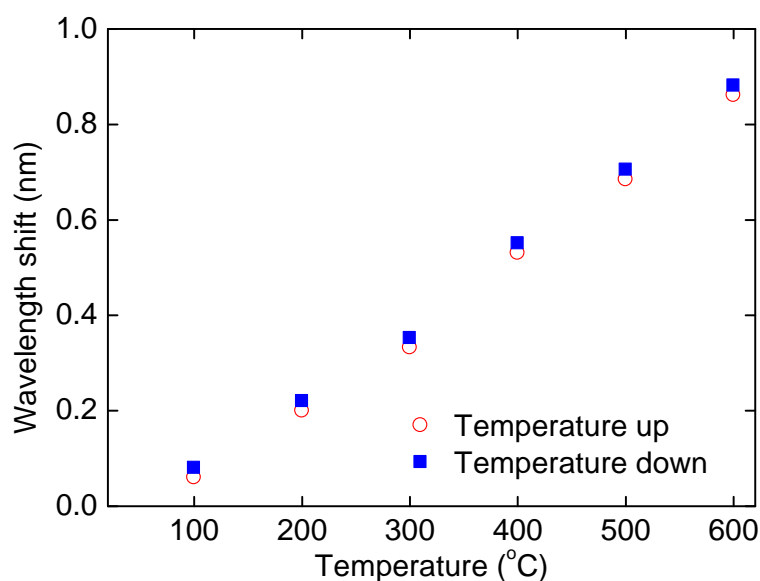


Fig. 4.13 Temperature response of the micro-cavity sensor with  $t = 8\ \mu\text{m}$ .

Due to the all fused-silica structure, the micro-cavity is expected to survive in a high temperature environment. Fig. 4.13 shows the temperature response of micro-cavity with the silica-wall thickness  $t = 8\ \mu\text{m}$ . The sensor works well with good stability up to a temperature of  $600\ ^\circ\text{C}$ , and shows a temperature sensitivity of  $\sim 1.55$

pm/°C. Theoretically, the temperature sensitivity of the micro-cavity may be induced by the thermal expansion of the cavity and the pressure change in the cavity [7].

The temperature sensitivity due to the thermal expansion of the cavity  $S_{T1}$  may be expressed as,

$$S_{T1} = \frac{\Delta\lambda}{\Delta T} = \lambda\alpha \quad (4.3)$$

where  $\alpha=5.5\times 10^{-7}/^{\circ}\text{C}$  is the thermal expansion coefficient of silica. For the wavelength of 1500 nm,  $S_{T1}$  is calculated to be 0.9 pm/°C. This value is of the same order as what we have measured (1.55 pm/°C).

The temperature sensitivity due to the pressure change in the cavity  $S_{T2}$  may be described by,

$$S_{T2} = S_p \frac{\Delta P}{\Delta T} \quad (4.4)$$

where  $S_p$  is the pressure sensitivity of the sensor at the ambient temperature, and  $\Delta P$  is the change of the internal pressure in the cavity resulting from the temperature variation  $\Delta T$ . According to the ideal gas law  $\Delta P/\Delta T = nR/V$ , where  $n$  is the amount of gas in units of mol,  $R$  is the ideal gas constant equal to 8.314 J/(K·mol), and  $V$  is the volume of the air-cavity, the value for  $\Delta P/\Delta T$  at the condition of the atmospheric pressure and room temperature is equal to  $\sim 3.4 \times 10^{-4}$  MPa/°C.

The exact value of  $n$  in the cavity is unknown, but it is smaller than that in the atmospheric pressure since the arc discharge raises the temperature around the cavity, causes expansion of gas, and reduces the gas pressure within the cavity. Thus,  $\Delta P/\Delta T$  is actually less than  $3.4 \times 10^{-4}$  MPa/°C for the micro-cavities developed. If  $S_p$  is assumed to be  $\sim 100$  pm/MPa for the micro-cavity,  $S_{T2}$  is estimated to be less than 0.034 pm/°C. As a result, the temperature sensitivity of the sensor is largely determined by the thermal expansion of the cavity instead of the pressure change in cavity.

For the micro-cavity sensor ( $t = 2.2 \mu\text{m}$ ) with a pressure sensitivity of 315 pm/MPa and a temperature sensitivity  $\sim 1.55 \text{ pm}/^\circ\text{C}$ , its temperature-cross sensitivity can be calculated to be  $\sim 5 \text{ kPa}/^\circ\text{C}$ .

## 4.5 Summary

This chapter describes a novel technique to develop a fiber-tip micro-cavity pressure sensor by simply using a fusion splicer and a pressurization device. The pressure sensitivity of the sensor is inversely proportional to its wall-thickness which is dependent on the fusion time and fusion current during the melting of the capillary. The pressure sensor shows a high mechanical strength up to 40 Mpa and low temperature cross-sensitivity of  $\sim 5 \text{ kPa}/^\circ\text{C}$ . For applications involving large pressures or small temperature fluctuations, the sensor can be used without the temperature calibration, and for applications with larger temperature excursions, the influence of temperature may be compensated taking advantage of the linear temperature response of the sensor. Compared to the flat diaphragm based pressure sensor, the micro-cavity pressure sensor shows a lower pressure sensitivity ( $\sim 315 \text{ pm}/\text{Mpa}$ ) because of the spherical structure of the sensor head. As discussed in Chapter 3, the pressure sensitivity of the diaphragm with a spherical shape exhibits a significantly smaller dependence on the physical size of the diaphragm, which means that the spherical diaphragm offers a smaller increase than the flat diaphragm for the equal reduction of the diaphragm thickness. The next chapter will introduce the flat diaphragm based FPI pressure sensors with greatly higher pressure sensitivities.

## References for Chapter 4

- [1] J. Xu, X. Wang, K. L. Cooper, and A. Wang, "Miniature all-silica fiber optic

- pressure and acoustic sensors,” *Opt. Lett.* 30, 3269-3271 (2005).
- [2] D. Donlagic and E. Cibula, “All-fiber high-sensitivity pressure sensor with SiO<sub>2</sub> diaphragm,” *Opt. Lett.* 30, 2071-2073 (2005).
- [3] J. P. Dakin, W. Ecke, K. Schroeder, and M. Reuter, “Optical fiber sensors using hollow glass spheres and CCD spectrometer interrogator,” *Opt. Laser Eng.* 47, 1034-1038 (2009).
- [4] J. Ma, J. Ju, L. Jin, W. Jin, and D. Wang, “Fiber-tip micro-cavity for temperature and transverse load sensing,” *Optics Express* 19, 12418-12426 (2011).
- [5] J. Villatoro, V. Finazzi, G. Coviello, and V. Pruneri, “Photonic-crystal-fiber-enabled micro-Fabry-Perot interferometer,” *Opt. Lett.* 34, 2441-2443 (2009).
- [6] E. Li, G. -D. Peng, and X. Ding, “High spatial resolution fiber-optic Fizeau interferometric strain sensor based on an in-fiber spherical microcavity,” *Appl. Phys. Lett.* 92, 101117 (2008).
- [7] Y. Zhu, K. L. Cooper, G. R. Pickrell, and A. Wang, “High-temperature fiber-tip pressure sensor,” *J. Lightwave Technol.* 24, 861-869 (2006).

## Chapter 5

# Graphene diaphragm based FPI pressure and acoustic sensors

### 5.1 Introduction

The theory for the pressure induced deflection of diaphragm suggests that the pressure sensitivity of a diaphragm based FPI pressure sensor can be improved by reducing the diaphragm thickness [1]. However, the reduction of the diaphragm thickness is limited by the fabrication techniques and the mechanical strength of the diaphragm itself. Taking the silica diaphragm as an example, it is difficult to achieve a diaphragm thickness less than 1  $\mu\text{m}$  despite that considerable efforts such as polishing or chemical (hydrofluoric acid) etching have been made [2-4]. To our knowledge, the thinnest diaphragm reported for the diaphragm based FPI pressure sensor is the silver diaphragm with a thickness of  $\sim 100$  nm [5]. Compared to the silica with a mechanical strength of  $\sim 1.5$  GPa, the graphene exhibits a much higher value of  $\sim 130$  GPa due to its carbon-carbon covalent bond [6]. The high mechanical strength supports the high quality graphene diaphragm with the thickness down to even several nanometers and also enables easy handling of the graphene without being easily damaged during the fabrication process of the sensor. Therefore, the ultra-small thickness and highly strong mechanical strength of the graphene film support itself as a promising candidate for constructing miniature and high-sensitivity pressure/acoustic sensors.

This chapter describes the fabrication, the interrogation and the pressure/acoustic response measurement of the graphene diaphragm based FPIs. A few-layer graphene

diaphragm with a thickness at the nanometer scale is transferred onto a fiber tip with an air cavity to build a fiber-tip FPI pressure sensor; a multi-layer graphene diaphragm with a thickness of ~100 nm is transferred to a ferrule endface to build a ferrule-top acoustic sensor.

## 5.2 Graphene diaphragm

In this section, the preparation, transferring and characterization of the graphene diaphragm are introduced.

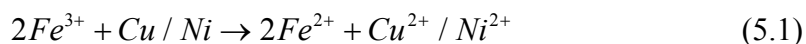
### 5.2.1 Graphene preparation and transferring

The graphene films used in the experiment are grown on metal substrates by using the chemical vapor deposition (CVD) method. Table 5.1 lists the properties of graphene samples including the single-layer graphene (SLG), the few-layer graphene (FLG; 2-9 layers) and the multi-layer graphene (MLG; 10 or more layers) [7].

Table 5.1 List of the properties of the CVD graphene samples.

<i>Sample name</i>	<i>Substrate</i>	<i>Metal thickness (<math>\mu\text{m}</math>)</i>	<i>Layer number</i>
<i>single-layer</i>	<i>Cu foil</i>	<i>20</i>	<i>1</i>
<i>few-layer</i>	<i>Ni/SiO<sub>2</sub>/Si</i>	<i>0.02</i>	<i>1-7 (not uniform)</i>
<i>multi-layer</i>	<i>Ni foil</i>	<i>25</i>	<i>~300</i>

Before the characterization of the graphene samples, the graphene on the metal substrate is usually transferred to a SiO<sub>2</sub>/Si substrate. The process for transferring the graphene film is schematically plotted in Fig. 5.1. The metal foil beneath the graphene is etched away by the iron chloride (FeCl<sub>3</sub>) solution with the concentration of 0.05 mg/mL as shown in Fig. 5.1(a). The etching process can be described by the net ion reaction equation as follows,



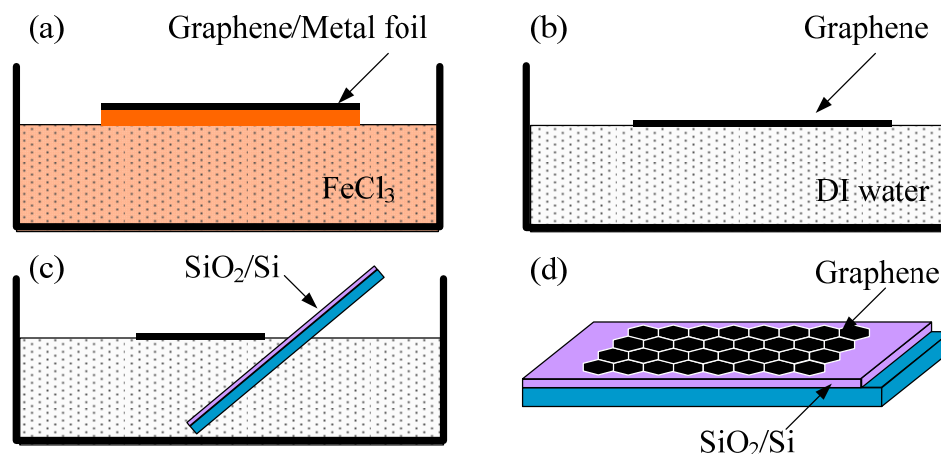


Fig. 5.1 Schematic diagram of transferring the graphene from the CVD graphene samples to a SiO<sub>2</sub>/Si substrate. (a) Graphene/metal foil on the FeCl<sub>3</sub> solution; (b) graphene floated on the DI water; (c) scooping the graphene with a SiO<sub>2</sub>/Si substrate; (d) graphene on the SiO<sub>2</sub>/Si substrate.

After the metal is totally removed, the graphene film is scooped from the FeCl<sub>3</sub> solution into the de-ionized (DI) water (Fig. 5.1(b)). The graphene is repeatedly transferred into the fresh DI water for several times to remove the residual ions (Fe, Cu/Ni). Finally, a clean SiO<sub>2</sub>/Si substrate is used to scoop the graphene onto its surface (Fig. 5.1(c)) and the SiO<sub>2</sub>/Si substrate with the graphene is heated to dry at 90 °C for ~30 minutes.

## 5.2.2 Graphene characterization

### 5.2.2.1 Microscope images of the graphene

Fig. 5.2 shows the microscope images of the graphene films with different layer numbers after being transferred onto the SiO<sub>2</sub>/Si substrate. The graphene with a different layer number shows a different color due to the interference of lights from the graphene and the SiO<sub>2</sub>/Si substrate. The thickness of the SiO<sub>2</sub> layer on the Si substrate is ~ 300 nm.

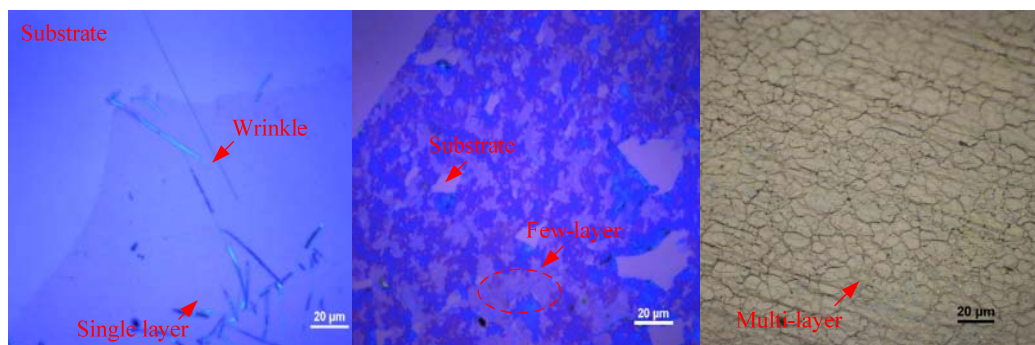


Fig. 5.2 Microscope images of the SLG, FLG and MLG transferred onto the SiO<sub>2</sub>/Si substrate.

The SLG has a uniform thickness (mostly one layer) and shows a light blue (Fig. 5.2(a)). The FLG shows no uniform thickness over the whole area and looks like a patchwork as shown in Fig. 5.2(b). The light blue areas are single or bi-layer graphene, and the dark blue regions are the graphene with more layers. For the MLG with a thickness of 100 nm in Fig. 5.2(c), it can be considered as a common graphite film [8].

### 5.2.2.2 Atomic force microscope images of the graphene

The values of the thickness of the SLG, FLG and MLG after being transferred onto the SiO<sub>2</sub>/Si substrate are measured with an atomic force microscope (AFM, model: XE-100 park system). The AFM works in the tapping mode and the measured AFM images and the corresponding height values of the graphene films are given in Fig. 5.3. For the SLG, the measured thickness is ~ 1 nm, which is larger than the thickness of the pristine monolayer graphene ~ 0.335 nm. This has been found to be caused by the chemical contrast between the substrate and the graphene which induces a chemical thickness of 0.5 nm-1 nm [9]. For the FLG, the larger average thickness measured by the AFM might result from the no-uniform thickness of the film itself and the wrinkles formed during the transferring process especially at the location where the film is broken [10, 11]. The thickness of the MLG measured by the AFM is similar to the value (~100 nm) given in the datasheet of the MLG products.

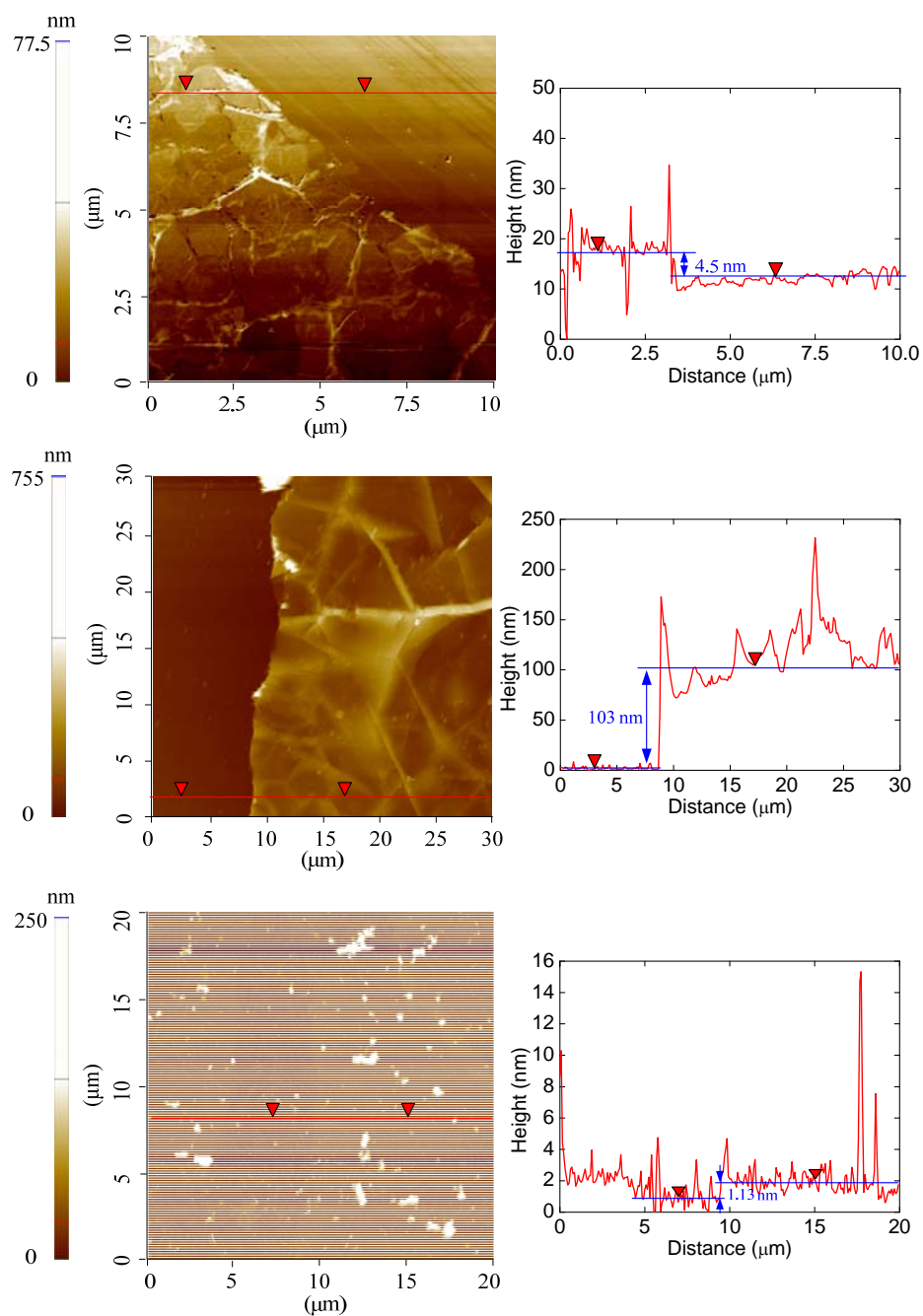


Fig. 5.3 AFM images of (a) the single-layer, (b) the few-layer and (c) the multi-layer graphene transferred on the  $\text{SiO}_2/\text{Si}$  substrate.

### 5.2.2.3 Raman spectrum

Compared to the AFM, the Raman spectroscopy is an efficient and easy way to identify the SLG, FLG and MLG. The Raman spectrum is measured by illuminating

the sample with a 488 nm excitation light after being focused by a 100× objective lens and the measurement can be completed in minutes. As shown in Fig. 5.4, the SLG exhibits a sharp and symmetrical  $G'$  peak ( $\sim 2700\text{ cm}^{-1}$ ) with a bandwidth of  $30\text{ cm}^{-1}$  as acquired by the Lorentz fitting. In contrast, for the FLG, a broader and asymmetry  $G'$  peak is observed. For the MLG, the  $G'$  peak can be fitted by two separate peaks and is similar to the  $G'$  peak of the graphite. In addition to the  $G'$  peak, the intensity ratio of the  $G$  ( $\sim 1580\text{ cm}^{-1}$ ) and  $G'$  peak also shows obvious difference for the graphene samples and can be used to distinguish the SLG and FLG [12]. The large intensity of the  $D$  peak ( $\sim 1350\text{ cm}^{-1}$ ) for the SLG and FLG might be due to the damage induced in the graphene film during the process of transferring the graphene film onto the  $\text{SiO}_2/\text{Si}$  substrate.

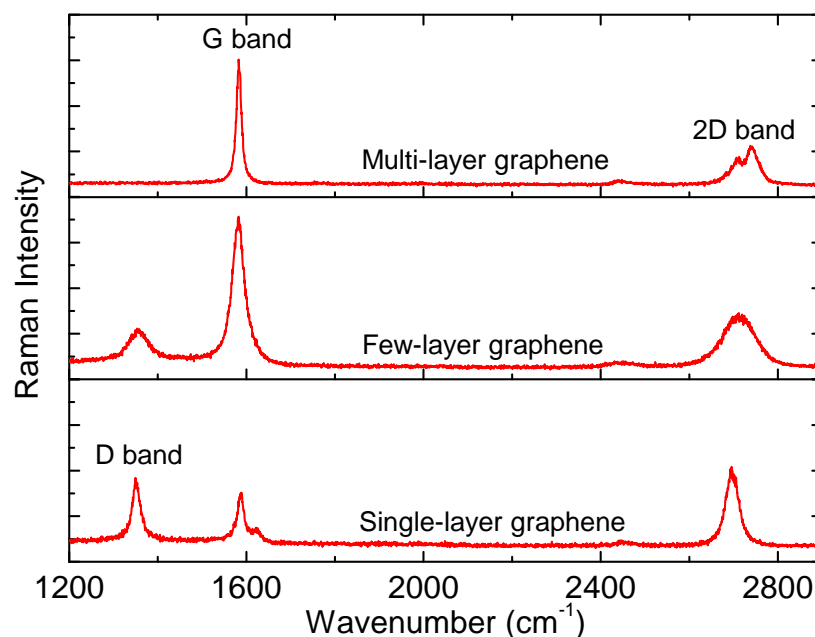


Fig. 5.4 Raman spectrums of the single, few and multi-layer graphene.

### 5.3 Fiber-tip FPI with the few-layer graphene diaphragm

In this section, the fabrication of the fiber-tip FPI with the FLG diaphragm is

described.

### 5.3.1 Fabrication and interrogation

Fig. 5.5 shows the schematic images of employing the graphene as the deflectable diaphragm on the fiber tip for pressure sensing. The fabrication of the graphene based FPI can be divided into two steps:

**Step 1:** fabricating an open micro-cavity with a depth of several tens of microns at the single mode fiber (SMF) tip (Fig. 5(b));

**Step 2:** sealing the micro-cavity by the use of the graphene diaphragm with the nanometer scale thickness (Fig. 5(c)).

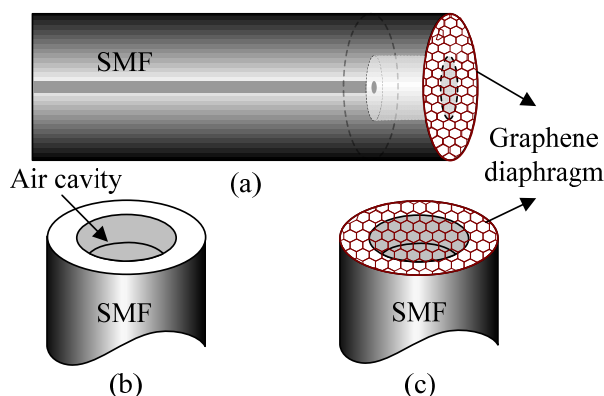


Fig. 5.5 Schematic of (a) the graphene diaphragm based FPI pressure sensor; (b) an open air-cavity on the fiber end; (c) the cavity covered with the graphene diaphragm.

The micro-cavity at the fiber tip is fabricated by firstly splicing a SMF28 (Corning) with a section of pure silica capillary (Polymicro) with an inner air hole diameter of  $25\ \mu\text{m}$  by using the Ericsson FSU-975 fusion splicer, as shown in Fig. 5.6(a). The fusion currents and fusion times of the three-step splicing procedure are set as follows: 10 mA/0.2 s, 11.5 mA/0.2 s and 10.6 mA/0.4 s. The capillary is then cut at a distance of a few tens of micrometers from the splice joint with the aid of a microscope as plotted in Fig. 5.6(b) and (c).

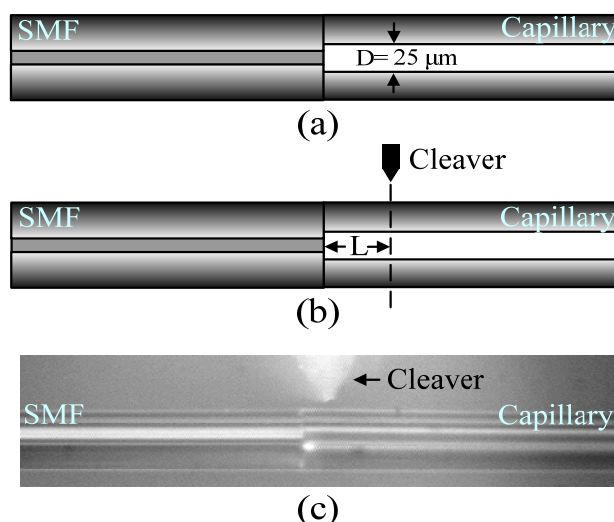


Fig. 5.6 Schematic of (a) a SMF spliced with a section of capillary and (b) the capillary cut by the cleaver at a distance of  $L$  from the splicing joint; (c) the microscope image of the process for cleaving the capillary.

The short section of the capillary left on the SMF forms the open air-cavity at the fiber tip (see Fig. 5.7). With the assistance of a microscope and a high-precision translation stage, the length of the cavity can be controlled in the range from ten to several tens of micrometers.

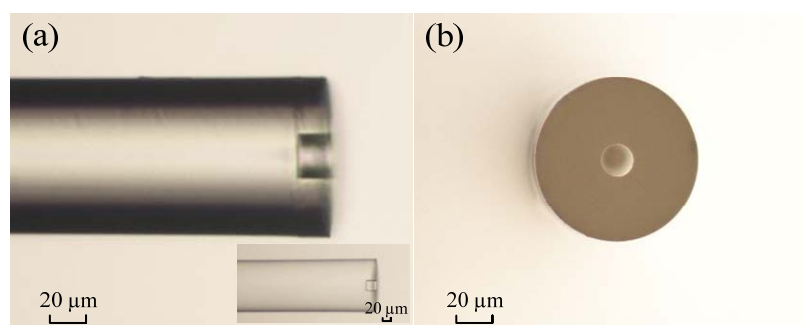


Fig. 5.7 Microscope images of (a) the fiber/capillary tip; (b) the cross-section of the tip endface; inset: fiber-tip immersed in the oil with a refractive index of 1.4.

The next step is to seal the micro-cavity at the SMF tip by a dip-coating process. As illustrated in Fig. 5.8, we start with a commercial graphene/Ni/SiO<sub>2</sub>/Si sample in which the FLG is grown on a Nickel (Ni) /SiO<sub>2</sub>/Si substrate by the CVD method (see Table 5.1). The transferring process is as follows,

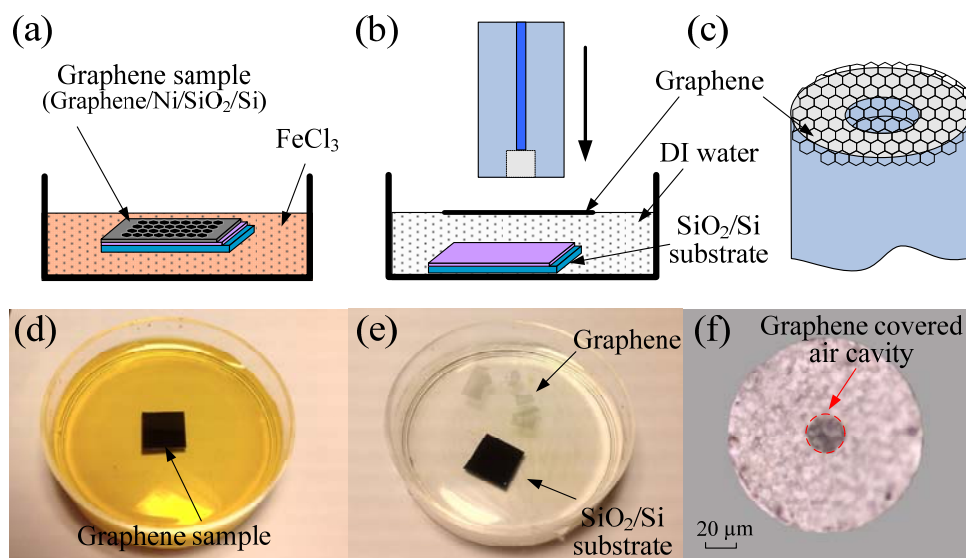


Fig. 5.8 Fabrication process of the fiber-tip micro-cavity with a graphene diaphragm. (a) Etching off the Ni layer by immersing the sample to a  $\text{FeCl}_3$  solution; (b) transferring graphene film floating on the water surface to the surface of fiber-tip open-cavity; (c) schematic showing the graphene film covering a fiber-tip micro-cavity. Photographs of (d) a graphene/Ni/SiO<sub>2</sub>/Si sample floating on the  $\text{FeCl}_3$  solution; (e) graphene films floating on DI water; (f) the micro-cavity with the graphene covered.

1) The metal film between the graphene and the substrate is etched off. The sample is immersed into a  $\text{FeCl}_3$  solution with a concentration of 0.05 g/mL (Fig. 5.8(a) and (d)). Before the Ni layer is completely etched off, which corresponds to the detachment of the graphene film from the SiO<sub>2</sub>/Si substrate, the sample is transferred to the DI water and left on the water for ~ 12 hours to remove the residual metal ions.

2) The graphene film is separated from the substrate. The sample is dipped into the clean DI water with a floating-off process to delaminate the graphene from the SiO<sub>2</sub>/Si substrate [13]. After being detached from the substrate, the graphene film will float on the water under the surface tension of water (Fig. 5.8(e)).

3) The graphene film is transferred onto the surface of the fiber-tip air-cavity. The fiber-tip with the open air-cavity is inserted into a ferrule with an inner diameter of 127  $\mu\text{m}$ . The endface of the fiber-tip is adjusted so that it is in the same plane with that of the ferrule under the microscope. The ferrule/fiber-tip assembly is then fixed to

keep its endface parallel to the water surface. Until it touches the graphene sample, the assembly is moved down slowly toward the floating graphene, as shown in Fig. 5.8(b). Finally, the graphene is attached to the surface of the assembly and is left to dry at room temperature in a cabinet for about half an hour.

In the process of drying, the water on the assembly end is drawn by the capillary force into the gap between the fiber and the ferrule. This might help to avoid the damage of the graphene by the water surface tension and prevent the sealing of the water into the air-cavity. After the water is evaporated, the graphene seals the air-cavity by the van der Waals interaction [14] as shown in Fig. 5.8(c). No additional splicing or adhesion process is required for the fabrication of the sensor. The microscope image of the sealed fiber-tip micro-cavity is shown in Fig. 5.8(f).

Fig. 5.9(a) shows a typical reflection spectrum of the FPI with the graphene diaphragm. From this interference spectrum, the cavity length  $d$  can be calculated to be  $\sim 21 \mu\text{m}$ , which agrees with the value measured by the microscope.

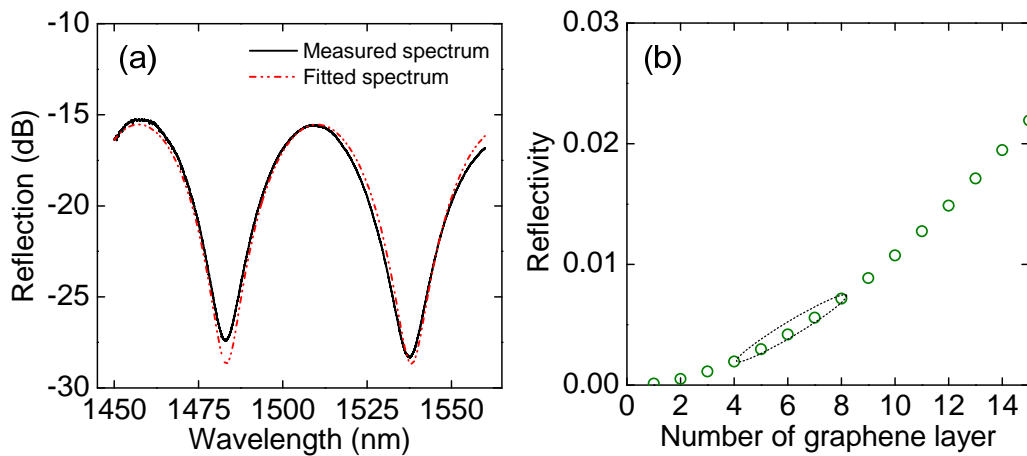


Fig. 5.9 (a) Measured and fitted reflection spectrums of the FPI; (b) calculated reflectivity as a function of the number of graphene layers at the wavelength of 1550 nm. The refractive index of the graphene used in the calculation is  $3.45 - 2.32i$  [15].

Since the reflectivity of the cleaved fiber end is known, the reflectivity of the graphene film can be determined by curving fitting the measured reflection spectrums of several fabricated samples. The fitted values of the graphene reflectivity vary

from 0.27% - 0.79% and are similar to those measured with an optical low-coherence reflectometer (OLCR). Compared to the calculated curve as shown in Fig. 5.9(b), the measured values of the graphene reflectivity correspond to a layer number varying from 4 – 8, as denoted by the dotted line. This variation might result from the uneven thickness of the graphene grown on the nickel film, which can be observed from the microscope image of the FLG (Fig. 5.2(b)). According to the datasheet, the thickness of the FLG varies from 1 to 7 and has an average layer number of 4.

As discussed in 2.11, the fringe visibility of the interference spectrum for the Fabry-Perot cavity reaches maximum when the two reflective mirrors have the same values of reflectivity. However, the FLG film has a reflectivity less than 1%, which is much smaller than that of a perfectly cut fiber end (~ 4%). To maximize the fringe visibility, the reflectivity of the fiber end is reduced by cutting the fiber with an appropriately tilted angle. Fig. 5.10 shows the reflectivity of the fiber end with various tilted angles.

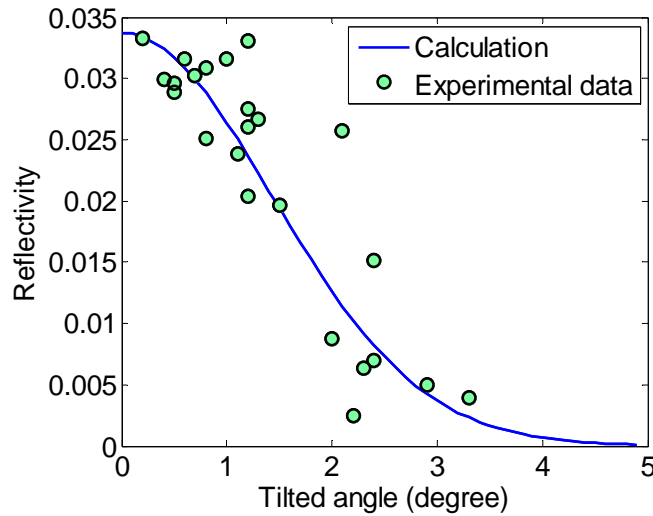


Fig. 5.10 Reflectivities of the SMF endface with different tilted angles at the wavelength of 1550 nm.

The reflectivity of the fiber end with a tilted angle  $\theta$  can be described by [16],

$$R(\theta) = R_0 \cdot \exp \left[ - \left( \frac{2\pi n_{core} \theta}{\lambda} \right)^2 \right] \quad (5.2)$$

where,  $R_\theta$  is the reflectivity of the perpendicularly cleaved fiber end,  $n_{core}$  is the refractive index of the fiber core, and  $\lambda$  is the wavelength of the light. In the experiment, the fiber ends with a tilted angle  $\sim 2$  degree, i.e., a reflectivity of  $\sim 1\%$  are selected to build the FPIs.

### 5.3.2 Pressure response

The wavelength shift  $\Delta\lambda$  of the interference fringe under different pressures is measured, and the cavity length change  $\Delta d$  which is equal to the diaphragm deflection  $\delta$ , can be calculated by the relationship  $\Delta d/d = \Delta\lambda/\lambda$ . As shown in Fig. 5.11, the cavity length decreases with the increasing external pressure and follows a non-linear curve. The average pressure sensitivity over the range from 0 to 5 kPa is estimated to be  $\sim 39.4$  nm/kPa.

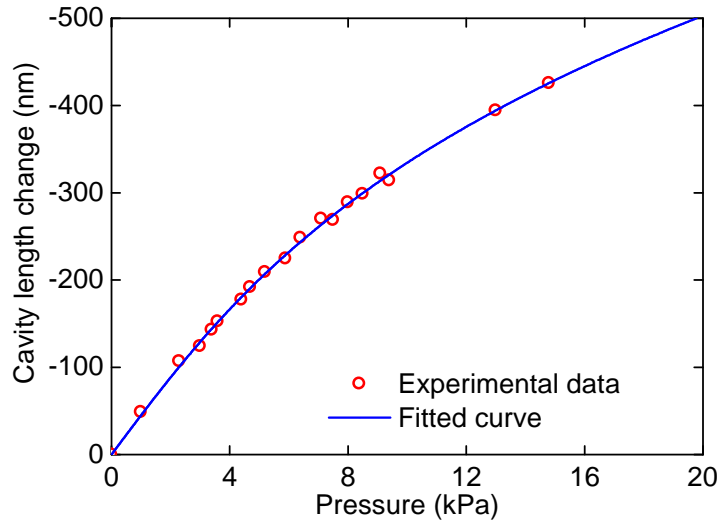


Fig. 5.11 Pressure response of the fiber-tip micro-cavity with the graphene film.

The deflection  $\delta$  of a circular membrane under the pressure change  $P$  can be described by,

$$P = \frac{2Et}{(1-\nu)a^4} \delta^3 + \frac{4\sigma_0 t}{a^2} \delta \quad (5.3)$$

where  $E$  and  $\nu$  are the Young's modulus and Poisson's ratio ( $\sim 0.17$ ) of the graphene, respectively.  $\sigma_0$  is the graphene film pre-stress, and  $a$  and  $t$  are the radius and the thickness of the graphene film, respectively. For graphene,  $E \sim 1$  Tpa and  $\nu \sim 0.17$ . By least-square curve fitting of the experimental data in Fig. 5.11, the thickness and the pre-stress of the graphene film is found to be  $\sim 0.71$  nm and  $\sim 1.2$  GPa. The thickness corresponds to a 2-layer graphene and the pre-stress is within the range measured by the AFM-tip method which indicates a broad range of pre-stresses varying from 0.2 to 2.2 GPa [6]. This pre-stress might result from the stretching of the graphene caused by the strong van der Waals interaction between the graphene and the inner wall of the cavity.

It should be noted that the graphene sealed cavity is found to be slightly leaky during the pressure tests. Fig. 5.12 shows the measured cavity length change as a function of time when a pressure of  $\sim 13$  kPa is applied at time  $T=0$  and released at  $T \sim 30$  min by opening the pressure chamber.

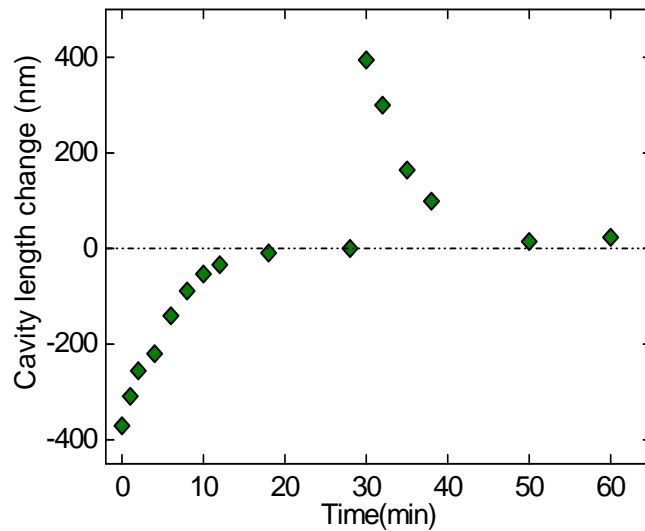


Fig. 5.12 Cavity length change vs time for an initially applied pressure of  $\sim 13$  kPa.

When the pressure is applied at  $T=0$ , the graphene diaphragm deflects inward since the external pressure is higher than that inside the micro-cavity. The deflection

of the graphene gradually reduces and returns to initial state (zero deflection), indicating that the cavity is leaking and the time to achieve the pressure equilibrium is about 20 min. When the applied pressure is released, the graphene diaphragm deflects in the opposite direction instantly, and the deflection reduces gradually and returns to the equilibrium again after  $\sim 20$  min. As reported in [17], the graphene itself is impermeable to all standard gases, and the leakage might be attributed to the imperfect sealing at the graphene/capillary interface.

To alleviate the measurement error induced by this leakage problem in the continuous test of the sensor under static pressure, our measurement of the pressure response was conducted by applying a target pressure, recording the spectrum and releasing the pressure, with all these steps completed within the duration of only several seconds. The pressure response shown in Fig. 5.11 was obtained by repeating this process with different applied pressures.

Several fiber-tip micro-cavities were constructed and their pressure sensitivities range from 36 to 63 nm/kPa over the pressure range of 0 - 5 kPa. By fitting the pressure response curves by Eq. (5.3), the pre-stress and the thickness of different graphene based fiber-tip micro-cavities were obtained and are shown in Fig. 5.13. The pre-stress varies from 1 to 2.1 GPa, within the previously reported range [6]. The graphene thickness ranges from 0.26 to 1.1 nm, corresponding to a layer number of 1 to 3.

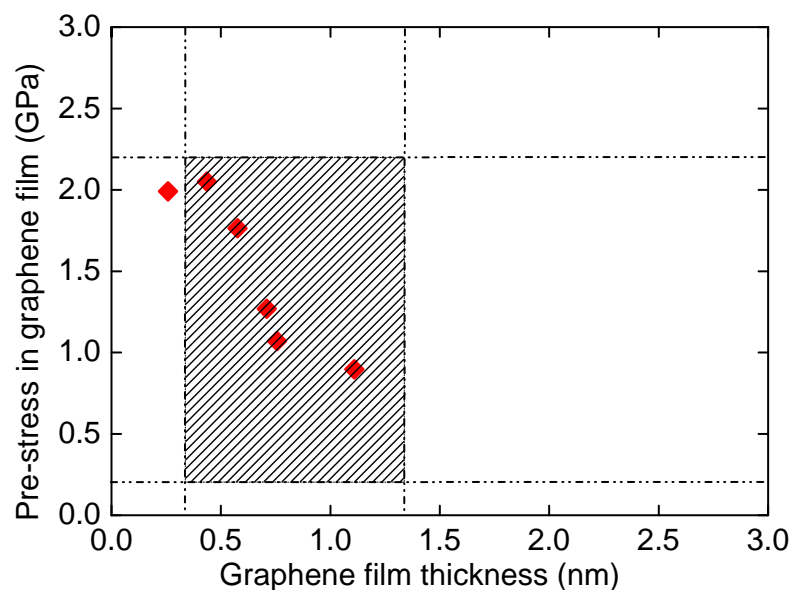


Fig. 5.13 Fitted pre-stress and thickness of the graphene film from the measured pressure response of several fiber-tip micro-cavity sensors.

As we mentioned previously, the micro-cavity is not perfectly sealed by the graphene and shows leakage phenomenon. To improve the sealing of the cavity, the endface of the capillary is smoothed by the electric arc discharge before being covered by the graphene film. The fusion current and time used are, respectively 10.5 mA and 0.3 s. The microscope images and the AFM images for the endface of the cleaved capillary before and after the smoothing treatment are shown in Fig. 5.14 and Fig. 5.15, respectively.

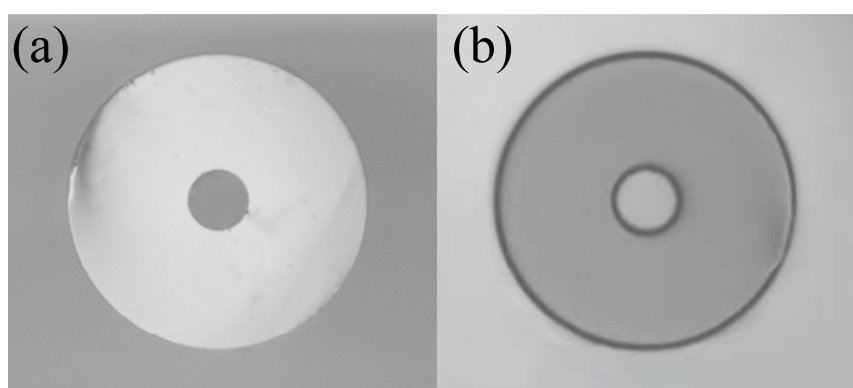


Fig. 5.14 The microscope images of the cross-section of the capillary before (a) and after (b) the smoothing treatment.

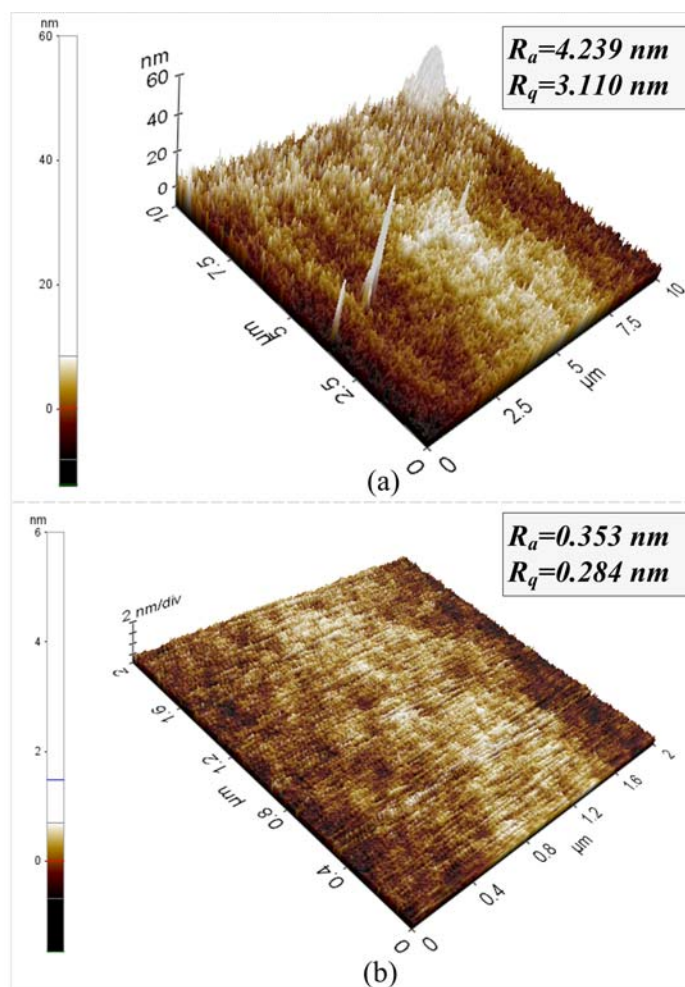


Fig. 5.15 AFM images of the capillary end surface (a) before and (b) after smoothing treatment.  $R_a$  and  $R_q$  are the average roughness and the root mean square roughness, respectively.

The average roughness ( $R_a$ ) for the capillary surface is reduced from 4.24 nm to 0.353 nm which might provide a firmer attachment of the graphene to the endface of the capillary [14]. The pressure response of the graphene-sealed micro-cavity after the smoothing treatment is tested and the leakage phenomenon is significantly alleviated without observable spectrum shift for the constant pressure applied. The interference spectrum shift and the cavity length change of the sensor to the increase of the pressure are shown in Fig. 5.16(a) and Fig. 5.16(b), respectively. The sensor exhibits a similar pressure response to that of the leaky samples as we tested previously.

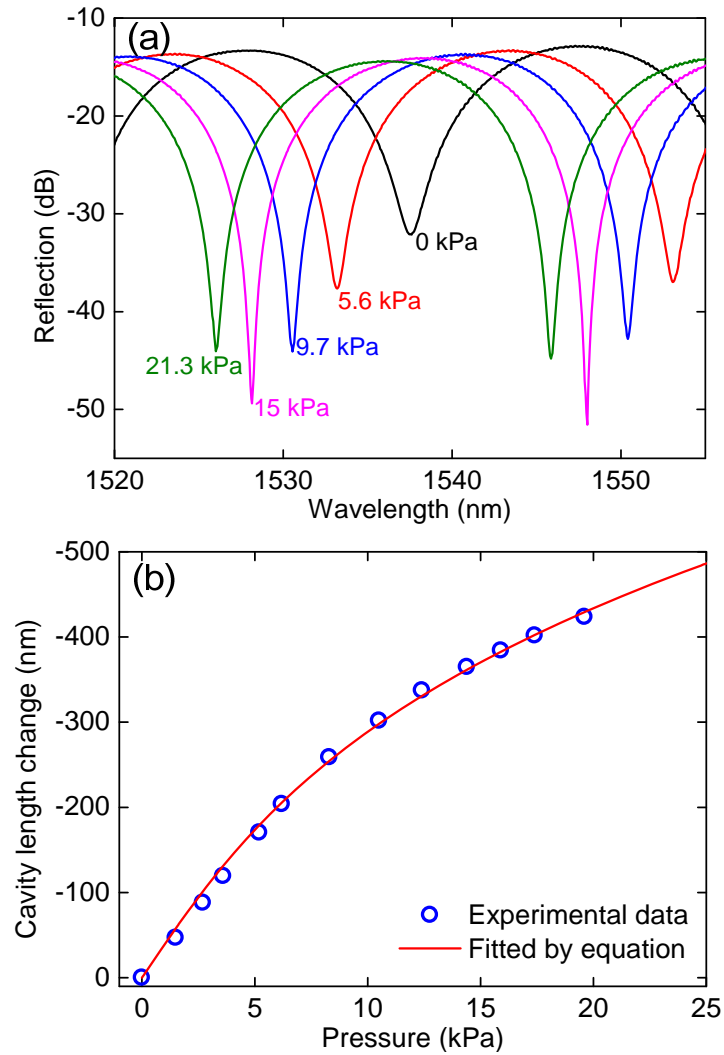


Fig. 5.16 (a) Reflection spectra of the FPI at different pressures; (b) the cavity length change as a function of the applied pressure.

Fig. 5.17 shows the pressure response of the sensor in the pressure up and down cycle. The discrepancy between the two curves indicates an unsatisfactory repeatability, which might result from the hysteresis or non-uniform thickness (defects) of the graphene film. The defects could also deteriorate the mechanical strength of the graphene film although the pristine graphene can withstand pressure up to 2.5 MPa without being broken [14]. For an applied pressure of  $\sim 100$  kPa in the experiment, the sensor shows a very unstable behavior, which is reflected by a continuous drift of the spectrum and a fast leakage. This instability prevents the

determination of the break-down pressure and detailed study is necessary for practical pressure sensing applications.

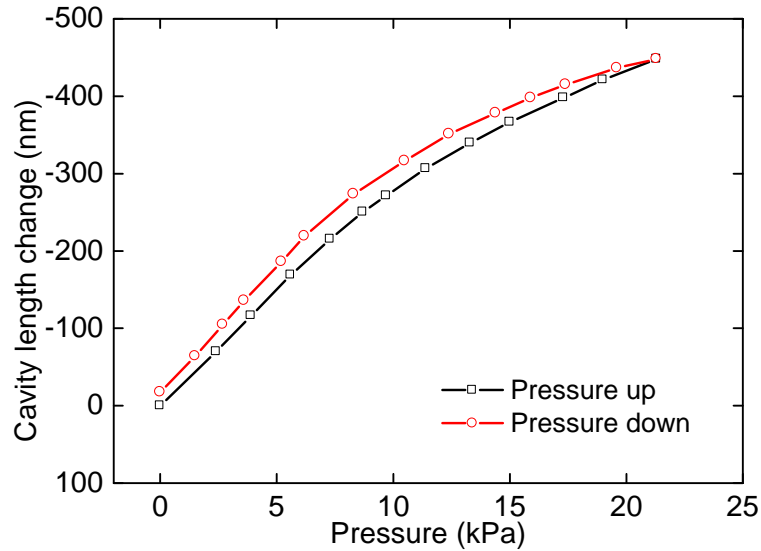


Fig. 5.17 Cavity length change of the FPI during the pressure up and down cycle.

### 5.3.3 Temperature response

The average temperature response of the sensor from 25 to 40 °C is measured and the sensor demonstrates a temperature sensitivity of  $\sim 70 \text{ nm}/^\circ\text{C}$ , as shown in Fig. 5.18. This large temperature sensitivity of the sensor might result from two factors: the pressure change of the air trapped in the cavity and the thermal expansion of the silica wall of the cavity. As indicated by the calculated values in Fig. 5.18, the latter factor makes a negligible contribution to the large temperature sensitivity of the sensor. This has been confirmed experimentally by testing the temperature response of a leaky sensor sample, for which the effect of the pressure change of the air in the cavity could be excluded. As expected, no obvious cavity change of the sample was observed when the sample was heated up and cooled down.

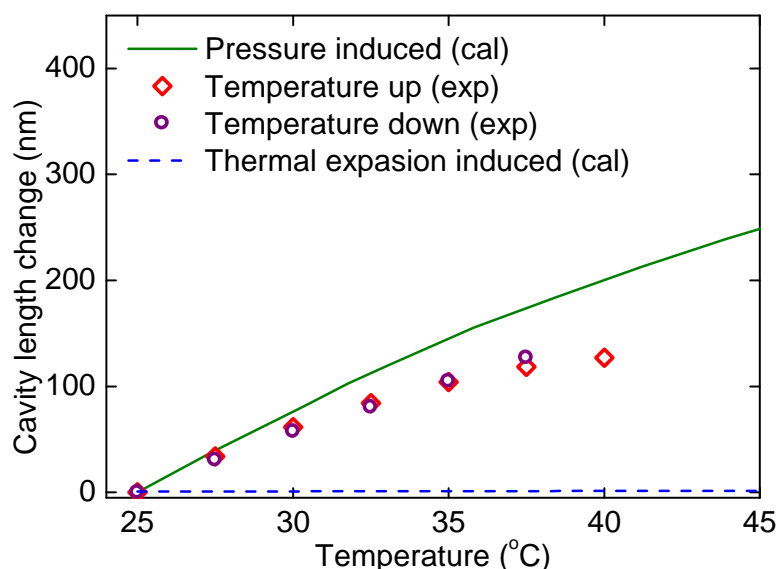


Fig. 5.18 Temperature response of the FPI sensor. Green curve: the calculated cavity length change induced by the pressure change of the air in the cavity; blue curve: the calculated cavity length change induced by the thermal expansion of the cavity; dots: the experimental results for the cavity length change in the temperature up and down cycle.

## 5.4 Ferrule-top FPI with the multi-layer graphene diaphragm

By using the SLG film with the diameter of only 25  $\mu\text{m}$  as the deflectable diaphragm, the fiber-tip FPI demonstrates a pressure sensitivity of  $\sim 39.4$  nm/kPa. Increasing the diameter of the diaphragm can further improve the pressure sensitivity of the sensor, but it is found difficult to prepare and transfer a larger graphene film with a nanometer thickness to the fiber-tip. During the transferring, the suspended graphene film is easily broken by the surface tension of the water during the evaporation of the water lying between the graphene and the fiber end. Therefore, to further increase the pressure sensitivity of the FPI sensor, a 125  $\mu\text{m}$ -diameter multi-layer graphene (MLG) diaphragm with a thickness of  $\sim 100$  nm is used to build the FPI pressure sensor. The MLG is strong enough to withstand the transferring process without being damaged.

### 5.4.1 Sensor fabrication and interrogation

Fig. 5.19(a) is the schematic of the ferrule-top MLG FPI. The structure comprises a piece of SMF, a zirconia ferrule and a MLG diaphragm.

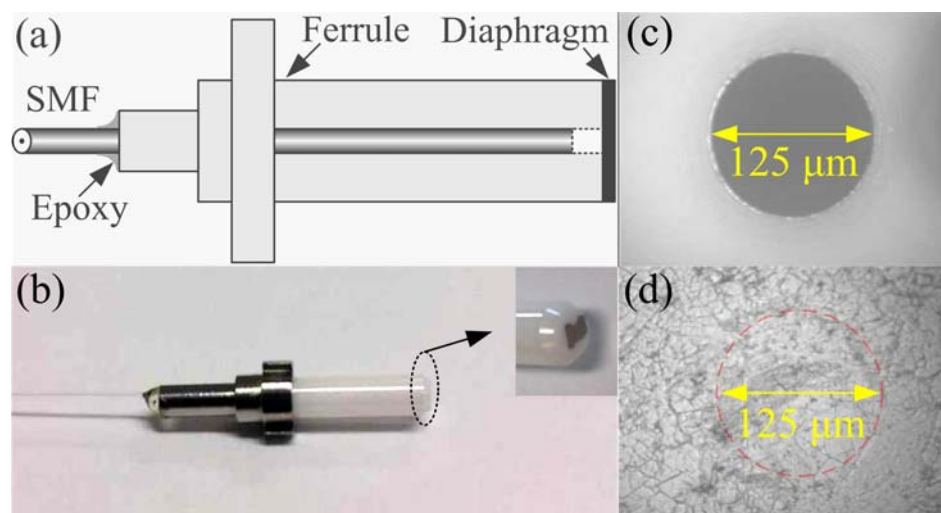


Fig. 5.19 (a) Schematic of the FPI configuration: a 125  $\mu\text{m}$ -diameter zirconia ferrule with a SMF inserted into it and a graphene diaphragm covering its endface; (b) photograph of the fabricated FPI; microscope images of the ferrule endface (c) before and (d) after it is covered with the graphene diaphragm.

The fabrication process of this sensor is described as follows: firstly, the SMF is cleaved and inserted into the ferrule (the inner diameter  $\sim 125 \mu\text{m}$ ), and the separation between the fiber end and the ferrule endface is controlled by a translation stage. The ferrule and the SMF are held together by using a curable gel; secondly, the MLG diaphragm is transferred to the ferrule endface. The MLG diaphragm is prepared from the graphene/Ni/graphene film (see Table 5.1) in which the 100 nm-thick MLG is grown by the CVD method on a 25  $\mu\text{m}$ -thick Ni foil. The process of separating the MLG from the Ni foil and transferring it to the ferrule endface is similar to the process for the fabrication of the FLG based fiber-tip FPI. The difference is that the MLG on one side of the graphene/Ni/graphene sample is polished off before the sample is immersed into the  $\text{FeCl}_3$  solution to etch the Ni foil off. During the etching

process, the unpolished side is kept face up.

Fig. 5.19(b) shows a photograph of the FPI sensor head, and Fig. 5.19(c) and (d) show respectively the microscope images of the ferrule endface before and after being covered with the graphene diaphragm. The graphene diaphragm is stuck to the ferrule endface by the van der Waals interaction [18].

Fig. 5.20 shows a typical interference spectrum of the FPI measured by a broadband source (BBS) in combination with an optical spectrum analyzer (OSA). From the interference spectrum, the cavity length of the FPI can be calculated by  $L = \lambda_1 \lambda_2 / 2(\lambda_1 - \lambda_2)$ , where  $\lambda_1$  and  $\lambda_2$  are the adjacent peak/dip wavelengths of the interference spectrum. The interference fringe visibility reaches up to ~10 dB, which is determined by the reflectivities of the fiber end and the graphene diaphragm. The reflectivity of the cleaved fiber end before being inserted into the ferrule is measured to be 3.0%. The reflectivity of the graphene film is determined by curve fitting the interference spectrum since the reflectivity of the fiber end and the length of the cavity are already known.

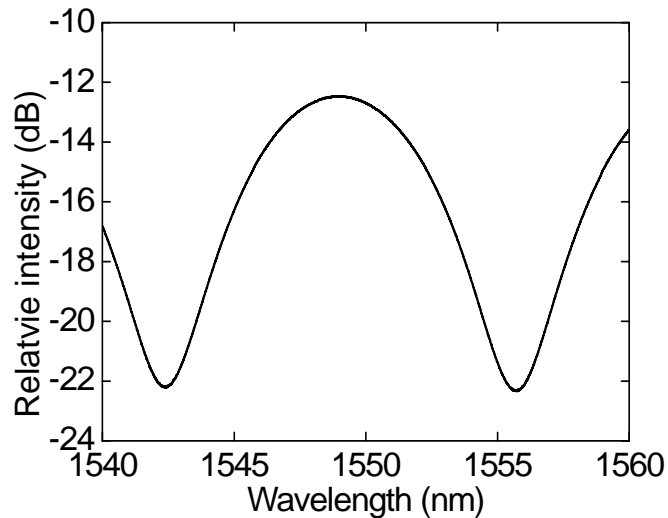


Fig. 5.20 Interference spectrum of the multi-layer graphene diaphragm based FPI.

Fig. 5.21(a) shows the measured interference spectrums of FPIs with different cavity lengths when the fiber end is moved towards the diaphragm by a translation

stage. During the fabrication of this sample, the SMF is not tightly fixed in the ferrule on purpose.

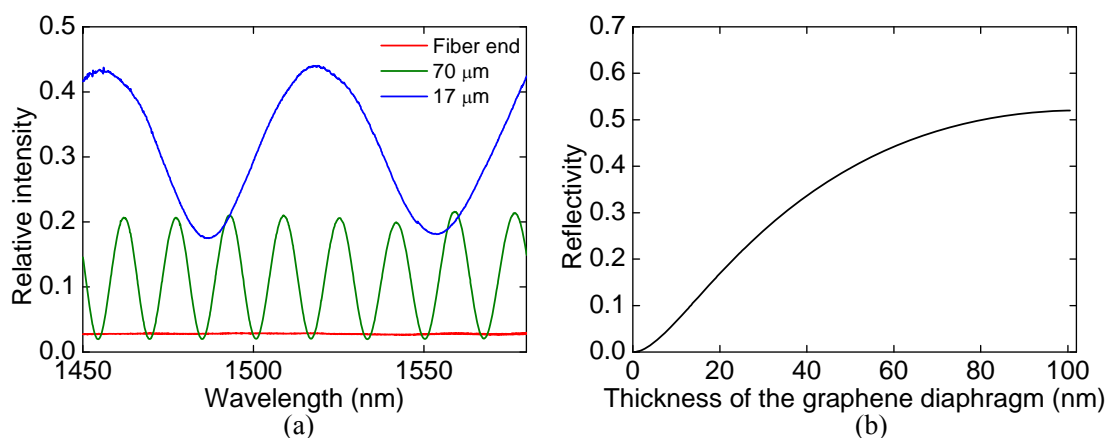


Fig. 5.21 (a) Measured reflection spectrums of FPI with different cavity lengths; (b) calculated reflectivity of graphene diaphragm at 1550 nm as a function of its thickness. The complex refractive index of graphene is assumed to be  $3.45-2.32i$  [15].

When the fiber is far from the diaphragm, the reflection from the fiber end shows no change before and after being inserted into the ferrule as indicated by the red line. As the fiber end is sufficiently close to the diaphragm surface, the interference fringes are observed (green and blue lines) and the fringe spacing increases when the fiber end moves closer to the diaphragm, as shown in Fig. 5.21(a). The average intensity of the reflected light also increases since more light reflected from the diaphragm is coupled back into the SMF. It has been shown that most of the light reflected from the diaphragm ( $\sim 90\%$ ) is coupled back to SMF when the cavity length is reduced down to  $17\ \mu\text{m}$  [19]. By curve fitting the interference spectrum, the reflectivity of the graphene diaphragm is determined to be  $\sim 31\%$ . This value is smaller than the theoretical reflectivity (Fig. 5.21(b)) which is similar to the reflectivity of graphite as reported in [20]. The smaller reflectivity measured might result from the deformation of the diaphragm. As shown in Fig. 5.19 (d), the diaphragm transferred onto the ferrule endface is not perfectly flat, which might

reduce the light level being coupled back into the SMF as well as the pressure sensitivity which we will discuss later.

### 5.4.2 Response to acoustic pressure

As pointed out in Chapter 3, for an edge fixed circular plate, the deflection  $\Delta L$  at the center of the diaphragm to the pressure  $\Delta P$  may be expressed as,

$$\Delta L = \frac{3(1-\nu^2)D^4}{256Et^3} \Delta P \quad (5.4)$$

where  $D$  and  $t$  are respectively the diameter and the thickness, and  $\nu$  and  $E$  are the Poisson ratio and Young's modulus of the diaphragm, respectively. For graphene,  $\nu = 0.17$ ,  $E = 1$  TPa. For a diaphragm with the thickness  $t = 100$  nm and the diameter  $D = 125$   $\mu\text{m}$ , the pressure sensitivity (pressure-induced deflection) is calculated to be 2.86 nm/Pa. However, for static pressure measurement, the sensor shows a quick leakage to the applied pressure due to the weak Van der Waals interaction between the ferrule endface and the MLG.

To measure the static pressure sensitivity of the sensor, sealing of the cavity has been attempted by the following steps: firstly, a thin layer epoxy is spin-coated onto the ferrule endface and the graphene/Ni/graphene film is flattened by being pressed between two clean glass slides. Then the graphene/Ni/graphene sample is transferred onto the ferrule endface with the epoxy. After the epoxy is solidified, the graphene/Ni/graphene sample is bonded to the ferrule endface and is polished lightly to remove the graphene on the upside of the graphene/Ni/graphene film. Finally, the ferrule with the graphene/Ni film is immersed into the  $\text{FeCl}_3$  solution to remove the Ni film and only the graphene is left which covers the air-hole of the ferrule endface. The leakage problem has been significantly improved while the pressure sensitivity is found to be limited at the range from several to several tens nm/kPa. Compared to the value calculated from Eq. (5.4), the pressure sensitivity is much lower, which

might be due to the wavy surface/wrinkles of the suspended MLG induced during the transfer process as observed by the microscope.

For dynamic (or acoustic) pressure test, the leakage problem might introduce slightly or no error to the measurement. On the other hand, the leakage problem might alleviate the influence of the pressure fluctuations in the environment on the working stability of the sensor. Fig. 5.22 shows the experimental setup for testing the acoustic response of the ferrule-top MLG based FPI with the interference spectrum shown in Fig. 5.20.

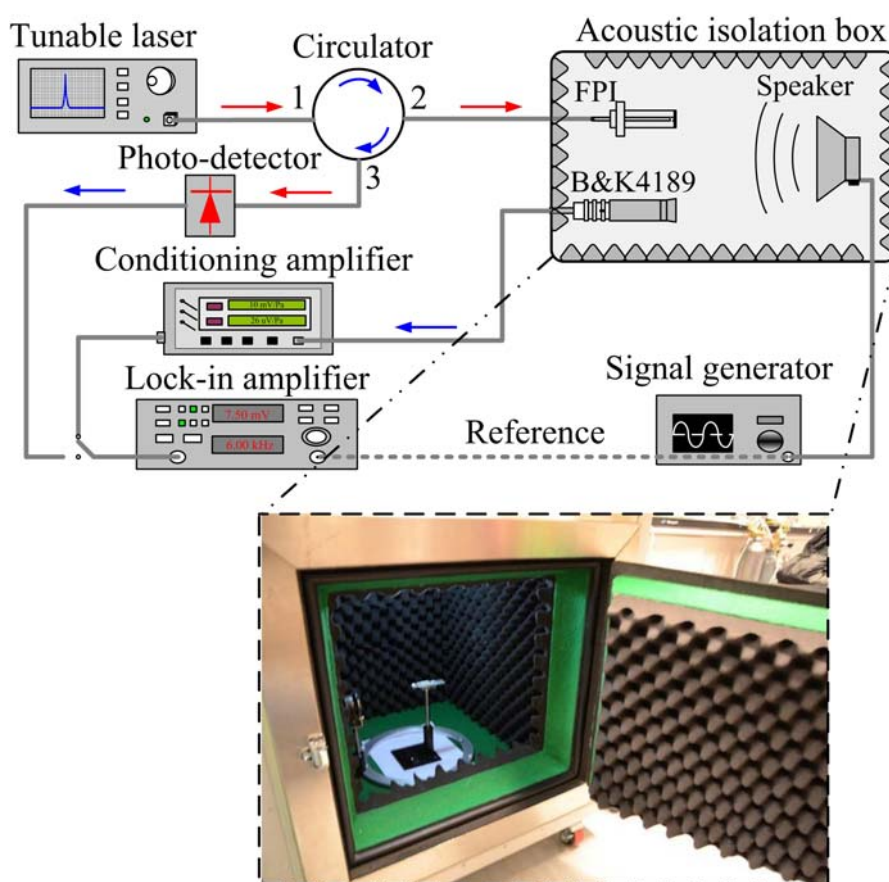


Fig. 5.22 (a) Schematic of the experimental setup for the acoustic pressure measurement; (b) photograph of the acoustic isolation box.

The FPI and a calibrated microphone (B&K4189) are positioned at two symmetry points to the central axis of the speaker which is driven by a signal generator. The working wavelength of the tunable laser is tuned to the Q point of the interference

spectrum of the FPI to achieve a linear response and to maximize the sensitivity [21]. The light reflected from the FPI travels through an optical circulator and is detected by a photo-detector (PD). The calibrated microphone is connected with a conditioning amplifier. The electrical outputs from the PD and the conditioning amplifier are received by either a lock-in amplifier (SR830, Stanford research systems) or a real-time electrical spectrum analyzer (RSA3303, Tektronix). During the acoustic test, the FPI sensor, the microphone and the speaker are placed inside an acoustic isolation box. Fig. 5.23(a) shows the output signal of the FPI for different acoustic pressure levels at a frequency of 10 kHz. The acoustic pressure sensitivity, i.e., the slope of the curve of the FPI, is estimated to be 13.2 mV/Pa. The time constant and roll off of lock-in amplifier in the test are set to 100 ms and 18 dB/octave. Under the approximation of two-beam interference, the output voltage  $V_{ac}$  can be related to the pressure induced deflection of the diaphragm by,

$$V_{ac} = \mathfrak{R} \cdot I_0 \cdot S_{\max} \cdot \Delta L \quad (5.5)$$

where,  $\mathfrak{R}$  is the responsibility of the PD,  $I_0$  is the laser power at the Q-point.

$$S_{\max} = \frac{d(I/I_0)}{dL} = 2\sqrt{R_1 R_2} \cdot \frac{4\pi n}{\lambda} \quad (5.6)$$

is the slope of the normalized intensity change to the deflection of the diaphragm. In our experiment,  $I_0 = 0.8$  mW and  $\mathfrak{R} = 10^5$  V/W.  $R_1$  and  $R_2$  are the reflectivities of the fiber end/air interface and the graphene diaphragm, and can be determined to be respectively 1.7% and 0.5% by curve fitting the interference spectrum in Fig. 5.20. The smaller values of reflectivity for the sample may result from the imperfect cleaving of the fiber end and the transmission loss for the light propagating forward and backward through the air cavity of the FPI. The slope  $S_{\max}$  can then be calculated by Eq. (5.6) to be  $0.15 \times 10^{-3}/\text{nm}$ , which is similar to that directly estimated from the interference spectrum in Fig. 5.20. Combined with Eq. (5.4), the pressure sensitivity of the FPI to acoustic pressure is calculated to be 1.1 nm/Pa.

This result is lower than the calculated value by Eq. (5.4). As mentioned previously, the pressure sensitivity of the MLG diaphragm is significantly affected by the deformation/stress introduced to the diaphragm during the graphene transfer process, and further investigation is needed to improve this problem [22].

The sensor exhibits a relatively uniform response over the frequency range from 0.2 kHz to 22 kHz as shown in Fig. 5.23(b).

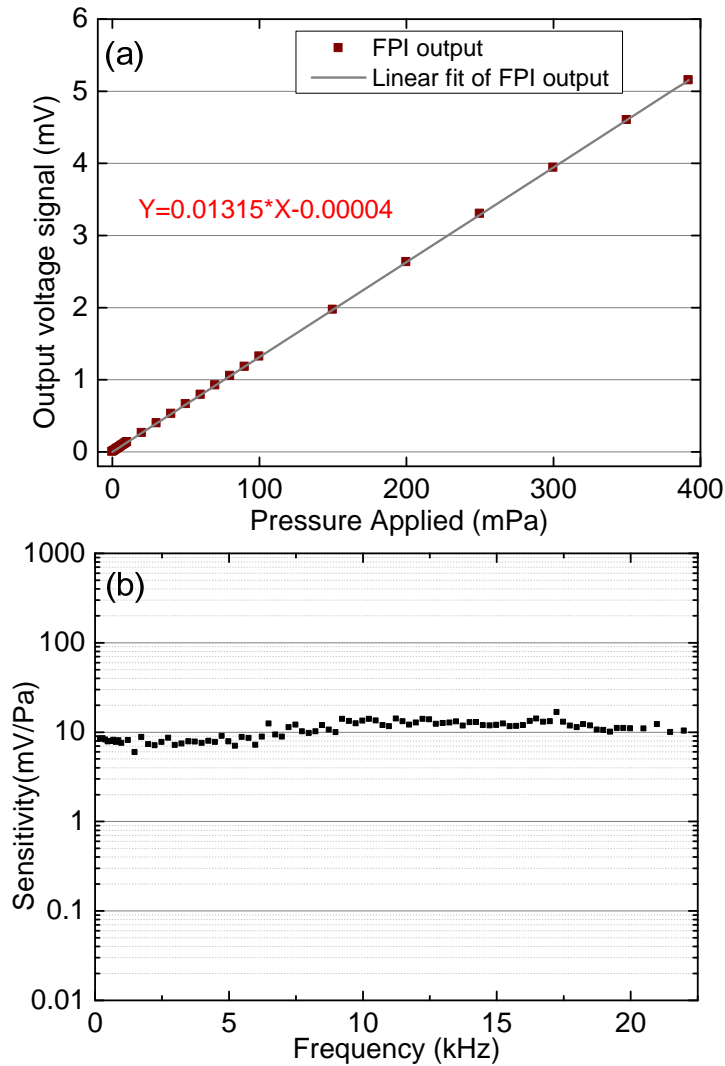


Fig. 5.23 (a) Output voltage signal of the FPI for varying applied acoustic pressure levels at the frequency of 10 kHz; (b) frequency response of the FPI.

The small ripples observed might be caused by the interference of the incident acoustic wave and the reflected acoustic waves from the FPI and the microphone [23]. If we assume the graphene diaphragm as a clamped circular plate, its fundamental resonance frequency  $f_{00}$  can be described as follows [21],

$$f_{00} = \frac{10.21t}{2\pi r^2} \sqrt{\frac{E}{12\rho(1-\nu^2)}} \quad (5.7)$$

For the graphene diaphragm with the mass density  $\rho=2.2\times 10^3$  kg/m<sup>3</sup>, the thickness  $t=100$  nm and the radius  $r=62.5$   $\mu$ m, its theoretical resonant frequency is 259.8 kHz. The value is significantly higher than our tested frequency range which is limited by the maximum frequency of the speaker.

It is needed to point out that the pressure sensitivity and the resonant frequency of the MLG diaphragm calculated by the ideal elastic plate model, as denoted by the Eq. (5.4) and (5.7) here, is simply a rough estimate. The effects of the pre-stress in the diaphragm are ignored due to the difficulty in directly measuring the pre-stress in the suspended MLG on the ferrule enface.

To measure the resonant frequency of the diaphragm, thermal excitation by using a modulated laser is an alternative [24]. Fig. 5.24(a) shows the power spectrum of the FPI output under an acoustic pressure with a magnitude of 400 mPa and a frequency of 10 kHz, which was measured by the real-time electrical spectrum analyzer. For the noise floor of  $\sim -91$  dBm with a bandwidth of 50 Hz, the signal to noise ratio (SNR) of the FPI output can be calculated to be  $\sim 57.5$  dB, which corresponds to a noise-limited minimum detectable pressure (MDP) level of  $75 \mu\text{Pa}/\text{Hz}^{1/2}$ . The noise performance of the FPI sensor was further examined by a lock-in amplifier. Fig. 5.24(b) presents the outputs from the lock-in amplifier for different pressure levels at 10 kHz. The output voltage of the FPI for a pressure  $\sim 2$  mPa is 37  $\mu$ V and the standard derivation of the noise without acoustic signal is 1.1  $\mu$ V. The minimum detectable pressure can then

be calculated to be  $59.5 \mu\text{Pa}/\text{Hz}^{1/2}$ , which is similar to the value estimated from Fig. 5.24(a).

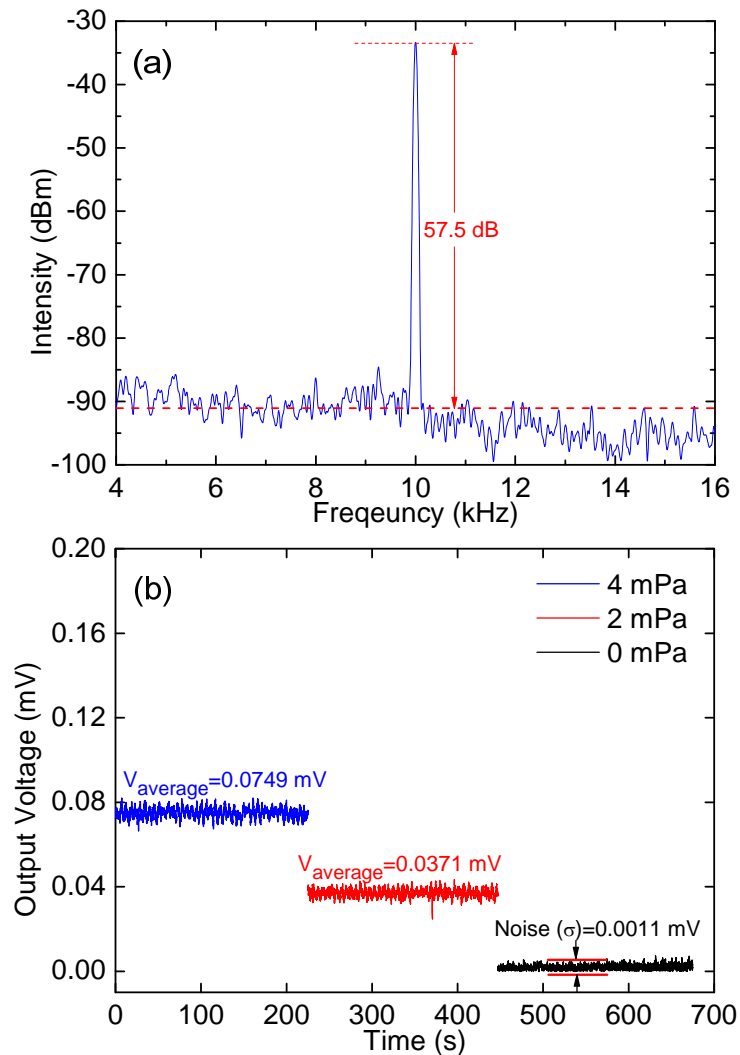


Fig. 5.24 (a) Power spectrum of the FPI output under an acoustic pressure level of 400 mPa at 10 kHz; (b) output voltages of the FPI for acoustic pressures of 0 mPa, 2 mPa and 4 mPa at 10 kHz.

It should be pointed out that the sensor head was aligned to the central axis of the speaker to achieve the maximum acoustic sensitivity during the acoustic test. To account for the sensitivity penalty induced by the alignment angle, the directivity of the sensor was investigated and the result is illustrated in Fig. 5.25.

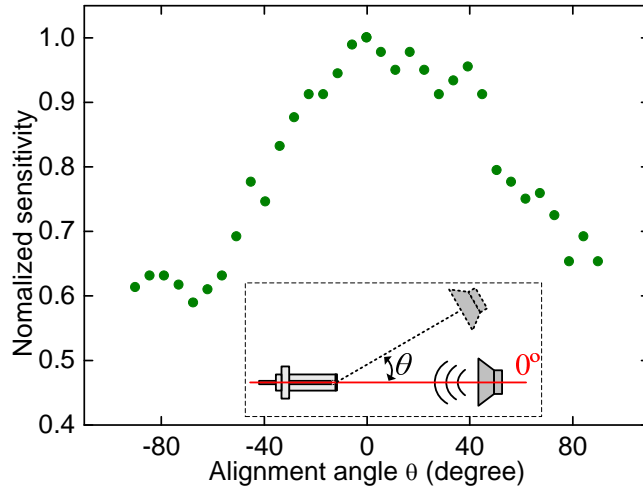


Fig. 5.25 Normalized acoustic sensitivity of the FPI with different alignment angles at the acoustic frequency of 10 kHz. Inset: schematic showing the alignment angle between the sensor head and the speaker.

### 5.4.3 Noise analysis

Fig. 5.26 shows the frequency spectrums of the FPI sensor in the Q-point demodulation system with the laser output power is off, the laser power is -25 dBm and the laser power is -20 dBm.

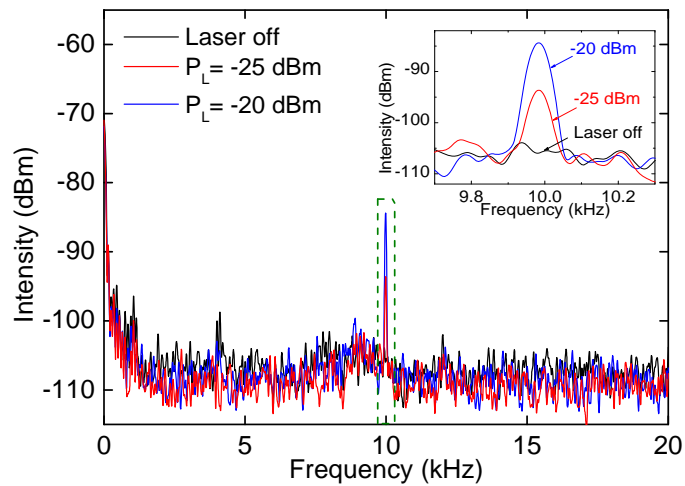


Fig. 5.26 Noise spectrums of the FPI sensor when the laser is off, the laser power is -25 dBm and the laser power is -20 dBm.

The curve with the laser off (black) represents the electrical noise from the electronics in the demodulation system. The noise spectrum shows nearly no change

when the incident laser power increases from -20 dBm to -25 dBm. At this low laser power, the noise mainly arises from the electrical noise instead of the shot noise. Consequently, a larger SNR as well as a smaller minimum detectable signal can be achieved by increasing the incident power of the laser. When the output power of the laser increases up to -10 dBm, the total noise exceeds the electrical noise. This indicates that the shot noise is necessary to be considered (see Fig. 5.27). The shot noise current can be expressed as,

$$i_{shot} \sim \sqrt{I_0} \quad (5.8)$$

and the signal current can be described by,

$$i_{signal} \sim I_0 \quad (5.9)$$

Accordingly, an increase of 10 dB in the incident power of the laser leads to an increase of 5 dB in the SNR. This is larger than the experimental result as shown in Fig. 5.27. An increase of SNR of  $\sim 3.5$  dB is observed when the output power of the laser increases from -10 dBm to 0 dBm. The smaller value may be caused by the increased thermal and/or RIN noise [25].

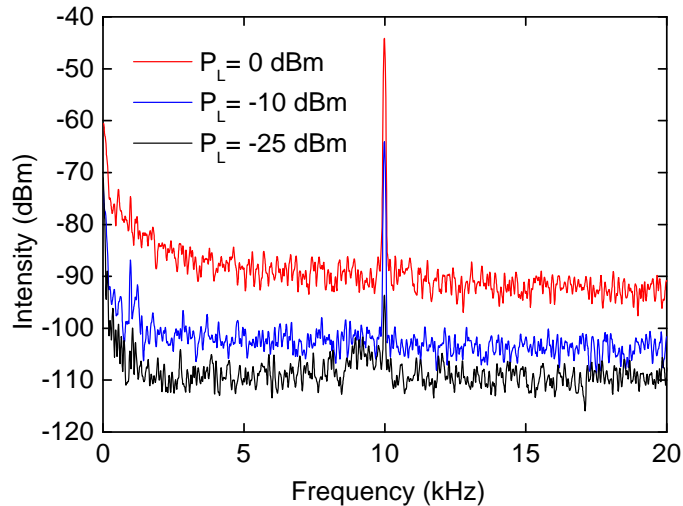


Fig. 5.27 Power spectra of the FPI sensor in the Q-point demodulation system when the output power of the laser is -25 dBm, -10 dBm and 0 dBm.

## 5.5 Summary

In this chapter, we have demonstrated two types of the diaphragm based pressure sensors. The first type is a fiber-tip FPI with the few-layer graphene which achieves a high sensitivity of  $\sim 40$  nm/kPa with a diaphragm of only 25  $\mu\text{m}$  in diameter. The nanometer-thick diaphragm stands for the ultimate limit for two-dimensional diaphragm-based pressure sensors, and the pressure sensitivity of this ultra-thin diaphragm is found to be limited by the pre-stress in the diaphragm instead of its thickness. The second type is the ferrule-top FPI with a multi-layer graphene which presents a high acoustic pressure sensitivity up to 1100 nm/kPa and a relative uniform response over the frequency range from 0.2 kHz to 22 kHz. The graphene film, used as a new type of diaphragms, allows the design of miniature and high-sensitivity fiber-tip pressure/acoustic sensors.

However, before the use of the sensor for field pressure measurements, several problems need to be solved. The first one is the optimization of the fabrication process which affects the amount of the pre-stress induced in the diaphragm since the pre-stress significantly affects the pressure sensitivity and linear working range of the sensor. The second one is the systematic characterization of the repeatability and stability of these thin diaphragm based pressure sensors, as the repeatability and stability of the sensors are experimentally found to exhibit high dependence on the maximum applied pressure and the temperature variation.

## References for Chapter 5

- [1] M. D. Giovanni, "Flat and Corrugated Diaphragm Design Handbook," Marcel Dekker (1982).
- [2] D. Donlagic and E. Cibula, "All-fiber high-sensitivity pressure sensor with SiO<sub>2</sub> diaphragm," *Opt. Lett.* 30, 2071-2073 (2005).
- [3] Y. Zhu, K. L. Cooper, G. R. Pickrell, and A. Wang, "High-temperature

- fiber-tip pressure sensor,” *J. Lightwave Technol.* 24, 861-869 (2006).
- [4] W. Wang, N. Wu, Y. Tian, C. Niezrecki, and X. Wang, “Miniature all-silica optical fiber pressure sensor with an ultrathin uniform diaphragm,” *Opt. Express* 18, 9006-9014 (2010).
- [5] F. Xu, D. Ren, X. Shi, C. Li, W. Lu, L. Lu, L. Lu, and B. Yu, “High-sensitivity Fabry-Perot interferometric pressure sensor based on a nanothick silver diaphragm,” *Opt. Lett.* 37, 133-135 (2012).
- [6] C. Lee, X. Wei, J. W. Kysar, and J. Hone, “Measurement of the elastic properties and intrinsic strength of monolayer graphene,” *Science* 321, 385-388 (2008).
- [7] M. S. Goh and M. Pumera, “Single-, few-, and multilayer graphene not exhibiting significant advantages over graphite microparticles in electroanalysis,” *Anal. Chem.* 82, 8367-8370 (2010).
- [8] A. K. Geim and K. S. Novoselov, “The rise of graphene,” *Nat. Mater.* 6, 183-191 (2007).
- [9] A. C. Ferrari, J. C. Meyer, V. Scardaci, C. Casiraghi, M. Lazzeri, F. Mauri, S. Piscanec, D. Jiang, K. S. Novoselov, S. Roth, and A. K. Geim, “Raman spectrum of graphene and graphene layers,” *Phys. Rev. Lett.* 97, 187401 (2006).
- [10] D. Nezich, A. Reina, and J. Kong, “Electrical characterization of graphene synthesized by chemical vapor deposition using Ni substrate,” *Nanotechnology* 23, 015701 (2012).
- [11] A. N. Obraztsov, E. A. Obraztsova, A. V. Tyurnina, and A. A. Zolotukhin, “Chemical vapor deposition of thin graphite films of nanometer thickness,” *Carbon* 45, 2017-2021 (2007).
- [12] Z. Ni, Y. Wang, T. Yu, and Z. Shen, “Raman Spectroscopy and Imaging of Graphene,” *Nano Res.* 1, 273-291 (2008).
- [13] Q. L. Bao, H. Zhang, Y. Wang, Z. H. Ni, Y. L. Yan, Z. X. Shen, K. P. Loh, and D. Y. Tang, “Atomic-Layer Graphene as a Saturable Absorber for Ultrafast Pulsed Lasers,” *Adv. Funct. Mater.* 19, 3077-3083 (2009).
- [14] S. P. Koenig, N. G. Boddeti, M. L. Dunn, J. S. Bunch, “Ultra-strong Adhesion of Graphene Membranes,” *Nat. Nanotechnol.* 6, 543-546 (2011).
- [15] F. J. Nelson, V. K. Kamineni, T. Zhang, E. S. Comfort, J. U. Lee, and A. C. Diebold, “Optical properties of large-area polycrystalline chemical vapor deposited graphene by spectroscopic ellipsometry,” *Appl. Phys. Lett.* 97, 253110 (2010).
- [16] K. Y. Lee and W. J. Parzygnat, “Low-reflection, single-mode multifiber array connector (MAC),” in *Proceedings of Electronic Components Conference (Bellcore, Piscataway, N. J., 1989)*, pp. 362–364.
- [17] J. S. Bunch, S. S. Verbridge, J. S. Alden, A. M. Van Der Zande, J. M. Parpia, H. G. Craighead, and P. L. McEuen, “Impermeable atomic membranes from graphene sheets,” *Nano Lett.* 8, 2458-2462 (2008).
- [18] L. Teng and Z. Zhao, “Substrate-regulated morphology of graphene,” *J. Phys. D: Appl. Phys.* 43, 075303 (2010).
- [19] X. Wang, J. Xu, Y. Zhu, K. L. Cooper, and A. Wang, “All-fused-silica miniature optical fiber tip pressure sensor,” *Opt. Lett.* 31, 885-887 (2006).

- [20] M. Bruna and S. Borini, "Optical constants of graphene layers in the visible range," *Appl. Phys. Lett.* 94, 031901 (2009).
- [21] B. Yu, D. W. Kim, J. Deng, H. Xiao, and A. Wang, "Fiber Fabry-Perot sensors for detection of partial discharges in power transformers," *Appl. Opt.* 42, 3241-3250 (2003).
- [22] J. A. Bucaro, N. Lagakos, B. H. Houston, J. Jarzynski, and M. Zalalutdinov, "Miniature, high performance, low-cost fiber optic microphone," *J. Acoust. Soc. Am.* 118, 1406-1413 (2005).
- [23] O. Kilic, M. Digonnet, G. Kino, and O. Solgaard, "External fibre Fabry-Perot acoustic sensor based on a photonic-crystal mirror," *Meas. Sci. Technol.* 18, 3049 (2007).
- [24] F. B. Shen, J. C. Xu, and A. Wang, "Measurement of the frequency response of a diaphragm-based pressure sensor by use of a pulsed excimer laser," *Opt. Lett.* 30, 1935-1937 (2005).
- [25] C. K. Kirkendall and A. Dandridge, "Overview of high performance fibre-optic sensing," *J. Phys. D: Appl. Phys.* 37, R197-R216 (2004).

## Chapter 6

# Graphene diaphragm based micro-mechanical resonators

### 6.1 Introduction

Mechanical resonators have been used in force, acceleration and pressure detection by monitoring the resonant frequency or the quality factor [1]. Resonators with different vibrating structures such as diaphragms, beams and cantilevers have been reported [2-4]. For an aluminum-coated silicon diaphragm which is optically excited, its resonant frequency is dependent on the pressure difference between the two sides of the diaphragm. The pressure difference deflects the diaphragm and the diaphragm deflection changes the stress in the diaphragm and thus the stress-dependent resonance frequency of the resonator. Based on the pressure-induced resonant frequency change, the resonator based on the diaphragm can be used as a pressure sensor [2]. Similarly, a beam-type resonator supported by two pillars attached to a pressure deflectable diaphragm has been reported for pressure sensing [3]. The above resonators show high pressure sensitivities, while the complete sealing of the cavity beneath the diaphragm adds the complexity for the sensor fabrication. The need of the cavity sealing (or air pressure difference besides the diaphragm) is obviated for the cantilever based pressure sensor which takes advantage of the air damping effect [4]. The dependence of the resonant frequency and quality factor of the cantilever on the pressure-dependent damping effect is investigated in detail [5]. However, the pressure sensitivity of the cantilever with a thickness at the micrometer-scale is

limited by the weak air damping effect and this effect can be enhanced by decreasing the thickness of the cantilever. The graphene film which has a nanometer-scale thickness provides the opportunity to significantly improve the pressure sensitivity of the resonator.

Recently, micro-mechanical resonators based on the graphene have drawn extensive interest. The first graphene micro-mechanical resonator is fabricated by mechanically exfoliating the graphene sheet onto predefined trenches in a SiO<sub>2</sub> substrate [6]. Due to the low-mass and the large surface-area of the graphene, the resonator can couple strongly to the outer environment and is promising for sensing applications [7]. To achieve mass production of the resonators, the graphene grown by the chemical vapor deposition (CVD) has also been transferred onto suspended trenches to fabricate large arrays of resonators with graphene sheets of different sizes and shapes [8-10]. To detect the resonant frequency of the graphene, a modulated light is launched and focused onto the graphene and the vibration amplitude of the graphene is measured from the interference of lights reflected from the graphene and the substrate, respectively. However, the launched light requires careful alignment to incident perpendicularly onto the graphene and the whole desktop system including the excitation and interrogation components might be bulky and difficult to operate for practical applications.

In this chapter, a ferrule-top pressure sensor based on the mechanical resonance of a graphene diaphragm is demonstrated. The resonator is excited and interrogated by an all-optical system, which delivers the excitation and interrogation lights by using just one piece of optical fiber. The ferrule-top graphene micro-mechanical resonator with this easy demodulation scheme is promising for mass, force and pressure measurements.

## 6.2 Theoretical basis for the graphene based micro-mechanical resonator

Before the discussion of the graphene resonator, the basic principle for a damped oscillator with a harmonic excitation is briefly introduced.

### 6.2.1 Damped oscillator with the harmonic excitation

Fig. 6.1 shows the spring-mass-damper model for a harmonically excited oscillator with viscous damping [11].

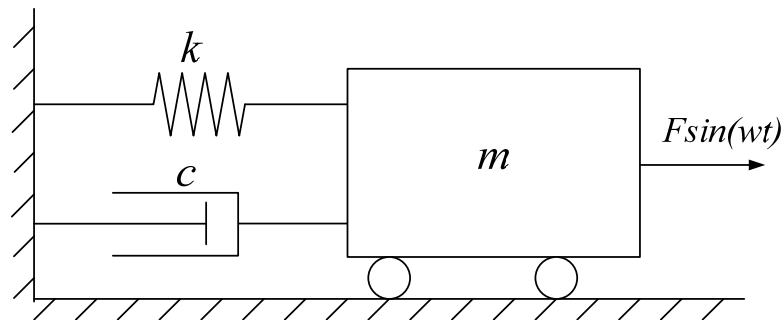


Fig. 6.1 Spring-mass-damper model for a forced resonator with viscous damping.

The oscillator with a body mass of  $m$ , is connected with a spring with constant stiffness of  $k$  and a viscous damper with a damping coefficient of  $c$ . Driven by a periodic force with an amplitude of  $F$  and an angular frequency of  $\omega$ , the equation for the motion of the oscillator can be expressed as,

$$m \frac{d^2 x}{dt^2} + c \frac{dx}{dt} + kx = F \cdot \sin(\omega t) \quad (6.1)$$

where  $x$  is the displacement of the oscillator. The steady-state solution to the Eq. (6.1) is,

$$x = \frac{F}{k} \frac{1}{\sqrt{\left(1 - \frac{\omega^2}{\omega_0^2}\right)^2 + \left(2\zeta \frac{\omega}{\omega_0}\right)^2}} \sin(\omega t - \theta) \quad (6.2)$$

where

$$\theta = \tan^{-1}\left(\frac{2\zeta(w/w_0)}{1-(w/w_0)^2}\right) \quad (6.3)$$

$$w_0 = \sqrt{\frac{k}{m}} \quad (6.4)$$

$$\zeta = \frac{c}{2mw_0} \quad (6.5)$$

$$Q = \frac{mw_0}{c} = \frac{1}{2\zeta} \quad (6.6)$$

$\theta$  is the phase,  $w_0=2\pi f_0$  is the resonant frequency,  $\zeta$  is the damping ratio and  $Q$  is the quality factor.  $Q$  is defined as the ratio of the stored potential energy to the dissipated energy per period for a damping system. In case of weak damping, the  $Q$  value can be determined from the measured resonant spectrum as,

$$Q = \frac{w_{peak}}{\Delta w_{peak}} \quad (6.7)$$

where  $\Delta w_{peak}$  is the bandwidth of 3dB-attenuation from the resonant peak  $w_{peak}$ . Fig. 6.2 shows the amplitude (normalized by  $FQ/k$ ) and the phase of the oscillator as functions of the frequency ratio ( $w/w_0$ ).

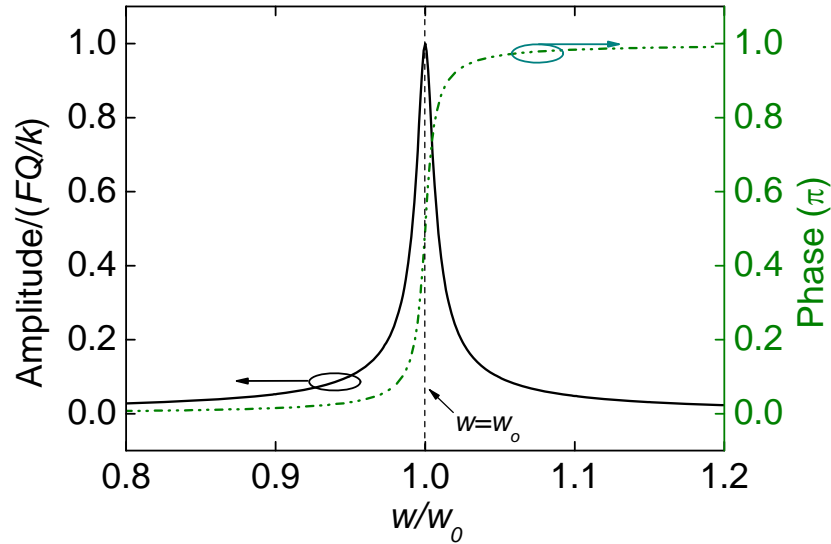


Fig. 6.2 The amplitude and phase as functions of the frequency ratio ( $w/w_0$ ) for the harmonically excited oscillator with viscous damping.

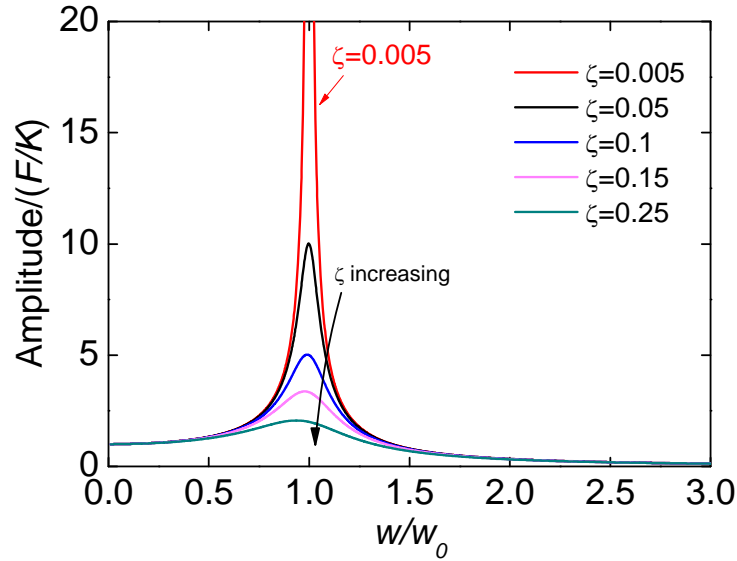


Fig. 6.3 Amplitude versus the frequency ratio for different values of  $\zeta$ .

As illustrated in Fig. 6.3, the oscillator experiences the largest amplitude at the value  $w/w_0$  less than 1 and the frequency for the maximum amplitude as well as the  $Q$  value decrease with the increase of the damping ratio  $\zeta$ .

For a resonator vibrating in the air, its behavior can be analyzed in a similar way to the harmonic oscillator except that the damping effect of air is more complicated than that of a viscous damper. The damping effect of air on the vibrating resonator can be divided into two parts, the acoustic radiation damping and the viscous damping [12].

The acoustic radiation damping results from the reaction force between the surrounding fluid and the vibrating resonator, which transfers the energy to the fluid by the sound emission. The fluid moves in phase with the resonator and its inertia can be modeled as an added virtual mass to the resonator. This added virtual mass decreases the resonant frequency of the resonator from the natural frequency in the vacuum. The added virtual mass is related to the kinetic energy of the fluid in motion with the resonator as well as the kinetic energy of the vibrating resonator itself and becomes considerable when the fluid has a density comparable to that of the resonator.

The viscous damping force is in phase with the velocity of the resonator and can be written in a complex form proportional to the velocity of the vibrating resonator as [5],

$$F_{drag} = (\beta_1 + j\beta_2)u = \beta_1 u - \beta_2 \frac{du}{dt} / w \quad (6.8)$$

where  $u = u_0 e^{-j\omega t}$  is the velocity. The first term on the right hand side proportional to the velocity  $u$  is called the drag force and accounts for the energy dissipation. The second term proportional to the acceleration  $du/dt$  is called the inertial force. As a result, the viscous damping effect contributes to both the drag force and the inertial force.

## 6.2.2 Theoretical analysis of the damped resonant beam

In Chapter 3, the viscous damping effect of air has not been considered since it is very small (less than 1 percent) compared to the acoustic radiation effect [13, 14]. To model the air damping effect more accurately, the effects of the acoustic radiation and viscous damping on the resonant frequency of the resonator are both considered for the clamped-clamped beam here.

The clamped-clamped beam can be modeled by the Euler-Bernoulli beam theory by assuming that the shear deformation and transverse strain are negligible for slender beams. If the beam is not slender, the Timoshenko theory must be employed to consider the shear force and rotary inertia [15]. For a beam with length  $L$ , width  $W$ , and thickness  $d$ , the free motion of the beam can be described by [5, 16, 17],

$$\frac{EI}{L^4} \frac{\partial^4 y(\eta, t)}{\partial \eta^4} + f_1 \frac{\partial y(\eta, t)}{\partial t} + [\rho_s A(1 + \beta_{rad}) + f_2] \frac{\partial^2 y(\eta, t)}{\partial t^2} = 0 \quad (6.9)$$

where,

$\eta = x/L$ : the normalized length

$E$ : Young's modulus

$I$ : the moment of inertial of the beam ( $Wd^3/12$ )

$f_1$ : the drag force parameter per unit length ( $\beta_1/L$ )

$f_2$ : the inertial force parameter per unit length ( $\beta_2/wL$ )

$\rho_s$ : the mass density of the beam  
 $A$ : the cross-section area ( $Wd$ )  
 $\beta_{rad}$ : the added virtual mass coefficient due to acoustic radiation

As the viscous damping force in Eq.(6.8) is defined for the harmonic motion, the result derived from Eq.(6.9) is only applicable for the harmonic vibration. The eigenvalue for the damped frequency of the clamped-clamped beam  $w_d$  can be derived by solving Eq.(6.9), and the solution is,

$$w_d = \left( \frac{EI k_n^4}{[\rho_s A(1 + \beta_{rad}) + f_2] L^4} - \frac{1}{4} \left[ \frac{f_1}{\rho_s A(1 + \beta_{rad}) + f_2} \right]^2 \right)^{1/2} \quad (6.10)$$

The second term in the square root might be neglected as the viscous drag force  $f_1$  is small in air. Eq. (6.10) can then be simplified as,

$$w_d = \left( \frac{EI k_n^4}{[\rho_s A(1 + \beta_{rad}) + f_2] L^4} \right)^{1/2} = w_n \left[ (1 + \beta_{rad}) + \frac{f_2}{\rho_s A} \right]^{-1/2} \quad (6.11)$$

$$w_n = k_n^2 \frac{d}{L^2} \sqrt{\frac{E}{12\rho_s}} \quad (6.12)$$

For a clamped-clamped beam,  $k_n=4.73$  for the first-order resonant mode ( $n=1$ ). The quality factor  $Q$  can be determined from the definition by,

$$Q = \frac{2\pi U_s}{U_D} \quad (6.13)$$

where  $U_s$  is the stored vibration energy and  $U_D$  is the dissipated energy per period. If the displacement of the harmonic motion is described with the separated variables  $\eta$  and  $t$  as,

$$y(\eta, t) = w(\eta)Y(t) = w(\eta)e^{j\omega t} \quad (6.14)$$

the stored vibration energy  $U_s$  equal to the maximum kinetic energy can be calculated by,

$$\begin{aligned}
 U_s &= \int_0^1 \frac{1}{2} L (\rho_s A(1 + \beta_{rad}) + f_2) \left( \frac{\partial y(\eta, t)}{\partial t} \right)_{\max}^2 d\eta \\
 &= \frac{1}{2} L [\rho_s A(1 + \beta_{rad}) + f_2] w^2 \int_0^1 w(\eta)^2 d\eta
 \end{aligned} \quad (6.15)$$

The dissipated energy per period  $U_D$  can be calculated by,

$$U_D = \int_0^T P u dt = \int_0^1 \int_0^T L f_1 \left( \frac{\partial y(\eta, t)}{\partial t} \right)^2 dt d\eta = L f_1 w^2 \int_0^1 w^2(\eta) \int_0^T \cos^2 wt dt d\eta \quad (6.16)$$

where  $P$  is the drage force, and  $T=2\pi/w$  is the period of the motion. Substituting Eq. (6.15) and (6.16) into Eq. (6.13), the quality factor due to the viscous damping  $Q_{vis}$  can be calculated by,

$$Q_{vis} = \frac{[\rho_s A(1 + \beta_{rad}) + f_2]w}{f_1} \quad (6.17)$$

It needs to mention that the energy dissipation due to the acoustic radiation is not considered in Eq. (6.17). According to [18], the energy dissipation induced by the acoustic radiation effect cannot be ignored for this thin beam, which is reflected in the significant decrease of the resonant frequency induced by the acoustic radiation. The damping ratio  $\zeta$  for the acoustic radiation of a plate with the dimensions of  $a$  by  $b$  can be estimated by,

$$\zeta = \frac{1}{4\pi} \frac{\rho_f a^2 b}{M} \frac{\lambda}{a} \Theta \quad (6.18)$$

$$\Theta = \begin{cases} (\pi/2)^2 \cdot (a^2 + b^2)/\lambda & \text{for } a/\lambda \ll 0.2 \\ 1 & \text{for } a/\lambda \gg 0.2 \end{cases} \quad (6.19)$$

where  $\rho_f$  is the mass density of the fluid surrounding the plate,  $M$  is the mass of the plate, and  $\lambda=2\pi c/w$  is the wavelength of the sound wave radiated by the vibrating plate.

The quality factor due to acoustic radiation  $Q_{rad}$  can be derived from the following relationship,

$$Q_{ac} = \frac{1}{2(w/w_n)\zeta} \quad (6.20)$$

where  $w_n$  is the undamped natural frequency. Based on Eq. (6.17) and Eq. (6.20), the quality factor of the system  $Q_{sys}$  can then be calculated by,

$$\frac{1}{Q_{sys}} = \frac{1}{Q_{ac}} + \frac{1}{Q_{vis}} \quad (6.21)$$

To analyze the resonant frequency and quality factor of the beam, the added virtual mass coefficient  $\beta_{rad}$  and the viscous damping parameters  $f_1$  and  $f_2$  should be

determined and they are discussed in the following parts.

The added virtual mass per unit length accounting for the acoustic radiation of a circular cylinder in a fluid with mass density of  $\rho_f$  can be given by [19],

$$M_{rad} = \rho_f \frac{\pi D^2}{4} \quad (6.22)$$

where  $D$  is the diameter of the cylinder which is equal to the beam width  $W$ . To consider the difference between the rectangular beam and the circular cylinder, a coefficient  $\alpha$  is introduced and Eq. (6.22) becomes,

$$M_{rad} = \alpha \rho_f \frac{\pi D^2}{4} \quad (6.23)$$

The coefficient  $\alpha$  depends on the value of the width/thickness ratio of the beam, as listed in Table 6.1 [20].

Table 6.1 Coefficient  $\alpha$  for different values of  $W/d$ .

$W/d$	0.1	0.2	0.5	1.0	2.0	5.0	10.0	$\infty$
$\alpha$	2.23	1.98	1.70	1.51	1.36	1.21	1.14	1.0

The added virtual mass coefficient due to the acoustic radiation ( $W/d \gg 1$ ) can then be expressed as,

$$\beta_{rad} = \rho_f \frac{\pi D^2}{4} / \rho_s W d = 0.785 \frac{\rho_f W}{\rho_s d} \quad (6.24)$$

For the viscous damping effect, according to the study of a silicon cantilever [5], the viscous damping force is dependent on the air pressure and the dominant damping mechanism for the pressure from the vacuum to the atmosphere can be divided into three regions: the intrinsic, the molecular and the viscous.

#### **The intrinsic region:**

Due to the low air pressure, the intrinsic damping of the beam dominates and the air damping effect is negligible. As a result,  $f_1$  and the corresponding  $Q$  is pressure independent and  $f_2$  is equal to zero thus  $w_d = w_n$ .

#### **The molecular region:**

In this region, the damping results from the independent collisions between the moving surface of the beam and the non-interacting air molecules. We still have  $f_2=0$ , and  $f_1$  can be determined by using the kinetic theory of gases as,

$$f_1 = k_m W p \quad (6.25)$$

$$k_m = \sqrt{32M/9\pi RT} \quad (6.26)$$

where  $p$  is the air pressure,  $W$  is the beam width,  $M$  is the mass per mol of the gas molecular,  $R$  is the gas constant and  $T$  is the absolute temperature. For nitrogen gas at room temperature,  $T=298.5$  K,  $M=28.9$ ,  $k_m$  is calculated to be 0.0036 s/m.

### The viscous region:

In this region, the air behaves like a fluid and needs to be studied by the fluid mechanics. The fluid may be considered as being incompressible since the velocity of the vibrating beam is normally significantly smaller than the sound speed in the fluid. The viscous damping force in the incompressible viscous fluid has been studied by applying the Navier-Stokes equation and the continuity equation [5].

To obtain a simple analytic solution for the problem, modeling the vibrating beam as a string of spheres is used in several studies [5, 21]. If the Reynolds number is small,  $f_1, f_2$  for a sphere with radius  $R_s$  can be expressed as,

$$f_1 = 6\pi\mu R_s (1 + R_s / \delta) / L \quad (6.27)$$

$$f_2 = \frac{2}{3} \pi R_s^3 \rho_f \left(1 + \frac{9}{2} \frac{\delta}{R_s}\right) / L \quad (6.28)$$

where  $\delta$  stands for the width of the boundary layer perpendicular to the motion direction and is given by  $(2\mu/\rho_f w)^{1/2}$ , where  $w$  is the angular frequency of the vibration, and  $\mu$  and  $\rho_f$  are the dynamic viscosity and the mass density of the fluid, respectively. In Eq. (6.28), the first term on the right hand side accounts for the acoustic radiation effect and the second term describes the viscous damping effect. The acoustic radiation effect is somewhat included in the calculation of the inertial

force parameter for the viscous damping. To be consistent with the previous definition, only the second term is considered for the viscosity-related added mass effect.

After substituting Eq. (6.27) and Eq. (6.28) into Eq. (6.11), the relative resonant frequency shift as functions of the air pressure for the beam with/without the viscous damping were calculated and are plotted in Fig. 6.4. For thick beams (e.g.,  $d = 20$  nm), the viscous damping is negligible compared to the acoustic radiation. For slender beams (e.g.,  $d = 5$  nm), the viscous damping is necessary to consider for accuracy.

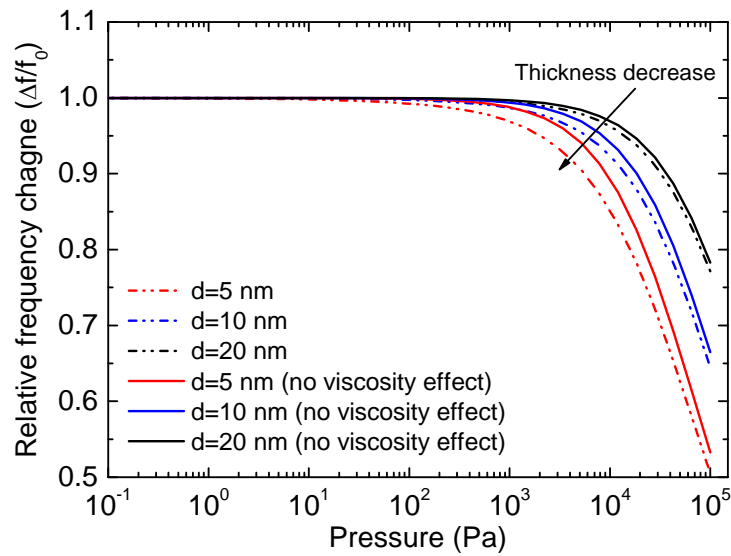


Fig. 6.4 Relative frequency changes for beam resonators with the thickness of 5, 10, 20 nm with/without considering the viscosity effect.

The parameters used in the calculation are listed in Table 6.2 with the air considered as pure nitrogen.

Table 6.2 Physical parameters of the graphene beam and the nitrogen gas in the calculation.

<b>Beam resonator (graphene)</b>	<i>Beam width <math>W</math> (<math>\mu\text{m}</math>)</i>	30	<i>Beam length <math>L</math> (<math>\mu\text{m}</math>)</i>	125
	<i>Beam thickness <math>d</math> (nm)</i>	5-10	<i>Density (<math>\text{kg}/\text{m}^3</math>)</i>	2200
	<i>Young's modulus <math>E</math> (Pa)</i>	$1e12$	<i>Poisson ratio</i>	0.17
<b>Nitrogen (at 1 atm, 25 °C)</b>	<i>Density (<math>\text{kg}/\text{m}^3</math>)</i>	1.14	<i>Dynamic viscosity (Pa·s)</i>	$1.66e-5$
	<i>Speed of sound (m/s)</i>	352	<i>Gas constant <math>J/(\text{mol}\cdot\text{K})</math></i>	8.314

### **6.3 Fabrication of the graphene diaphragm based micro-resonator**

Compared to the few-layer graphene (FLG) grown on the Ni substrate as we discussed in Chapter 5, the single-layer graphene (SLG) grown on the copper (Cu) substrate has a uniform thickness distribution over the whole substrate area. This uniform graphene film is promising for building high-performance mechanical resonators. However, the SLG is easily broken in the process of transferring the graphene onto the perforated substrate. Graphene-transferring assisted by the poly(methyl methacrylate) (PMMA) has been successfully demonstrated for the fabrication of the suspended SLG mechanical resonator [9, 10]. In the above fabrication process, a post-process such as the critical point drying technique or the high temperature heating under argon/hydrogen environment is employed to remove the PMMA without damaging the graphene. The post-process, however, is complicated and might not be suitable for the optical fiber since the coating layer of the optical fiber is easily corroded by the acetone or burnt out during the high temperature heating treatment.

Instead of the SLG, a graphene film with a layer number of  $\sim 10$  is used to build the resonator for the following reasons:

- 1) Simplifying the transferring process and avoid degradation of the mechanical performance of the fiber. The thicker graphene film can endure the surface tension of the acetone without being broken, and thus make the post-process unnecessary.
- 2) Offering more flexibility in the physical size of the resonator. The diameter of the suspended thicker graphene film can extend up to one hundred micrometers while the diameter of the SLG reported is limited to several tens of micrometers.

- 3) Improving the efficiency of the resonator excitation. For an optically excited resonator, the large optical absorption coefficient requires a low level of the excitation light. The optical absorption coefficient for the SLG is  $\sim 2.3\%$  and increases with the layer number of the graphene film.

As the layer number of the graphene grown on the Cu substrate is limited to 1-2 layers due to the low solubility of the carbon in the Cu, the multi-layer graphene (MLG) is obtained by stacking the SLG layer by layer. The process is schematically shown in Fig. 6.5.

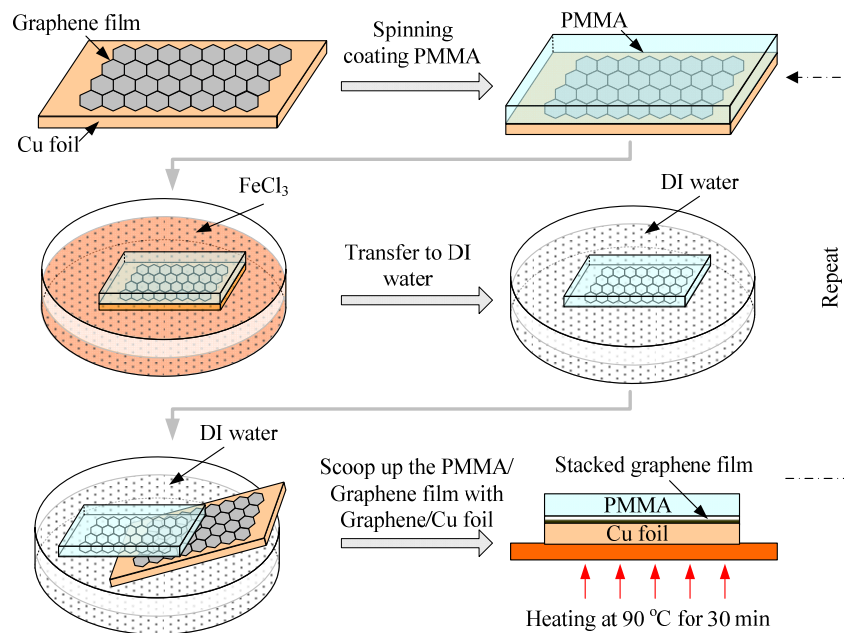


Fig. 6.5 Schematic of the fabrication process for the MLG film.

- Step 1) The graphene/Cu foil is spin-coated with a PMMA solution (average  $M_w \sim 996000$ , Sigma-Aldrich, dissolved in anisole with a concentration of 20 mg/mL) and left in the air to dry. The speed and time set for the spin coater is 3000 rpm and 30 seconds.
- Step 2) The Cu foil is etched away by using the iron chloride ( $\text{FeCl}_3$ ) solution with a concentration of 20 mg/mL. After that, the graphene/PMMA film is rinsed in the de-ionized (DI) water five times.

Step 3) The PMMA/Graphene film floated on the DI water is scooped up with another piece of flat graphene/Cu foil and the PMMA/Graphene/Cu sample is heated at 90 °C for ~ 30 min to dry the sample.

Step 4) Repeated the process 2 and 3 to stack more layer of graphene between the PMMA and Cu foil.

To decrease the number of the repeating time needed to stack a 10-layer graphene film, a Cu foil with two-layer graphene instead of that with the SLG is used in the experiment. The average thickness of the stacked 10-layer graphene film is measured and found to be ~10-20 nm by using the atomic force microscope. Considering that the measured thickness for the CVD produced SLG is ~1 nm, the large value is reasonable when considering the space existing between the stacked graphene layer and the possible residual of the PMMA.

Fig. 6.6 shows the process of transferring the stacked PMMA/graphene film to the ferrule top to construct the graphene diaphragm based resonator.

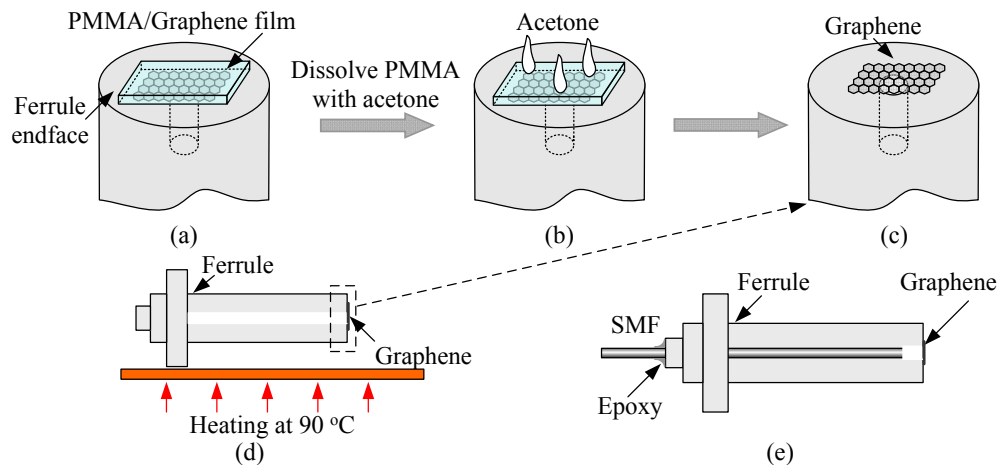


Fig. 6.6 Schematic of the process for transferring the MLG film to the ferrule top.

Step 1) The PMMA/Graphene film is transferred onto the endface of the ferrule with a bore-diameter of 125  $\mu\text{m}$ . The ferrule top with the film is then heated under 90 °C for 30 min to fasten the film onto the ferrule top.

Step 2) The PMMA/Graphene film is immersed in the acetone for several minutes to remove the PMMA layer. The graphene covering the ferrule endface is then dried in the air.

Step 3) A cleaved single mode fiber (SMF) is inserted into the ferrule to approach the graphene film. The cavity length, i.e., the distance between the fiber end and the graphene, is controlled through a translation stage and monitored through the reflection spectrum measured by the OSA. The SMF is then fixed into the ferrule by an epoxy as shown in Fig. 6.6(e).

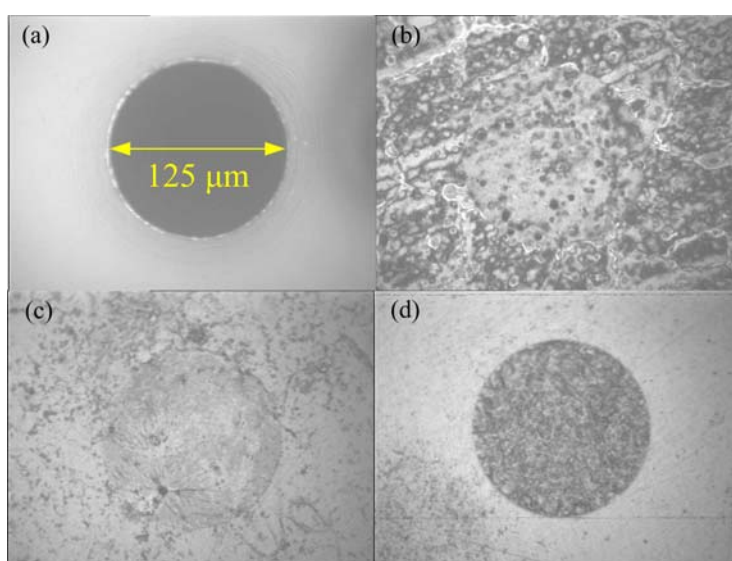


Fig. 6.7 Microscope images of (a) the ferrule endface; (b) the ferrule endface with the PMMA/graphene film; (c) the ferrule endface with PMMA removed; (d) sample in (c) after being heated at 400 °C for 2 hours.

Fig. 6.7(a-c) shows the microscope images of the ferrule endface, the ferrule endface with PMMA/graphene film and with PMMA removed, respectively. PMMA residuals are observed on the surface of the graphene, and further washing by using the acetone shows no obvious reduction of the residuals (see Fig. 6.7(c)). As the Young's modulus of the graphene is hundreds of times larger than that of the PMMA, the PMMA film will have a negligible effect on the mechanical properties of the graphene film with the thickness at the same scale. Heating this PMMA/graphene

film at 400 °C in an argon environment for 2 hours has also been attempted and the graphene surface is substantially cleaned (Fig. 6.7(d)). However, the surface of the graphene is found to wrinkle severely and further investigation to improve this heating method will be conducted in the future.

## 6.4 Optical excitation and interrogation of the micro-resonator

### 6.4.1 Optical excitation

Electrostatic, resistive heating and optical heating excitations are several of the most common methods to excite the vibration of the micro-resonator [1]. Compared to the electrostatic/resistive heating excitation which adopts the alternating electrical field/current to actuate the resonator, the optical heating excitation uses the periodically modulated light to heat the resonator without the need of electrical contracts. The resonator is excited by the heating induced thermal expansion or contraction of itself. Since the excitation light can be directly delivered by the optical fiber in the ferrule, no careful alignment of the optical path is needed to focus the light onto the diaphragm surface. As the actuation is based on the thermal expansion and contraction of the resonator, the maximum modulated frequency is limited by the thermal time constant  $T_{cont}$  of the resonator.  $T_{cont}$  should be less than the time period of the vibrations ( $1/f=2\pi/w$ ) to achieve the thermal equilibration. For a circular diaphragm with a radius of  $R$ ,  $T_{cont}$  is given by [22],

$$T_{cont} = \frac{c\rho}{\kappa} \left( \frac{\mu}{R} \right)^{-2} \quad (6.29)$$

where  $\kappa$  is the thermal conductivity,  $c$  is the specific heat,  $\rho$  is the mass density, and  $\mu= 2.4$ . For graphene,  $\kappa \approx 5 \times 10^3$  W/(m·K) [23],  $c \approx 0.7 \times 10^3$  J/(kg·K) [24],  $\rho \approx 2.2$

$\text{kg/m}^3$  [25].  $T_{cont}$  of the graphene diaphragm with the radius  $R= 62.5 \mu\text{m}$  is calculated to be  $\sim 0.2 \mu\text{s}$ , which corresponds to the time period of the optical excitation with a frequency of 5 MHz. This value is well above the measured resonate frequency of our fabricated graphene micro-mechanical resonators.

## 6.4.2 Optical interrogation

A typical reflection spectrum of the resonator is shown in Fig. 6.8. The interference contrast is up to 13 dB, and this is attributed to the larger reflectivity of the stacked MLG compared with that of the SLG. The pressure response of the resonator has been tested by applying a static pressure change. The interference spectrum shifts blue and returns to its initial position quickly, indicating that the air cavity at the ferrule top is not sealed. The pressure sensitivity of this resonator can be measured in a similar way to the MLG based acoustic sensor in Chapter 5.

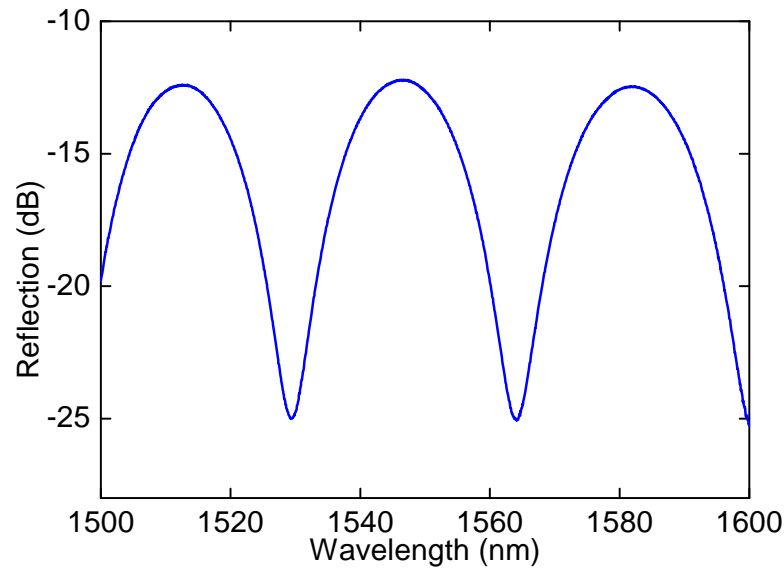


Fig. 6.8 A typical reflection spectrum of the graphene diaphragm based resonator.

An all-fiber system has been designed to measure the resonant frequency of the graphene resonator formed at the ferrule top as shown in Fig. 6.9. Two optical lasers with different central wavelengths ( $\lambda_1$  and  $\lambda_2$ ) have been used, respectively, for the

optical thermal excitation and interrogation of the vibration of the graphene diaphragm.

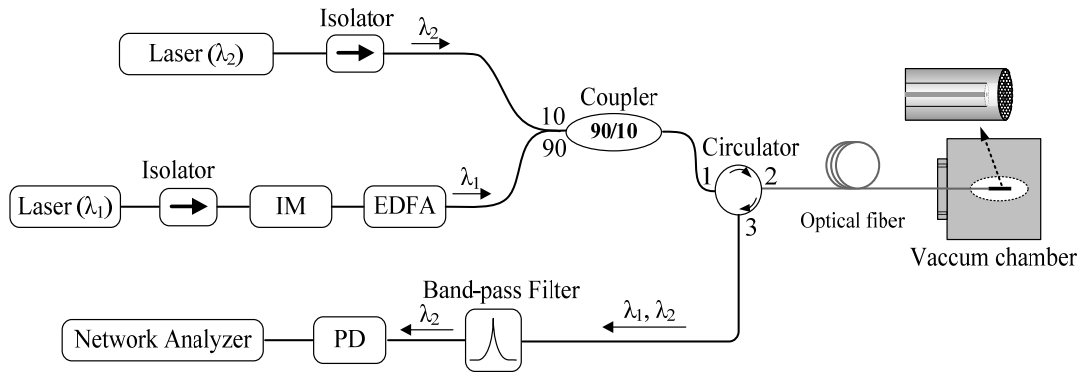


Fig. 6.9 Schematic of an all-fiber system for measuring the resonant frequency of the graphene diaphragm based resonator.

For the excitation, the light from the semiconductor laser working at a wavelength of  $\lambda_1$  (1531 nm) passes through the intensity modulator (IM) and is delivered to the resonator through the fiber pigtail connected to the optical coupler. The broadband absorption spectrum of the graphene offers excellent flexibility for the selection of the light wavelength for excitation [26].

For the interrogation, the light from another laser working at a wavelength of  $\lambda_2$  (1510 nm) is injected into the system through the second port of the same coupler and reaches the resonator through the same fiber pigtail as  $\lambda_1$ . The phase difference between the light reflected by the silica fiber end and that reflected by the graphene surface will change due to the vibration of the graphene. The intensity of the reflected light after passing through the circulator is received by the photo-detector (PD) and is modulated with a frequency the same as that of the vibration.

To avoid the interference between the excitation light  $\lambda_1$  and the interrogation light  $\lambda_2$ , the reflected light from the resonator passes through a band-pass filter (BPF) before being detected by the PD. The network analyzer can detect and analyze the frequency of the electric signal from the PD. The resonant frequency corresponds to the point where the largest PD signal appears during the adjustment of the frequency

of the excitation light  $\lambda_l$ .

Suffering from the low output intensity of the distributed feedback (DFB) laser ( $\lambda_l$ ) and the large attenuation of the IM used, the light after being modulated by the IM is amplified by the EDFA. The output intensities  $W$  of the EDFA with different injected currents  $I$  are shown in Fig. 6.10. As the current increases up, the intensity for the input light from the DFB laser at 1531 nm and the spontaneous light of the EDFA increase simultaneously. The spontaneous light is filtered out by using a Fabry-Perot tunable filter (FP-TF) with the central wavelength of the pass-band tuned to 1531 nm. The excited light is then combined with the interrogating light through the coupler and delivered to the graphene diaphragm by the circulator. The spectrum of the light reflected by the graphene diaphragm is recorded and plotted in Fig. 6.11. The peaks located at the wavelength of 1513 nm and 1531 correspond to the interrogation light and the excitation light, respectively. The small peak at 1576 nm comes from the second pass-band of the FP-TF due to its feature of periodic pass-bands. After passing through the BPF before the PD, only the interrogating light is left, which is indicated by the red light in Fig. 6.11.

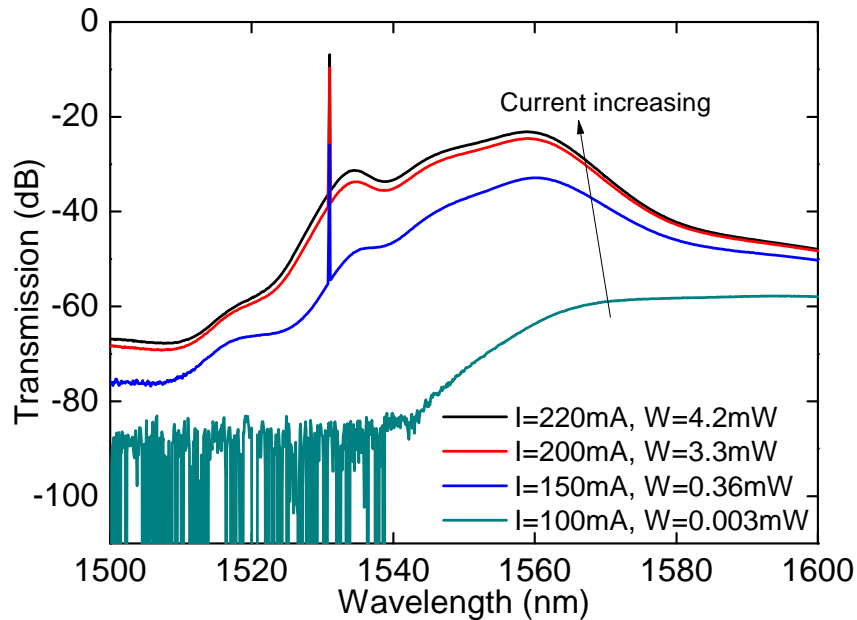


Fig. 6.10 Spectrums of the EDFA output with different injected currents.

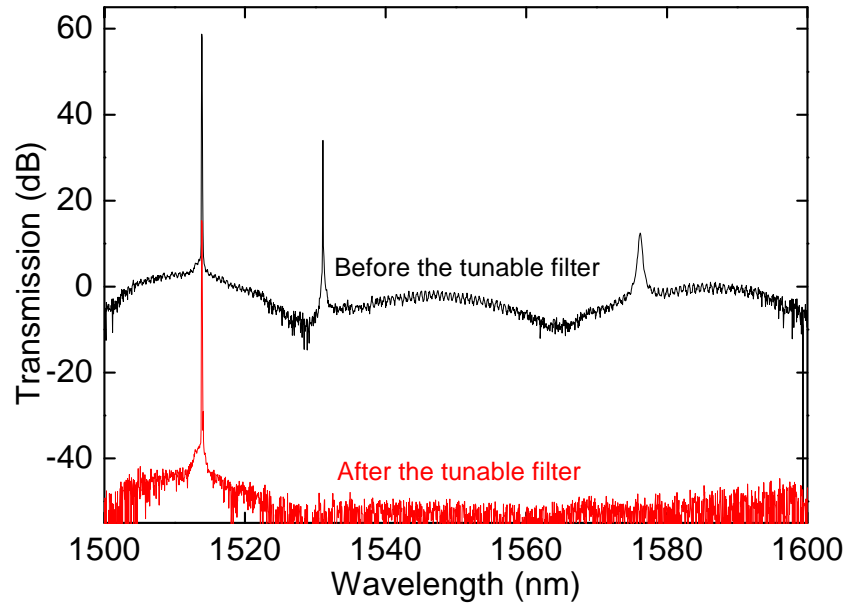


Fig. 6.11 Spectrums of the light intensity reflected by the graphene before and after the band-pass filter. The spectrums are offset vertically for the purpose of easy observation.

The resonator is placed in a vacuum chamber (Model: Pfeiffer, TSV-P1) and measurements are performed at room temperature in the vacuum ( $2 \times 10^{-5}$  mBar). Fig. 6.12 shows the measured frequency spectrum of a circular graphene diaphragm based resonator. Multiple resonant peaks are observed and the peak with the lowest frequency of 185 kHz exhibits the highest amplitude. If this peak is regarded as the fundamental mode of the resonator, the frequencies for the higher order modes can be calculated according to Eq.(3.35), as denoted in Fig. 6.12 by the red vertical dash lines. For a 10-layer graphene diaphragm with a thickness of  $\sim 10$  nm, the stress in the diaphragm is calculated to be 0.02 N/m, which is smaller than that for the SLG diaphragm [27]. The difference between the experimental and the calculated results might result from the PMMA residual on the graphene as shown in Fig. 6.7(c). The fundamental frequency and the  $Q$  values for our samples measured in the vacuum are varied from 170-520 kHz and 58.4-250, respectively. The excitation energy used in the experiment is  $\sim 100$   $\mu$ W, which benefits from the large light absorption coefficient of the graphene ( $\sim 2.3\%$  for monolayer graphene).

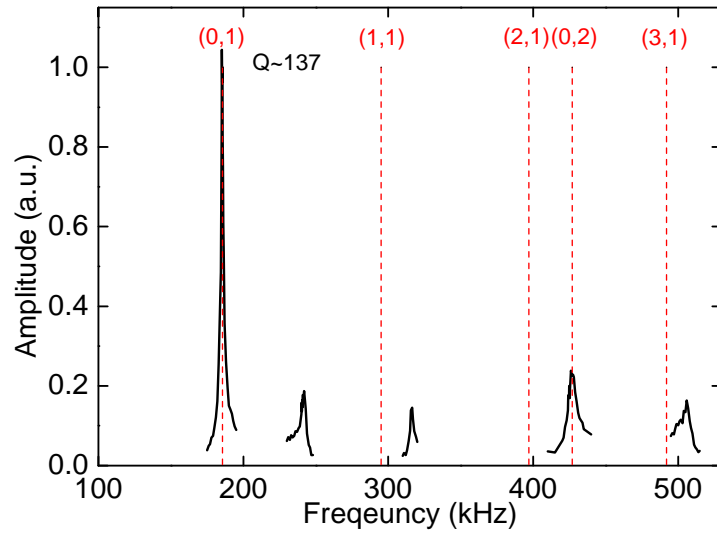


Fig. 6.12 Amplitude versus frequency of the circular graphene diaphragm in the vacuum ( $2 \times 10^{-5}$  mBar); red dash line denotes the calculated frequencies of the high order resonant modes.

### 6.4.3 Effects of air pressure

The effects of air pressure on the behavior of the resonator in terms of the quality factor and the resonant frequency are investigated, as shown in Fig. 6.13 and Fig. 6.14. The  $Q$  value decreases from 137 to 7.35 as the pressure increased from  $2 \times 10^{-5}$  to 100 mBar, which might result from the acoustic radiation and the air viscous damping [28, 29].

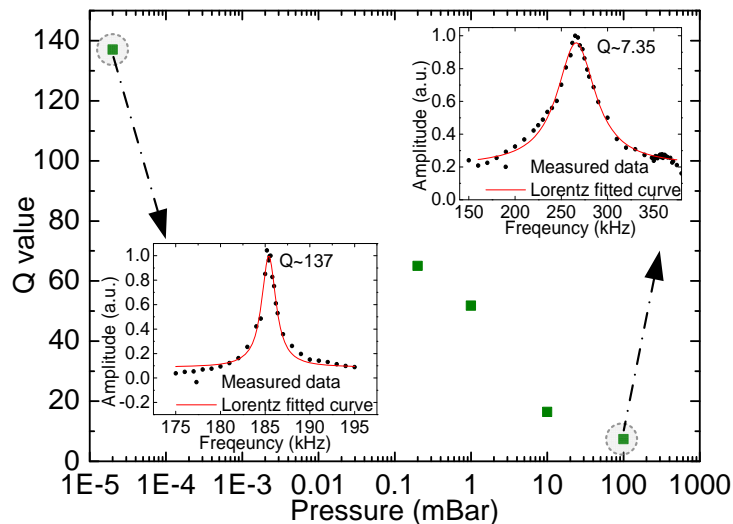


Fig. 6.13  $Q$  value of the fundamental mode as a function of the air pressure; Inset: the frequency responses of the resonator at the pressure of  $2 \times 10^{-5}$  and 100 mBar.

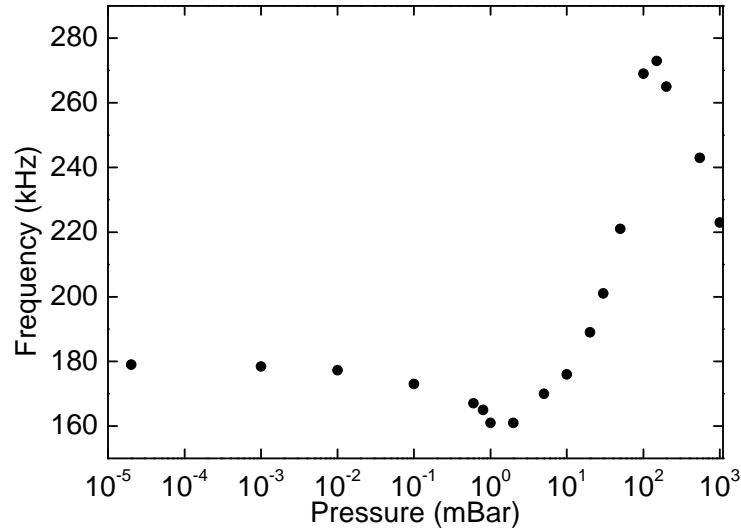


Fig. 6.14 Resonant frequency of the fundamental resonant mode as a function of the air pressure.

The resonant frequency of the resonator decreases with the increase of the pressure from  $2 \times 10^{-5}$  mBar to  $\sim 1$  mBar, with a similar trend to that reported in [28]. However, for the pressure in the range from 1 mBar to 100 mBar, the resonant frequency increases with a turning point observed near the pressure of 1 mBar. The frequency responses of the high-order resonant modes to pressure exhibit similar trends as shown in Fig. 6.15.

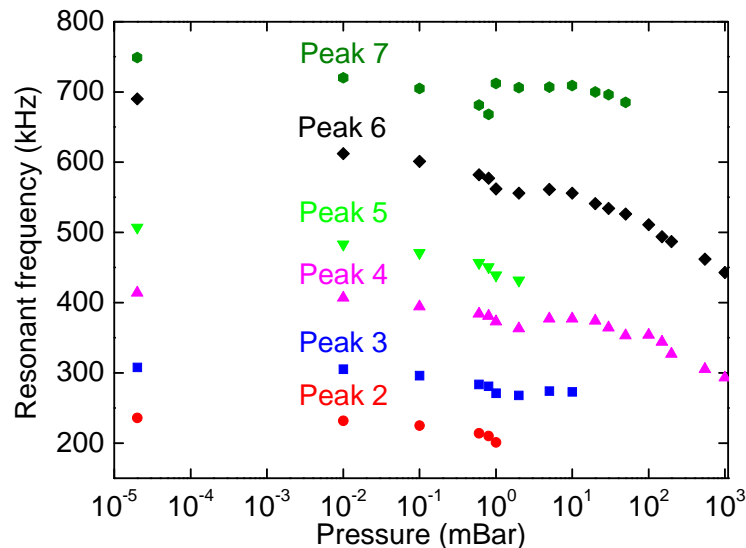


Fig. 6.15 Resonant frequencies of high-order resonant modes as functions of the air pressure.

Similar frequency responses have been reported in [30, 31] and the increase of the resonant frequency is believed to result from the increased thermal conductivity of air when the pressure increases in the molecular flow region. However, for the graphene with a negative thermal expansion coefficient [32], the increased thermal conductivity of air leads to a decreased temperature in the graphene diaphragm. The lower temperature is supposed to reduce the stress in the graphene diaphragm and decrease the resonant frequency of the resonator. One possible explanation is the effects of the residual PMMA, which has a positive thermal expansion coefficient and is difficult to be completely removed from the graphene film. In addition, considering the cavity partially sealed by the graphene diaphragm, the air flow during the pressure up/down process in the chamber may affect the resonant frequency of the resonator. The squeeze damping effect might also play a role as the cavity length of the resonator (a few tens of micrometers) is much less than the diameter of the graphene diaphragm.

## **6.5 Post-processing of the graphene diaphragm by the femtosecond laser**

To alleviate the possible effects of the air flow on the performance of the resonator, the circular graphene diaphragm on the ferrule top is post-processed into a beam shape by using a femtosecond (fs) laser. The post-processing is carried out by using a Ti: sapphire regenerative amplifier system (Spectra-Physics) with pulses of a central wavelength of 800 nm, a repetition rate of 1 kHz and duration of 120 fs. The fs pulses are focused onto the surface of the graphene diaphragm by a microscope objective and have a spot size (diameter at  $1/e^2$  intensity) of  $\sim 2 \mu\text{m}$ . The intensity of the laser pulses are controlled by a half-wave plate in combination with a polarizer. The samples to be processed are mounted on a three-axis translation stage with a

positioning resolution of 0.1  $\mu\text{m}$ . The parameters for the fs laser processing are summarized in Table 6.3.

Table 6.3 Parameters for the fs fabrication.

Wavelength	Objective	Energy	Moving speed
800 nm	$\times 20$ , NA=0.5	20 nJ	10 $\mu\text{m/s}$

During the fabrication of the beam-shape grapheme diaphragm, the central part of the circular diaphragm is firstly separated by cutting two lines through the diaphragm (Fig. 6.16(a)) and the parts at the two sides are then gradually removed. Fig. 6.16(b) shows the fabricated beam-shape diaphragm with a length of  $\sim 125 \mu\text{m}$  and a width of  $30 \mu\text{m}$ . The cavity beneath the beam shape diaphragm is completely exposed to the outside environment.

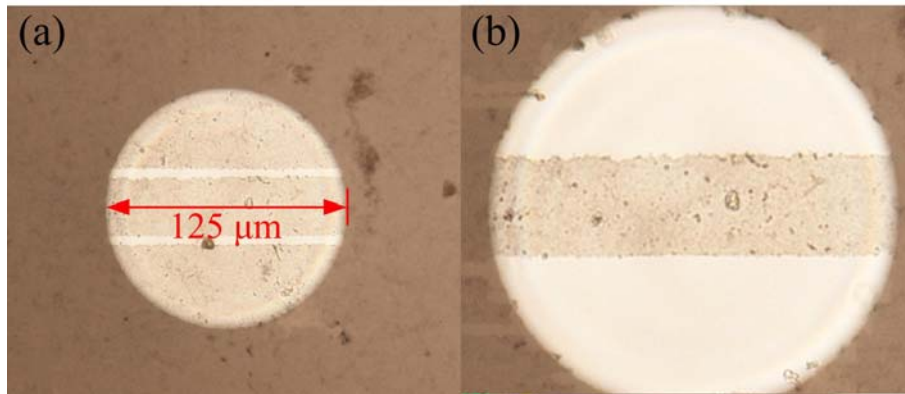


Fig. 6.16 Microscope images of (a) a circular graphene diaphragm with two scratch lines and (b) a beam-shape grapheme diaphragm manufactured by using the fs laser.

This beam-shape graphene diaphragm demonstrates a  $Q \sim 81$  in vacuum at the frequency of 135 kHz as shown in Fig. 6.17. The fundamental resonant frequency for a clamped-clamped beam with length  $L$  and thickness  $t$  is given by [6],

$$f_0 = \sqrt{\left( A \sqrt{\frac{E}{\rho}} \frac{t}{L^2} \right)^2 + \frac{0.57 A^2 S}{\rho L^2 t}} \quad (6.30)$$

where  $E$  and  $\rho$  are the Young's modulus and Poisson ratio of the beam, respectively.  $S$  is the tension per width of the beam, and  $A$  is equal to 1.03. The tension corresponding to the fundamental resonant frequency of  $\sim 135$  kHz is calculated to

be  $\sim 0.01$  N/m. The lower tension of the beam-shape graphene compared to that of the circular diaphragm might result from the change of the boundary condition: from all edges being tightly fixed for the circular diaphragm to two edges being free for the beam-shape diaphragm. If this peak (the lowest frequency) is taken as the fundamental frequency, the larger amplitude for the resonant peak at the frequency of 162 kHz might result from the mode splitting caused by the asymmetry of the graphene beam induced by the fs fabrication and the PMMA residual [33].

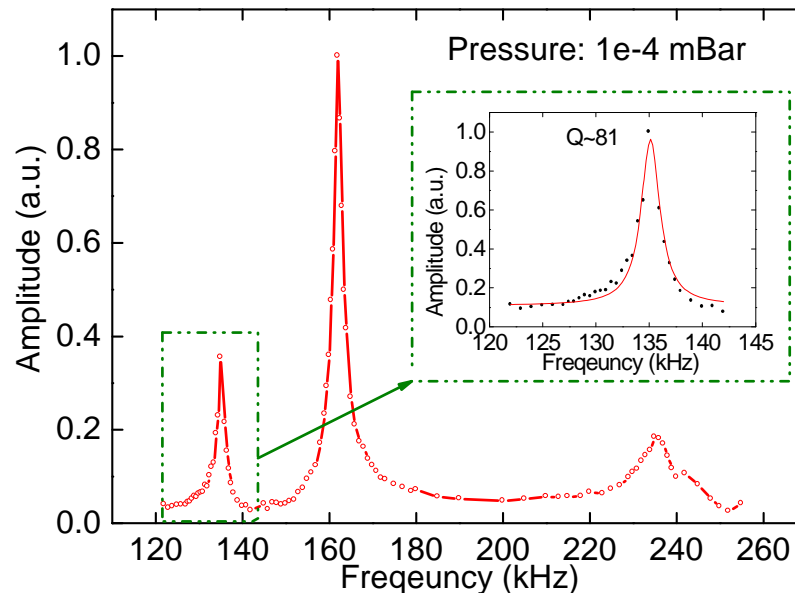


Fig. 6.17 Amplitude versus frequency of the beam-shape graphene diaphragm in vacuum ( $1 \times 10^{-4}$  mBar). Inset: enlarged part of the frequency response near the frequency of 135 kHz.

With the increase of the air pressure, the peak at 162 kHz is attenuated faster than the peak at 135 kHz, and is hardly observable when the pressure goes up to the atmosphere, as illustrated in Fig. 6.18.

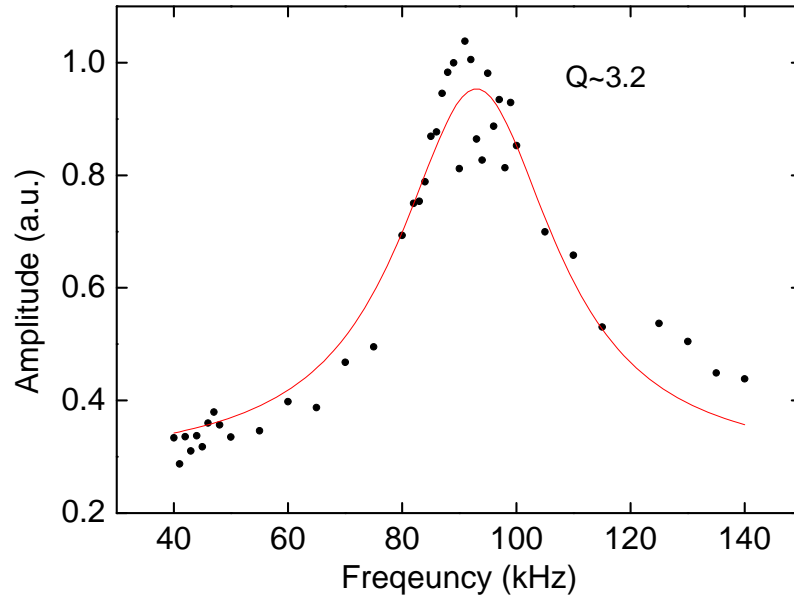


Fig. 6.18 Amplitude versus frequency of the beam-shape graphene diaphragm at the atmosphere (1000 mBar).

The  $Q$  value and the resonant frequency of the resonator both decrease with the increase of the pressure from  $1 \times 10^{-4}$  mBar to 1000 mBar, as shown in Fig. 6.19 and Fig. 6.20 respectively. The resonant frequency decreases with the pressure, without the appearance of the turning point as seen in Fig. 6.14 for the circular graphene diaphragm. This also demonstrates the importance of the effects caused by the air enclosed in the cavity. The effects of the air flow, the squeeze film damping as well as the PMMA residual on the resonant behavior of the graphene diaphragm based resonators are needed to be studied further.

For resonant peak 1 at 135 kHz, the frequency decreases to 88 kHz, which corresponds to a relative frequency shift of 34.8%. This result shows a similar trend to the calculated curve in Fig. 6.4 and is over one order of magnitude larger than that ( $\sim 1\%$ ) of the conventional resonators reported [5, 34]. This large shift of the resonant frequency is due to the small thickness of the graphene diaphragm which significantly amplifies the damping effect of the air when the diaphragm vibrates. Peak 2 shows a similar trend with peak 1, and the peak is difficult to distinguish from the frequency spectrum when the pressure is above 100 mBar due to its much attenuated amplitude.

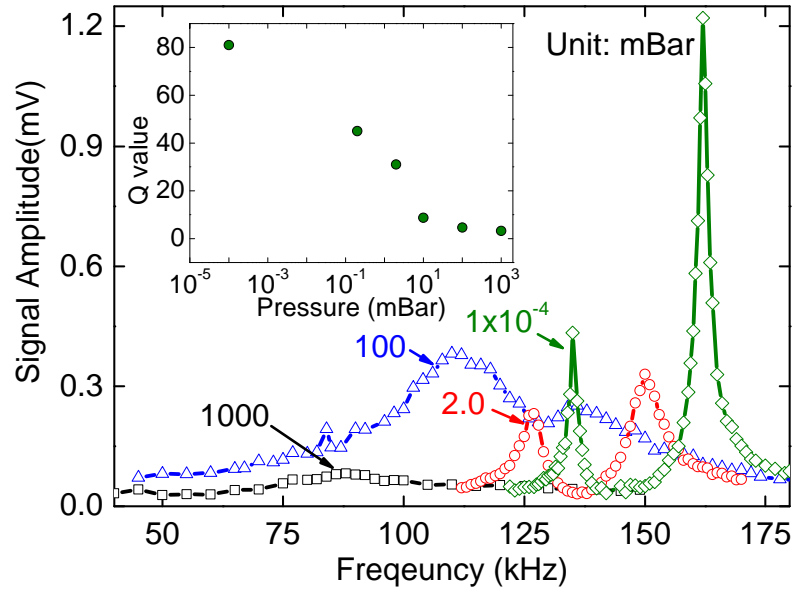


Fig. 6.19 Resonant spectrums of the beam-shape graphene diaphragm at different air pressures. Inset: Q values of the fundamental resonant mode of the beam-shape graphene diaphragm as a function of the air pressure.

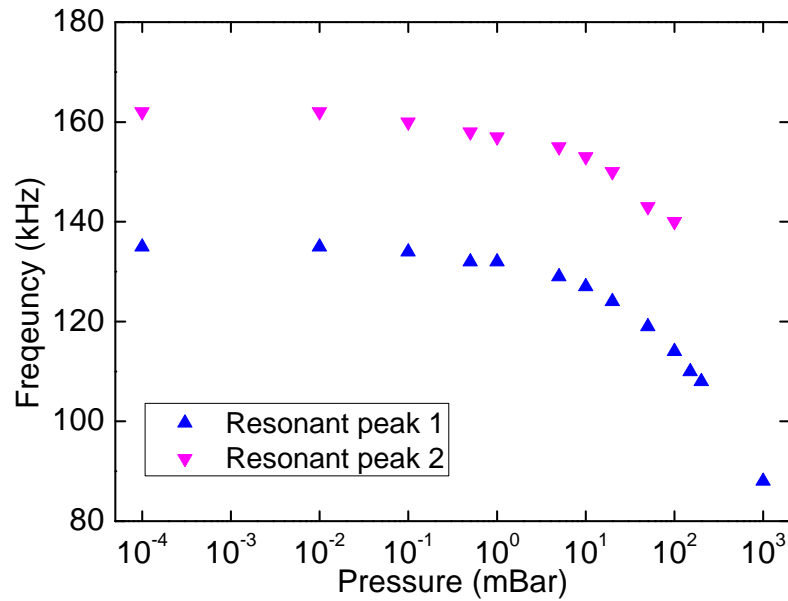


Fig. 6.20 Resonant frequency of the fundamental resonant mode of the beam-shape graphene diaphragm as a function of the air pressure.

## 6.6 Summary

In this chapter, a graphene diaphragm based micro-mechanical resonator is

constructed on a ferrule top by using a PMMA-assisted transferring process. The micro-mechanical resonator is optically excited and interrogated by using an all-fiber system without the bulky desktop for the optical alignment. The performance of the resonators has been theoretically and experimentally investigated in terms of the resonant frequency and the quality factor. A relative resonant frequency shift of ~35 % for the resonator with a beam-shape graphene diaphragm from the vacuum to atmosphere has been demonstrated. This value is about 30 times larger than that of conventional cantilever based resonators. Since the resonant frequency shift of the sensor is induced by the pressure dependent damping effect, the sensor needs no sealed cavity and is inherently immune to mechanical creep during the up and down cycles of the pressure. The easy and compact all-fiber actuation and interrogation scheme makes the ferrule top graphene resonator an attractive sensor for pressure measurement. The strong interaction of the graphene film with the outer environment might also make the resonator a promising candidate for sensitive mass, force and gas concentration detection.

## References for Chapter 6

- [1] G. Stemme, "Resonant silicon sensors," *J. Micromech. Microeng.* 1, 113-125 (1991).
- [2] D. Uttamchandani, K. E. B. Thornton, J. Nixon, and B. Culshaw, "Optically excited resonant diaphragm pressure sensor," *Electron. Lett.* 23, 152-153 (1987).
- [3] K. E. B. Thornton, D. Uttamchandani, and B. Culshaw, "A Sensitive Optically-Excited Resonator Pressure Sensor," *Sensors Actuators A.* 24, 15-19 (1990).
- [4] M. Cocuzza, I. Ferrante, A. Ricci, E. Giuri, L. Scaltrito, D. Bich, A. Merialdo, P. Schina, and R. Correale, "Silicon laterally resonant microcantilevers for absolute pressure measurement with integrated actuation and readout," *J. Vac. Sci. Technol. B.* 26, 541-550 (2008).
- [5] F. R. Blom, S. Bouwstra, M. Elwenspoek, and J. H. J. Fluitman, "Dependence of the Quality Factor of Micromachined Silicon Beam Resonators on Pressure and Geometry," *J. Vac. Sci. Technol. B.* 10, 19-26 (1992).

- [6] J. S. Bunch, A. M. van der Zande, S. S. Verbridge, I. W. Frank, D. M. Tanenbaum, J. M. Parpia, H. G. Craighead, and P. L. McEuen, "Electromechanical resonators from graphene sheets," *Science* 315, 490-493 (2007).
- [7] R. A. Barton, J. Parpia, and H. G. Craighead, "Fabrication and performance of graphene nanoelectromechanical systems," *J. Vac. Sci. Technol. B.* 29, 050801 (2011).
- [8] J. W. Suk, A. Kitt, C. W. Magnuson, Y. Hao, S. Ahmed, J. An, A. K. Swan, B. B. Goldberg, and R. S. Ruoff, "Transfer of CVD-grown monolayer graphene onto arbitrary substrates," *ACS Nano* 5, 6916-6924 (2011).
- [9] A. M. van der Zande, R. A. Barton, J. S. Alden, C. S. Ruiz-Vargas, W. S. Whitney, P. H. Q. Pham, J. Park, J. M. Parpia, H. G. Craighead, and P. L. McEuen, "Large-Scale Arrays of Single-Layer Graphene Resonators," *Nano Lett.* 10, 4869-4873 (2010).
- [10] R. A. Barton, B. Ilic, A. M. van der Zande, W. S. Whitney, P. L. McEuen, J. M. Parpia, and H. G. Craighead, "High, Size-Dependent Quality Factor in an Array of Graphene Mechanical Resonators," *Nano Lett.* 11, 1232-1236 (2011).
- [11] C. F. Beards, *Structural vibration: analysis and damping*, Arnold, Halsted Press (1996).
- [12] R. M. G. JR, "Resonant frequency characterization of a novel MEMS based membrane engine," MSc Thesis, Washington State University, 2004.
- [13] S. Inaba, K. Akaishi, T. Mori, and K. Hane, "Analysis of the Resonance Characteristics of a Cantilever Vibrated Photothermally in a Liquid," *J. Appl. Phys.* 73, 2654-2658 (1993).
- [14] S. Inaba and K. Hane, "Photothermal Vibration for a Membrane in Water," *J. Appl. Phys.* 71, 3631-3632 (1992).
- [15] J. W. Weaver, S. P. Timoshenko, D. H. Young, *Vibration Problems in Engineering*, 5th Edition, Wolfenden Press, 2007.
- [16] W. H. Waugh, B. J. Gallacher, and J. S. Burdess, "A high-sensitivity resonant sensor realized through the exploitation of nonlinear dynamic behaviour," *Meas. Sci. Technol.* 22, 105202 (2011).
- [17] W. H. Waugh, "A high-sensitivity resonant sensor realised through the exploitation of nonlinear dynamic behaviour," PhD Thesis, Newcastle University, 2010.
- [18] S. Kaneko, T. Nakamura, F. Inada, M. Kato, *Flow-induced vibrations*, Elsevier, 2008.
- [19] R. D. Blevins, *Flow-induced vibration*, 2nd edition, Van Nostrand Rheinhold, 1990.
- [20] R. D. Blevins, "Formulas for natural frequency and mode shape," Krieger Publishing Company, 1979.
- [21] K. Kokubun, M. Hirata, M. Ono, H. Murakami, and Y. Toda, "Frequency-Dependence of a Quartz Oscillator on Gas-Pressure," *J. Vac. Sci. Technol. A.* 3, 2184-2187 (1985).
- [22] K. L. Aubin, *Radio Frequency Nano/microelectromechanical Resonators: Thermal and Nonlinear Dynamics Studies*, Cornell University, 2005.
- [23] A. A. Balandin, S. Ghosh, W. Bao, I. Calizo, D. Teweldebrhan, F. Miao, and C.

- N. Lau, "Superior thermal conductivity of single-layer graphene," *Nano Lett.* 8, 902-907 (2008).
- [24] E. Pop, V. Varshney, and A. K. Roy, "Thermal properties of graphene: Fundamentals and applications," *MRS Bull.* 37, 1273 (2012).
- [25] S. S. Gupta and R. C. Batra, "Elastic properties and frequencies of free vibrations of single-layer graphene sheets," *J. Comput. and Theor. Nanosci.* 7, 2151-2164 (2010).
- [26] R. R. Nair, P. Blake, A. N. Grigorenko, K. S. Novoselov, T. J. Booth, T. Stauber, N. M. R. Peres, and A. K. Geim, "Fine structure constant defines visual transparency of graphene," *Science* 320, 1308 (2008).
- [27] C. Lee, X. Wei, J. W. Kysar, and J. Hone, "Measurement of the elastic properties and intrinsic strength of monolayer graphene," *Science* 321, 385-388 (2008).
- [28] M. Olfatnia, Z. Shen, J. M. Miao, L. S. Ong, T. Xu, and M. Ebrahimi, "Medium damping influences on the resonant frequency and quality factor of piezoelectric circular microdiaphragm sensors," *J. Micromech. Microeng.* 21, 045002 (2011).
- [29] Y. Kozlovsky, "Vibration of plates in contact with viscous fluid: Extension of Lamb's model," *J. Sound Vib.* 326, 332-339 (2009).
- [30] K. Hane, T. Iwatuki, S. Inaba, and S. Okuma, "Frequency shift on a micromachined resonator excited photothermally in vacuum," *Rev. Sci. Instrum.* 63, 3781 (1992).
- [31] S. Inaba and K. Hane, "Resonance Frequency-Shifts of a Photothermal Vibration in Vacuum," *J. Vac. Sci. Technol. A.* 9, 2138-2139 (1991).
- [32] D. Yoon, Y.-W. Son, and H. Cheong, "Negative Thermal Expansion Coefficient of Graphene Measured by Raman Spectroscopy," *Nano Lett.* 11, 3227-3231 (2011).
- [33] D. Garcia-Sanchez, A. M. van der Zande, A. San Paulo, B. Lassagne, P. L. McEuen, and A. Bachtold, "Imaging mechanical vibrations in suspended graphene sheets," *Nano Lett.* 8, 1399-1403 (2008).
- [34] Y. Xu, J.-T. Lin, B. W. Alphenaar, and R. S. Keynton, "Viscous damping of microresonators for gas composition analysis," *Appl. Phys. Lett.* 88, 143513 (2006).

# Chapter 7

## Conclusion and future work

### 7.1 Conclusion

In this thesis, several miniature fiber-tip pressure/acoustic sensors have been demonstrated to possess advantages in terms of simple fabrication process, miniature structure size and higher sensitivity compared to conventional FOPSs.

Firstly, an all-silica micro-cavity at the SMF tip has been developed by using a simple and low-cost fabrication process, which requires only a fusion splicer. Micro-cavities with different cavity length and silica wall thickness have been fabricated by controlling the fusion time and current. The pressure sensitivity is theoretically and experimentally investigated and is inversely proportional to the silica wall thickness of the micro-cavity. With a pressure-assisted capillary tapering process, the silica wall thickness of the micro-cavity has been successfully reduced from several tens of micrometers down to a few micrometers. For a micro-cavity with a silica wall thickness of 2.2  $\mu\text{m}$ , a linear pressure response (adjusted R-Square larger than 0.99995) and a sensitivity of  $\sim 315$  pm/MPa over a pressure range from 0 to 40 MPa have been demonstrated. The micro-cavities also exhibit a low temperature sensitivity of  $\sim 1.55$  pm/ $^{\circ}\text{C}$  and high temperature stability for temperature up to 600  $^{\circ}\text{C}$ . The major advantages for the micro-cavity are: 1) a simple fabrication process which involves no multiple steps, e.g., cleaving, polishing, chemical etching and bonding as needed for the conventional diaphragm based FPIs; 2) a linear pressure response and a low temperature cross-sensitivity; 3) a high mechanic strength and good temperature stability since the micro-cavity is directly melt into the SMF end and the whole

structure is all-fused-silica without multiple parts with different thermal expansion coefficients.

Secondly, the pressure sensitivity of the diaphragm based FPI have been significantly increased by employing the graphene as the diaphragm. The ultra-small thickness and high mechanical strength of the graphene make itself a promising candidate as the diaphragm for highly sensitive pressure/acoustic detection. A few-layer graphene film (thickness of  $\sim 1$  nm) produced by the chemical vapor deposition has been successfully transferred to a SMF fiber tip to build pressure sensors. The sensor with an air-cavity diameter of only  $\sim 25$   $\mu\text{m}$  demonstrates a pressure sensitivity of  $\sim 39.2$  nm/kPa which corresponds to a pressure resolution of about 4 Pa. To further improve the pressure sensitivity, a 100 nm thick multi-layer graphene with a larger diameter of  $\sim 125$   $\mu\text{m}$  has been transferred onto a zirconia ferrule top to build a highly-sensitive acoustic pressure sensor. By using a linear phase demodulation technique, the ferrule-top FPI with the multi-layer graphene demonstrates a high acoustic pressure sensitivity of up to 1100 nm/kPa, which is the highest value reported to date according to our knowledge, for the diaphragm based FPIs with similar diaphragm sizes. The sensor exhibits a flat frequency response from 0.2 to 22 kHz and a noise equivalent acoustic signal level of  $\sim 60$   $\mu\text{Pa}/\text{Hz}^{1/2}$  at a frequency of 10 kHz.

Finally, the graphene based micro-mechanical resonators have been demonstrated. The resonating performance of the resonators has been theoretically and experimentally investigated. The fundamental resonant frequency and Q value for the circular graphene membranes vary respectively from 170-500 kHz and 58~250 in the vacuum. For pressure measurements, a beam-shape graphene resonator exhibits a relative resonant frequency shift of  $\sim 35$  % from the vacuum to atmosphere, which is about 30 times larger than that of conventional cantilevers. This large frequency shift agrees with the theoretical prediction that the resonant frequency is mainly influenced

by the pressure-dependent reaction force between the air and the vibrating graphene resonator. The major advantages for this micro-resonator for pressure sensing are : 1) a higher pressure sensitivity: the ultra-small thickness and mass of the graphene film makes itself couple strongly with the outer environment; 2) a easy experiment setup and compact structure: the ferrule-top configuration make the resonator integrated easily with the optical fiber, and thus the micro-resonator can be excited and interrogated optically by just one piece of optical fiber, which avoids the bulky desktop for the optical alignment; 3) an inherent immunity to the mechanical fatigue during the up and down cycles of the pressure: the sensor utilizes the resonant frequency shift induced by the pressure dependent damping, which requires no pressure difference between the two sides of the diaphragm.

## **7.2 Future work**

We have fabricated several novel diaphragm based FPIs for pressure/acoustic measurement with advantages in terms of simple fabrication process, miniature structure size and higher sensitivity. Several suggestions for future investigation are given as follows:

1) The pressure sensitivity of the micro-cavity can be further increased by reducing the thickness of the silica wall of the cavity. This can be implemented by using a more stable electric arc discharge for the tapering and melting process. Another method which takes advantage of the ultra-smooth surface of the micro-cavity is chemical etching. Since the micro-cavity is formed by direct melting without undergoing a polishing process, the silica wall thickness might be reduced to submicrometer without the local over-etching problem for the silica diaphragm in conventional fabrication processes.

2) The fabrication (mainly graphene transfer) repeatability for the fiber-tip or

ferrule-top pressure/acoustic pressure sensor can be improved by the use of alternative transfer methods, e.g., the PMMA-assisted transfer process, to avoid the easy damage of the graphene diaphragm caused by the surface tension of the water. The pre-stress in the graphene diaphragm, induced by different transfer methods will be investigated since the pre-stress in the graphene diaphragm plays an important role in the determination of the pressure sensitivity of the sensor. For the acoustic sensor based on the multi-layer graphene, total sealing of the cavity will enable the sensor to carry out highly-sensitive measurement of the low-frequency or static pressures.

3) The quality factor for the graphene based micro-mechanical resonator can be improved by engineering the pre-stress in the graphene. This may be completed by transferring the graphene on a thermally shrinkable substrate and then applying a tensile strain to the graphene by annealing the substrate. The effect of the pre-stress on the resonant frequency and quality factor of the graphene will be studied in detail. Possible applications of the resonator for ultra-sensitive mass, force and gas composition detection will also be investigated.